Spring 1-1-2020

Design And Development of A Powered Pediatric Lower-limb Orthosis

Curt A. Laubscher
Cleveland State University

DESIGN AND DEVELOPMENT OF A POWERED PEDIATRIC LOWER-LIMB ORTHOSIS

CURT A. LAUBSCHER

Bachelor of Mechanical Engineering

Cleveland State University

May 2014

Submitted in partial fulfillment of the requirements for the degree

DOCTOR OF PHILOSOPHY IN ENGINEERING

at the

CLEVELAND STATE UNIVERSITY

MAY 2020

We hereby approve this dissertation for

CURT A. LAUBSCHER

Candidate for the Doctor of Philosophy in Engineering degree

for the Department of Mechanical Engineering and

CLEVELAND STATE UNIVERSITY'S

College of Graduate Studies by

Jerzy T. Sawicki, Ph.D., Committee Chair
Department of Mechanical Engineering

Ryan J. Farris, Ph.D.
Department of Mechanical Engineering

Dan Simon, Ph.D.
Department of Electrical Engineering and Computer Science

Antonie J. van den Bogert, Ph.D.
Department of Mechanical Engineering

Ulrich Zurcher, Ph.D.
Department of Physics

Date of Defense: April 29, 2020

This student has fulfilled all requirements for the

Doctor of Philosophy in Engineering degree

Chandra Kothapalli, Ph.D.
Doctoral Program Director

ACKNOWLEDGEMENTS

The work of this dissertation would not have been possible as presented without the contribution of many individuals, which I am very grateful for. First, I would like to thank my advisor, Professor Jerzy T. Sawicki, for the opportunity and generously providing his valuable time. Without his guidance throughout the years, I would not be where I am today. I would also like to thank my dissertation committee members for their feedback and comments on my work.

In addition, I thank my colleague Alican Sahinkaya for the numerous technical discussions and critical feedback on various aspects of the project. I am also greatly appreciative for the considerable amount of time devoted by Anthony Goo and Huawei Wang in helping conduct the assistive control experiments in this dissertation. Next, I would like to thank the participating subject in the assistive control experiments for volunteering numerous hours and providing valuable feedback on the orthosis design.

Lastly, I would like to specially thank Dr. Ryan J. Farris who has been instrumental throughout the work of this dissertation. His technical expertise has been invaluable, by providing insightful comments for design suggestions, helping navigate the space of possible research directions, and providing extensive feedback on manuscripts. Without his help, this dissertation would not have become what it is.

DESIGN AND DEVELOPMENT OF A POWERED PEDIATRIC

LOWER-LIMB ORTHOSIS

CURT A. LAUBSCHER

ABSTRACT

Gait impairments from disorders such as cerebral palsy are important to address early in life. A powered lower-limb orthosis can offer therapists a rehabilitation option using robot-assisted gait training. Although there are many devices already available for the adult population, there are few powered orthoses for the pediatric population. The aim of this dissertation is to embark on the first stages of development of a powered lower-limb orthosis for gait rehabilitation and assistance of children ages 6 to 11 years with walking impairments from cerebral palsy.

This dissertation presents the design requirements of the orthosis, the design and fabrication of the joint actuators, and the design and manufacturing of a provisional version of the pediatric orthosis. Preliminary results demonstrate the capabilities of the joint actuators, confirm gait tracking capabilities of the actuators in the provisional orthosis, and evaluate a standing balance control strategy on the under-actuated provisional orthosis in simulation and experiment. In addition, this dissertation presents the design methodology for an anthropometrically parametrized orthosis, the fabrication of the prototype powered orthosis using this design methodology, and experimental application of orthosis hardware in providing walking assistance with a healthy adult. The presented results suggest the developed orthosis hardware is satisfactorily capable of operation and functional with a human subject. The first stages of development in this dissertation show encouraging results and will act as a foundation for further

development of the device for rehabilitation and assistance of children with walking impairments.

TABLE OF CONTENTS

NOMENCLATURE

$\boldsymbol{A}'$	State matrix of the linearization of the system $\boldsymbol{G}'$ about the equilibrium point $\boldsymbol{x}^{\mathrm{d}}$
$\boldsymbol{A}''$	State matrix of the linearization of the system $\boldsymbol{G}''$ about the equilibrium point $\boldsymbol{x}^{\mathrm{d}}$
b_{h}	Hip bias torque [N·m]
b_{k}	Knee bias torque [N·m]
$\boldsymbol{B}'$	Input matrix of the linearization of the system $\boldsymbol{G}'$ about the equilibrium point $\boldsymbol{x}^{\mathrm{d}}$
c_j	Shorthand for the cosine function $c_j = \cos(q_j)$
c_{jk}	Shorthand for the cosine function $c_{jk} = \cos(q_j + q_k)$
c_{123}	Shorthand for the cosine function $c_{123} = \cos(q_1 + q_2 + q_3)$
$\boldsymbol{C}_k$	Center of mass position vector of link k represented in the base frame [m]
$\dot{\boldsymbol{C}}_k$	Center of mass velocity vector of link k represented in the base frame [m/s]
d_{ad}	Ankle dorsiflexion damping coefficient [N·m·s/rad]
d_{ap}	Ankle plantarflexion damping coefficient [N·m·s/rad]
d_{h}	Hip damping coefficient [N·m·s/rad]
d_{k}	Knee damping coefficient [N·m·s/rad]
$\boldsymbol{D}$	Controller derivative term [N·m·s/rad]
$\boldsymbol{f}(\boldsymbol{x})$	State function term in the nonlinear state-space system $\boldsymbol{G}$
$\boldsymbol{f}'(\boldsymbol{x})$	State function term in the nonlinear state-space system $\boldsymbol{G}'$

$\boldsymbol{f}''(\boldsymbol{x})$ State function term in the nonlinear state-space system $\boldsymbol{G}''$

g Acceleration due to gravity, 9.81 [m/s^2]

$\boldsymbol{g}(\boldsymbol{x})$ Input coefficient function in the state-space system $\boldsymbol{G}$

$\boldsymbol{g}'(\boldsymbol{x})$ Input coefficient function in the state-space system $\boldsymbol{G}'$

$\boldsymbol{G}$ Triple pendulum system

$\boldsymbol{G}'$ Triple pendulum system with the ankle-model feedback-loop closed

$\boldsymbol{G}''$ Triple pendulum system with the ankle-model and controller feedback-loops closed

$\boldsymbol{G}(\boldsymbol{q})$ Gravity torque vector [N·m]

$G_k(\boldsymbol{q})$ Element k of the gravity torque vector $\boldsymbol{G}(\boldsymbol{q})$ [N·m]

$\boldsymbol{H}(\boldsymbol{q},\dot{\boldsymbol{q}})$ Torque vector of centrifugal, Coriolis, and non-nominal robot model terms in the triple pendulum model [N·m]

i Unit imaginary number

i_k Imaginary component of eigenvalue k of the linearized closed-loop system

I_k Moment of inertia of link k at the center of mass of the link in the triple pendulum [kg·m^2]

$\boldsymbol{I}_k$ The $k \times k$ identity matrix

J Cost function used in numerical optimization in the creation of a momentum-based controller and a linear-quadratic regulator

J_{LQR} Cost function used in the creation of a linear-quadratic regulator

k_{d} Ankle dorsiflexion stiffness used in the ankle stiffness model [N·m/rad]

k_{p}	Ankle plantarflexion stiffness used in the ankle stiffness model [N·m/rad]
K	Number of measurements
$\boldsymbol{K}(\boldsymbol{q},\dot{\boldsymbol{q}})$	Control law [N·m]
$\boldsymbol{K}_{\mathrm{MBC}}$	Momentum-based controller gain matrix associated with the angular momentum
k_{h}	Momentum-based controller hip proportional gain [N·m/rad]
k_{k}	Momentum-based controller knee proportional gain [N·m/rad]
L	Total angular momentum of the nominal triple pendulum system [N·m·s]
$\dot{L}$	Time derivative of the total angular momentum of the nominal triple pendulum system [N·m]
$\ddot{L}$	Second time-derivative of the total angular momentum of the nominal triple pendulum system [N·m/s]
L_k	Length of link k in the triple pendulum [m]
m_k	Mass of link k in the triple pendulum [kg]
$\boldsymbol{M}(\boldsymbol{q})$	Inertia matrix
$M_{\mathrm{a}}(\theta)$	Ankle stiffness model [N·m]
p	The p-value from statistical analyses
P	Penalty term used in numerical optimization of standing balance controllers
$\boldsymbol{P}$	Controller proportional term [N·m/rad]
$\boldsymbol{q}$	Joint angular position vector [rad]
$\dot{\boldsymbol{q}}$	Joint angular velocity vector [rad/s]

$\ddot{\boldsymbol{q}}$ Joint angular acceleration vector [rad/s^2]

q_k Angle of joint k [rad]

q_r Neutral position of the ankle [rad]

$\boldsymbol{q}^d$ Desired joint position vector [rad]

$\tilde{\boldsymbol{q}}$ Joint angular position error vector [rad]

$\dot{\tilde{\boldsymbol{q}}}$ Joint angular velocity error vector [rad/s]

N Number of degrees of freedom in a robotic system

$\boldsymbol{Q}$ The positive-definite state weight matrix used in the creation of a linear-quadratic regulator

$\boldsymbol{R}$ The positive semi-definite input weight matrix used in the creation of a linear-quadratic regulator

r_k Real component of eigenvalue k in the linearized closed-loop system

s_j Shorthand for the sine function $s_j = \sin(q_j)$

s_{jk} Shorthand for the sine function $s_{jk} = \sin(q_j + q_k)$

s_{123} Shorthand for the sine function $s_{123} = \sin(q_1 + q_2 + q_3)$

$S(x)$ Sigmoid function $S(x) = 1/(1 + e^{-x})$

t Time [s]

t^* Statistical significance test statistic threshold in SPM paired t-test

t_k Measured time instant [s]

$\boldsymbol{u}$ Control input signal [N·m]

u_k Control input k [N·m]

$u_{\max}$	Maximum control input at hip or knee joints [N·m]
$\bar{\boldsymbol{u}}$	Concatenated measured control input signal [N·m]
w_{I}	Weight associated with the imaginary component of the eigenvalues used in the creation of a linear-quadratic regulator and momentum-based controller
w_{R}	Weight associated with the real component of the eigenvalues used in the creation of the linear-quadratic regulator and momentum-based controller
x_k	Center of mass of link k from joint k in the triple pendulum [m]
$\hat{\boldsymbol{x}}$	Unit vector in the positive x direction
$\boldsymbol{y}$	Output vector in the systems $\boldsymbol{G}$, $\boldsymbol{G}'$, and $\boldsymbol{G}''$
$\boldsymbol{Y}(\boldsymbol{q},\dot{\boldsymbol{q}},\ddot{\boldsymbol{q}})$	Coefficient matrix-valued function in the model of a robotic system
$\bar{\boldsymbol{Y}}$	Regressor matrix
$\bar{\boldsymbol{Y}}^{+}$	Moore-Penrose left pseudo-inverse of the regressor matrix $(\bar{\boldsymbol{Y}}^{\mathrm{T}}\bar{\boldsymbol{Y}})^{-1}\bar{\boldsymbol{Y}}^{\mathrm{T}}$
$\boldsymbol{Y}_{\mathrm{a}}(\boldsymbol{q},\dot{\boldsymbol{q}},\ddot{\boldsymbol{q}})$	Augmented part of the coefficient matrix-valued function in the triple pendulum model
$\boldsymbol{Y}_{\mathrm{n}}(\boldsymbol{q},\dot{\boldsymbol{q}},\ddot{\boldsymbol{q}})$	Nominal part of the coefficient matrix-valued function in the triple pendulum model
$\boldsymbol{Y}_{\mathrm{s}}(\boldsymbol{q},\dot{\boldsymbol{q}},\ddot{\boldsymbol{q}})$	Coefficient matrix-valued function in the shank model
$\boldsymbol{Y}_{\mathrm{sa}}$	Augmented part of the coefficient matrix-valued function in the shank model
$\boldsymbol{Y}_{\mathrm{sn}}$	Nominal part of the coefficient matrix-valued function in the shank model
$\boldsymbol{Y}_{\mathrm{tt}}(\boldsymbol{q},\dot{\boldsymbol{q}},\ddot{\boldsymbol{q}})$	Coefficient matrix-valued function in the thigh and torso model

$\boldsymbol{Y}_{\mathrm{tta}}$ Augmented part of the coefficient matrix-valued function in the thigh and torso model

$\boldsymbol{Y}_{\mathrm{ttn}}$ Nominal part of the coefficient matrix-valued function in the thigh and torso model

$\boldsymbol{z}$ State vector

$\hat{\boldsymbol{z}}$ Unit vector in the positive z direction

z_k State k

$\boldsymbol{z}^{\mathrm{d}}$ Desired equilibrium state

α Significance level used in statistical analyses

β Ankle angle normalization constant used in the weights in the ankle stiffness model [rad]

$\kappa\left(\bar{\boldsymbol{Y}}\right)$ Condition number of the regressor matrix

λ_k Eigenvalue k of the state matrix $\boldsymbol{A}''$ [rad/s]

$\boldsymbol{\Phi}$ Parameters in the triple pendulum model

Φ_k Parameter k in a robotic system

$\boldsymbol{\Phi}_{\mathrm{a}}$ Augmented parameters in the triple pendulum system

$\boldsymbol{\Phi}_{\mathrm{n}}$ Nominal (inertial) parameters in the triple pendulum system

$\boldsymbol{\Phi}_{\mathrm{s}}$ Parameters in the shank model

$\boldsymbol{\Phi}_{\mathrm{sa}}$ Augmented parameters in the shank model

$\boldsymbol{\Phi}_{\mathrm{sn}}$ Nominal (inertial) parameters in the shank model

$\boldsymbol{\Phi}_{\mathrm{tt}}$ Parameters in the thigh and torso model

Φ_{tta} Augmented parameters in the thigh and torso model

Φ_{ttn} Nominal (inertial) parameters in the thigh and torso model

θ Orientation of the shank relative to the vertical [rad]

θ_0 Ankle angle offset used in the weights in the ankle stiffness model [rad]

θ_{d} Ankle dorsiflexion offset used in the ankle stiffness model [rad]

θ_{p} Ankle plantarflexion offset used in the ankle stiffness model [rad]

ω_k Angular velocity of link k [rad/s]

$\dot{\omega}_k$ Angular acceleration of link k [rad/s^2]

$\langle \cdot \rangle$ Iverson bracket function, 1 when the given condition is true and 0 otherwise

$\| \cdot \|$ Induced matrix 2-norm

LIST OF TABLES

LIST OF FIGURES

CHAPTER I

INTRODUCTION

1.1 Background Information

There are a number of developmental, neurological, and neuromuscular disorders in children that can result in varying levels of gait impairment, such as cerebral palsy, spina bifida, and muscular dystrophy. Cerebral palsy (CP) is a non-progressive developmental brain lesion disorder resulting in a deficit in neuromotor control, and is often accompanied by a progressive musculoskeletal impairment [1], [2]. Children with CP often have limited muscle strength, are incapable of producing normal muscle forces or joint torques, have limited range of motion [1], [3], [4], and display abnormal gait such as crouch gait, scissor walking, Trendelenburg gait, or stiff knee in swing [1], [5]. As the most common childhood motor disability, CP accounts for 8,000 new cases every year in the United States, with about 36 children with CP for every 10,000 school-aged children [2]. Another example of a disorder resulting in gait impairment is spina bifida (SB), also referred to as myelodysplasia, a progressive developmental malformation of the spinal cord due to neural tubes failing to properly close in the congenital stage of child development [1], [2]. Functional ability of children with SB can vary considerably, though they can show impaired posture and stability, decreased muscle strength, and muscle imbalance [1]. Approximately 3 for every 10,000 children aged 8 to 11 years in the United States have SB [6]. A third example of a disorder resulting in gait impairment is muscular dystrophy (MD), a genetic disorder of progressive loss of muscle fibers resulting in muscle atrophy and weakness which can be accompanied by musculoskeletal disease [1], [2]. Prevalence estimates put at least 1 in 10,000 individuals worldwide living with MD [7].

It is important to address poor ambulation in children with CP early in their development since secondary impairment may arise as the child grows, such as skeletal malalignment and contractures due to limited physical activity and participation [1]. This is particularly true for the about 34% of children with CP that are wheelchair-bound or require the use a mobility device [1]. Traditionally, rehabilitation of individuals with gait impairment is accomplished using overground gait training, usually with the aid of parallel bars, canes, walkers, or crutches [2], [8]. Alternatively, treadmill-based gait training can be used for gait rehabilitation. This form of therapy allows for more task-specific training and more steps for each training session [9] as compared to overground gait training. Although evidence is somewhat limited, there are reports that treadmill-based gait training can improve gross motor function, walking performance, and gait parameters such as step length [8], [10]. In both overground and treadmill-based gait training, overhead harness systems are sometimes used, providing partial bodyweight support to the patient [2], [8], [9], [11]; the amount of support can be gradually decreased in order to increase patient strength [8]. However, these treatments are limited in a number of ways. First, they usually involve one or two therapists or clinicians providing manual guidance to the patient's legs, which can be physically demanding to the therapists and is often a limiting factor in the duration of the training sessions [12]. Second, it can also be difficult for therapists to achieve symmetrical gait between the patient's legs throughout the training session [13]. Third, these gait training methods pose some noteworthy risks for injury to the therapists during training [13]. Fourth, sessions may not be intense enough for the patients with neuromotor dysfunction such as CP and therefore may be inadequate for rehabilitation [14]. Fifth, the restriction to straight-line walking on a treadmill and the bodyweight support harness makes balance training allowed by overground gait training difficult or not possible. Lastly, these therapies lack an objective, quantitative performance measure necessary to evaluate gait improvements [2], [11].

A lower-limb exoskeleton is a powered orthosis designed to provide torque to the hips, knees, and/or ankles, and can augment, assist, or rehabilitate a subject in performing some task such as walking. Such a device can be designed for robot-assisted gait training, offering a better option for therapists that would mitigate some of the aforementioned shortcomings of traditional overground and treadmill-based gait training. It removes the need for a therapist to manually move the legs of the patient, therefore permitting an increase in session duration and intensity, removing the risk for therapist injury, and increasing symmetry of assistance. In addition, the device would include a multitude of sensors, providing therapists with data recorded during gait training sessions which can be useful for quantitative evaluation and comparison of gait performance. Also, a mobile powered lower-limb orthosis can be used outside the context of a gait rehabilitation, providing the user with assistance when needed and potentially improving mobility when used in a community setting.

1.2 State-of-the-Art of Powered Pediatric Lower-Limb Orthoses

There are many powered adult lower-limb orthoses that are either currently commercially available or under development. These devices have been thoroughly reviewed in the literature, such as in [12], [15], [16]. This is in contrast with devices for the pediatric population, of which there are only a small number. Lokomat [17], [18] is a commercially available platform developed by Hocoma consisting of an exoskeleton integrated into a treadmill with overhead bodyweight support system. Although primarily used in adult gait rehabilitation, Locomat has been recently adapted to allow gait therapy with children and has been clinically tested with children with CP around 10 years of age. The device is adaptable to the size of the child and can supply torque to the hip and knee joints using electric drives.

Marsi Bionics developed the ATLAS 2020 [19]–[21], a 10 degree-of-freedom (DOF) exoskeleton for children ages 3 to 12 years with spinal muscular atrophy and similar pathologies. The dimensions of the device can be adjusted to fit the growing child. They use a variable-stiffness series-elastic actuator driven by an electric motor through a harmonic drive system to actuate the flexion-extension DOF at the hip, knee, and ankle. The device also uses linear drives powered by brushless DC motors to actuate the adduction-abduction DOF at the hip and the eversion-inversion DOF at the ankle. Clinical trials are underway with their current prototype, the ATLAS 2030 [22], a similar exoskeleton weighing only 14 kg and designed for children ages 3 to 14 years.

Patané et al. [23] published an article on their WAKE-Up exoskeleton, a modular 2.5 kg device designed for children ages 5 to 13 years of age that have neurological disorders such as CP. It is adjustable to accommodate different thigh and shank body segment lengths. The device uses identical compliant actuators to drive the knees and ankles using servomotors and is capable of providing up to 5.6 N·m of torque within the sagittal plane.

Researchers from NIH [24], [25] created a knee-ankle-foot-orthosis (KAFO)-based device for children with CP which can provide up to 16.1 N·m of knee flexion-extension torque using a 90 W brushless DC motor through a planetary gear and chain drive system. The ankle can be configured to be either passive or locked in position. The overall device weight ranged from 2.6 to 4.5 kg, depending on the particular KAFO that was used, and excludes the weight of the 2.0 kg control box.

Copilusi et al. [26], [27] developed a modular knee orthosis with multiple rotation axes designed for children ages 4 to 7 years. The device is driven by a single servomotor which drives two flexible steel cables fed through a pulley system, allowing for flexion or extension torque at the knee. Copilusi et al. [28] also recently developed a device designed for children around 7 years of age which can actuate the hips, knees, and ankles using servomotors operating behind a chain transmission.

Giergiel et al. [29] created a stationary rehabilitation robot for children around 7 to 9 years of age who weigh 25 kg and can supply torque to the hips, knees, and ankles using servomotors. Canela et al. [30] published a description of an exoskeleton for children ages 7 to 17 years who have CP. The lengths of the device links are adjustable using telescopic bars and the hips, knees, and ankles are driven by brushless DC motors.

Androwis et al. [31] modified a passive hip-knee-ankle orthosis for children with CP with the addition of servomotors plus gear transmission capable of providing 35 N·m of torque at the hip, knee, and ankle joints.

There are a couple noteworthy robotic devices for the pediatric population that are not strictly considered powered lower-limb orthoses. Kang et al. [32] demonstrated their tethered pelvis assist device, a cable-driven device that applies a downward force on the subject's pelvis while walking on a treadmill. The authors showed how children ages 9 to 19 years old with crouch gait can increase muscle activation, reduce crouch gait, improve posture, improve step length, increase range of motion, and increase toe clearance from CP training with their set up. The Anklebot [33], [34], developed by researchers at Massachusetts Institute of Technology, is a low friction and backdrivable ankle-training robotic device which was adapted for children ages 6 to 11 years with neurological disorders such as CP. It uses linear actuators driven by DC motors to supply a maximum dorsiflexion-plantarflexion torque of 7.21 N·m and inversion-eversion torque of 4.38 N·m. The internal-external DOF at the ankle is left passive.

For a summary of the aforementioned pediatric robotic devices, see Table I.

Each of the above pediatric devices is limited in at least one aspect. A number of these devices are stationary as they are either integrated with a treadmill system or are intrinsically stationary (i.e., Lokomat [17], [18], Copilusi et al. [28], Giergiel el al. [29], Kang et al. [32], and Anklebot [33], [34]). This limits the use of these device to rehabilitation and cannot be used for assistance within a community setting. Of the remaining mobile devices (i.e., ATLAS [19]–[22], WAKE-Up [23], NIH KAFO [24], [25], Copilusi et al. [26], [27], Canela et al. [30], and Androwis et al. [31]), most have

Table I. Summary of pediatric robotic assistive and rehabilitative devices

Device	Actuated DOF [1]	Target Ages	Weight	Mobility	Sources
Lokomat	H_f, K_f	~10 yr	*N/A* [2]	Stationary	[17], [18]
ATLAS	H_f, H_a, K_f, A_f, A_v	3–12/14 yr	14 kg	Mobile	[19]–[22]
WAKE-Up	K_f, A_f	5–13 yr	2.5 kg	Mobile	[23]
NIH KAFO	K_f	5–19 yr	2.6–4.5 kg	Mobile	[24], [25]
Copilusi et al.	K_f	4–7 yr	- [3]	Mobile	[26], [27]
Copilusi et al.	H_f, K_f, A_f	~7 yr	*N/A*	Stationary	[28]
Giergiel et al.	H_f, K_f, A_f	~7–9 yr	*N/A*	Stationary	[29]
Canela et al.	H_f, K_f, A_f	7–17 yr	-	Mobile	[30]
Androwis et al.	H_f, K_f, A_f	-	-	Mobile	[31]
Kang et al.	None	9–19 yr	*N/A*	Stationary	[32]
Anklebot	A_f, A_v	6–11 yr	*N/A*	Stationary	[33], [34]

[1] A: ankle, K: knee, H: hip
f: flexion-extension or plantarflexion-dorsiflexion DOF
a: adduction-abduction DOF
v: inversion-eversion DOF

[2] Not applicable

[3] Information not reported

few published articles, have undergone little or no clinical work, seem to not be further researched, are not sufficiently powerful, or are heavy or bulky which can make them intimidating or difficult to use by children. Some devices, like the NIH KAFO [24], [25] or Copilusi et al. [26], [27] device, are capable of actuating only a single joint on each leg. An ideal powered lower-limb orthosis for rehabilitation and assistance should have an active or passive joint at each hip, knee and ankle joint.

1.3 Motivation and Objectives for Dissertation Research

There is currently a wealth of literature on the development, control [35], [36], and clinical application of powered lower-limb orthoses for adults with paralysis or gait impairment from e.g. spinal cord injury [37] or stroke [38], [39]. This is in contrast to the relatively few powered lower-limb orthoses available for the pediatric population, despite the importance of early orthotic intervention to avert and mitigate long-term ambulatory issues in children [40]. Few orthoses for children can provide both rehabilitative and assistive capabilities and are adequately small and lightweight. The Marsi Bionics ATLAS orthosis [19]–[22] is a versatile device with these capabilities by being a mobile device which can actively control the hips, knees, and ankle joints in more than just the sagittal plane, but at the cost of being heavy and bulky.

Motivated by these points and inspired by the Indego exoskeleton from Parker Hannifin [41]–[43], there are two aims for this dissertation. The first aim is the design of a small, lightweight, and mobile powered lower-limb orthosis that is parametrized in terms of the anthropometrics of children ages of 6 to 11 years with walking impairments from disorders such as CP. The second aim is the preliminary evaluation of a prototype orthosis by conducting experiments to determine assistive capabilities. The development and evaluation are being carried out in collaboration with the Parker Hannifin Human Motion and Control team. CHAPTER II presents the development of the pediatric orthosis, and includes discussion on the design requirements for the actuators and orthosis, design of the actuators used in the orthosis, and design and fabrication of a prototype version of an anthropometrically parametrized orthosis. CHAPTER III presents the results obtained from preliminary evaluation of the prototype orthosis, and includes bench-top testing of the actuator's capabilities, gait-tracking experiments demonstrating use of the actuators, and a comparison of two standing balance controllers in simulation and experiment. CHAPTER IV presents the experimental evaluation of the anthropometrically parametrized orthosis for its ability to provide assistance to a healthy adult subject. Lastly, CHAPTER V concludes with an overview on the contributions of this dissertation and possible directions of future research.

CHAPTER II

DESIGN OF A POWERED PEDIATRIC LOWER-LIMB ORTHOSIS PROTOTYPE

This chapter presents the design of the powered pediatric lower-limb orthosis. First, the design requirements for the orthosis will be explored, including discussion on target users and healthy gait, and how these impact the design specifications and other requirements. Next, the actuator design is covered based on these design requirements. Finally, an anthropometrically parametrized orthosis design is presented, including a discussion on the necessary user anthropometrics and how those relate to the key orthosis dimensions, which is applied for the fabrication of a prototype adult device.

2.1 Design Requirements and Specifications

The powered orthosis presented in this dissertation is designed for both assistance and rehabilitation of children ages 6 to 11 years with gait impairments. The lower age of 6 years is chosen to ensure children have adequate motor skills, attention span, and communication skills to be able to focus on specific tasks while following a series of commands [44]. This is important for effective use of the powered orthosis for rehabilitation as children around this age have better self-control and are better at listening to and following instructions than their younger counterparts [45]. The upper age of 11 years is chosen because children about this age are nearly tall enough, at around 150 cm [46], to begin considering using one of the many commercially available exoskeletons designed for adults. For reference, the Rex Bionics exoskeleton reportedly accommodates adults with a standing height from 142 to 193 cm [47], Ekso Bionics from 150 to 190 cm [48], and Indego from 155 to 191 cm [49], to name a few commercialized devices for adults.

Many adult exoskeletons have undergone numerous clinical trials. Even devices that only actuate the hip and knee joints within the sagittal plane show some evidence for their ability to assist or rehabilitate individuals with either complete lower-limb paralysis or partial gait impairments. For instance, the ReWalk, Ekso, Indego, and ALEX devices have been used for assisting patients of a spinal cord injury or stroke in various clinical publications and are reviewed in [37]–[39]. The orthosis presented in this dissertation takes a similar approach by having the flexion-extension DOF at the hips and knee joints actuated. The hip adduction-abduction DOF is left free to allow the subject to naturally walk and balance. The ankle will be left passive, using a readily available or patient-brought ankle-foot orthosis (AFO) if necessary, which would be fairly common given about half of individuals with CP already use an AFO [50]. This also circumvents the need for an actuator to power the ankle, which would otherwise make the device heavier with a third actuator located low in the leg and therefore increase the mass and moment of inertia of the shank component of the orthosis, which could be detrimental to performance due to the placement. This increase in lower leg inertia could be partially mitigated by locating the actuator further up in the orthosis such as through the use of a cable-and-pully system, though at the cost of added complexity.

There are a few special requirements and challenges posed in the design of a pediatric orthosis which are not all necessarily addressed in adult orthoses. First, the device must accommodate the large range and changes in weight and height of children as they grow, which is about 3 to 3.5 kg and 6 cm per year [51]. The device can account for this wide range and variation by being easily adjustable in dimensions. Alternatively, the frame of the orthosis can be made particular to the child and periodically re-fitted as the child grows. The latter choice is chosen over the former because it can provide an improved fit to the child by allowing for custom contouring of the interfacing components. In addition, anatomical and physiological abnormalities, like deformed bone structure which may be present in individuals with CP and SB [2], can be considered in the design. The frame of the orthosis would be designed with parametric modeling based on measured anthropometrics of the child and fabricated using additive manufacturing techniques. This design methodology is described in more detail in Section 2.3. Second, the electronics and actuators should be modular to allow for easy insertion into this custom-made frame. The actuator should be designed to not require the frame for operation and is described in Section 2.2. Third, the device must be easy to learn and use by children which, when compared to adults, have shorter attention spans and poorer concentration skills due to how they are still cognitively developing [51]. The modular actuators can be inserted into an orthosis frame described in Section 2.3, nearly completely hidden from view. Fourth, the pediatric device must be lighter and smaller than devices for the adult population. Moreover, the pediatric device should also be quiet, safe, and approachable to children without requiring extensive training. This is to make the device less intimidating, and also to avoid making the device difficult and unnatural to wear and use by children. This is particularly true for children on the younger side of the target population, as gait therapy can start in children with CP or SB as young as 5 years [52]. Ideally, the device should be much lighter than the child, which is around 24 kg on average for children 6 years of age [46]. For reference, the ATLAS 2030 exoskeleton by Marsi Bionics weights 14 kg [22]; the orthosis described in this dissertation should be designed to be comparable to or lighter than this. The actuator in Section 2.2 and orthosis in Section 2.3 were designed to keep weight as small as reasonably possible without compromising basic functionality. Fifth, the actuators should be backdrivable. This permits the user to walk with the device donned but unpowered. This can be accomplished by keeping friction and inertia small and avoiding use of components like worm gears and harmonic gears which may be non-backdrivable; this is considered in the design of the actuator in Section 2.2. Lastly, since the device should be used not only as a rehabilitative device but also as an assistive device, it should be mobile and therefore usable in a community setting. That is, the powered orthosis should not be tethered to external equipment nor restricted to use only on a treadmill in the final design. This is considered in the source of mechanical power for the actuator in Section 2.2.

The anthropometrics and gait characteristic of healthy subjects in the target age range of 6 to 11 years are used to determine the basic design specifications of the actuator and orthosis. The average and standard deviation of weights and heights of children ages 6, 8, and 11 years are shown in Table II [46]. Adults typically have a natural cadence around

Table II. Average and standard deviation of weights and heights of children

Age (years)	6	8	11
Weight, male (kg)	24.3 ± 6.5	31.3 ± 10.2	46.6 ± 16.4
Weight, female (kg)	23.6 ± 6.3	31.9 ± 14.4	47.5 ± 18.9
Height, male (cm)	119.3 ± 6.3	131.6 ± 9.6	149.9 ± 9.0
Height, female (cm)	119.2 ± 6.9	131.3 ± 12.0	150.4 ± 8.0

101 to 120 steps per minute, whereas children usually walk at a faster cadence, at around 144 steps per minutes for children 7 years of age [53]. This suggests that children around the lower age of the target users are expected to have a gait period around 0.8 s and slower for older children. However, in practice, the gait period when using the orthosis is expected to be slower than this, particular for children with more severe gait impairments. For example, those with CP tend to have a reduced walking speed [10]. Typical healthy adult gait is used as a reference, which should adequately represent most healthy children in the target age range because children 7 years old have a gait similar to that of adults [51]. Nominal gait pattern, joint torques, and joint powers for the hip and knee are shown in Figure 2.1, where torque and power are normalized to the subject weight [53]. With a cadence of 110 steps per minute and the expected weights of children in the target population, the expected range of motion, joint velocity, joint torque, and joint power are tabulated in Table III. Sign convention used in this chapter for joint positions, velocities, and torques are positive for flexion and negative for extension. The actuators for the orthosis should be designed such that they can provide at least the full range of motion and velocity, while also able to supply at least comparable torque and power to the hip and knee joints.

A summary of the main design requirements and specifications covered in this section are shown in Table IV.

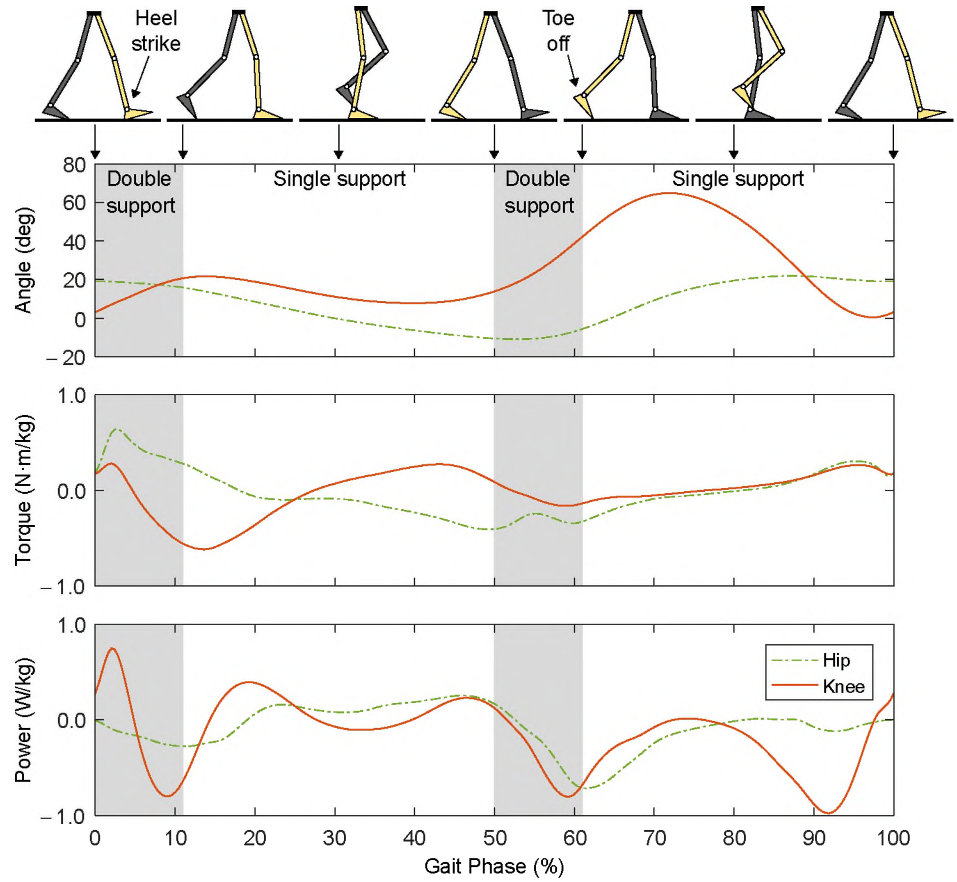

Figure 2.1 Nominal gait pattern, joint torque, and joint power

Table III. Expected range for a number of gait characteristics

	Hip	Knee
Range of motion (deg)	−11 to 22	0 to 65
Velocity (deg/s)	−82 to 159	−369 to 312
Torque for an average 6 year old child (N·m)	−9.9 to 14.8	−15.1 to 6.9
Torque for an average 8 year old child (N·m)	−13.8 to 19.0	−19.4 to 8.9
Torque for an average 11 year old child (N·m)	−19.2 to 28.5	−29.2 to 13.3
Power for an average 11 year old child (W)	−33.9 to 12.1	−46.4 to 35.4

Table IV. Summary of the main design requirements and specifications

Orthosis defined using parametric modeling and compatible with most children ages 6 to 11 years
Modular and backdrivable actuators for the hip and knee joints for flexion and extension
Allows for at least full range of motion from −11 to 22 deg at the hip and 0 to 65 deg at the knee
Capable of providing joint velocities at least 159 deg/s at the hip and 369 deg/s at the knee
At least comparable torque of 28.5 N·m at the hip and 29.2 N·m at the knee
At least comparable power of 33.9 W at the hip and 46.4 W at the knee
Total orthosis weight should be at most 14 kg
Operation should be quiet and not require being tethered

2.2 Design of the Joint Actuator

It was decided to use a single actuator design for both the hips and knees of the orthosis. This allows for simplicity in the design and improves device serviceability as they are interchangeable and components are identical, up to a symmetry difference. The actuator is driven by a brushless DC motor. Electrical power was chosen over hydraulic or pneumatic mode of power transfer to improve ease of implementation, making the device lighter, circumventing risk of fluid leaks and safety issues, and not requiring a tether to noisy external equipment like a compressor and pump. In addition, electric motors are straightforward for implementation, and would only require the addition of a transmission system since smaller motors typically operate at high speeds and low torques.

The Maxon EC 45 flat brushless DC motor [54] is chosen for the electric motor, and is rated to provide 70 W of power nominally. This should be sufficient since, even after transmission losses, this should satisfy the power requirement of 46.4 W at the knee and 33.9 W at the hip from Table III. The motor connects to a transmission system to increase torque and decrease speed at the output of the actuator. A toothed-belt and sprocket system was chosen over gears or chains since a belt system would be lighter, operate quieter, and allow for some compliant behavior when undergoing load, a desirable characteristic in an actuator for powered orthoses for shock absorption and safety [55], [56]. A three-stage transmission system is developed with a speed-reduction ratio of 40.6:1 which incorporates co-axial sprockets that rotate at different speeds to keep the profile of the actuator small. An actuator arm is fastened to the last sprocket of the actuator and is used to interface the actuator with the orthosis. The actuator arm can move from –30 to 110 deg, spanning the necessary range of motion at the hip and knee joints from Table III plus some extra allowance for flexion permitting the user to sit with the device donned. The actuator design includes screw-adjustable mechanisms for tensioning the belts. This allows the motor and a sprocket shaft to move along the actuator, and accordingly affecting compliance, backdrivability, and friction of the device. This can be used to tune the actuator performance when used in the orthosis.

The actuator output has a nominal operating speed of 375 deg/s, continuous operating torque of 5.4 N·m, and a rated stall torque of 35.7 N·m, based on the specifications of the motor and the transmission ratio. Note that this does not account for actuator dynamics and frictional losses; the performance of the actuator in practice will vary from these values according to its efficiency and compliance characteristics. This nominal speed capability should be sufficient to achieve the expected maximum speed of 369 deg/s at the knee and 159 deg/s at the hip. The actuator is small and lightweight, with a thickness of only 46 mm, a width of just 79 mm, and a weight of merely 0.6 kg. The actuator design described here is the second of two revisions; the first revision of the device had a similar transmission ratio of 39.0:1 and could theoretically provide more maximum torque due to the larger width belts used in the design, but had a few design problems. It was large with a thickness of 58 mm and width of 118 mm, and had practical usage problems with the spring-based belt tensioning mechanism. Even so, the rated torques of the second revision of the actuator should be enough to provide some degree of assistance and rehabilitative ability to the user using the orthosis.

The actuator incorporates a magnetic angle sensor (MAS) at the last sprocket to measure the angular displacement of the output of the actuator (i.e., joint angle). The motor used in the actuator includes Hall-effect sensors which can be used to measure the angular velocity of the motor. The motors are driven by ESCON 50/5 servo-amplifiers [57] which are able to measure total supplied motor current. All of these measurements can be used in a feedback controller that drives the actuators.

Five actuators have been manufactured and function satisfactorily. An assembled actuator can be seen in Figure 2.2 and an exploded view is depicted in Figure 2.3. The actuator described in this section is intellectual property of Cleveland State University

Figure 2.2 Manufactured and assembled actuator

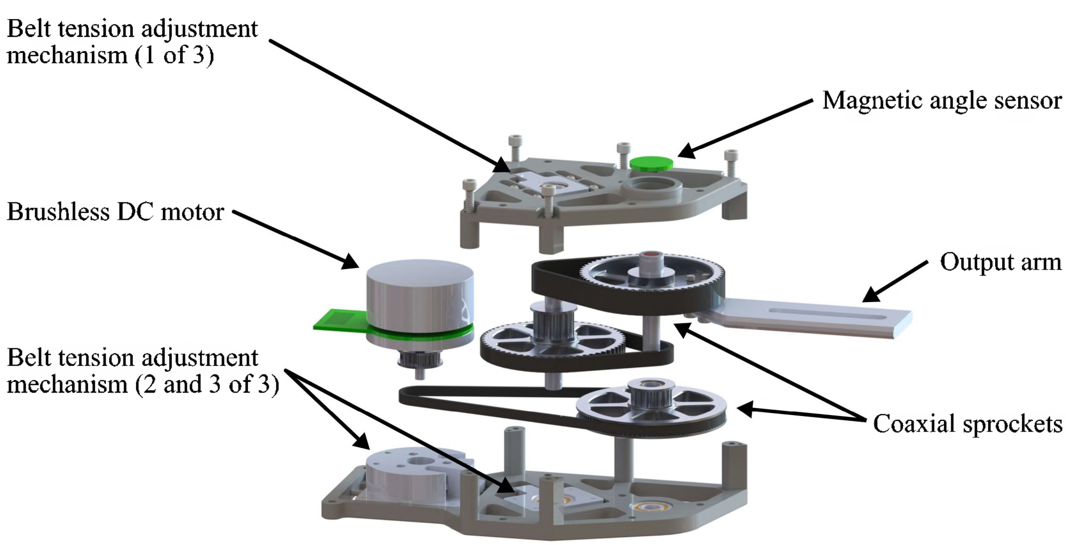

Figure 2.3 Exploded view render of the actuator

with patent pending [58]. A summary of the main features and nominal capabilities of the actuator are presented in Table V.

2.3 Design of the Anthropometrically Parametrized Orthosis

The powered orthosis described here takes inspiration from the Indego exoskeleton from Parker Hannifin [41]–[43] and was developed in collaboration with the Parker Hannifin Human Motion and Control team. As stated in the design requirements summarized in Table IV, the orthosis presented in this dissertation uses parametric modeling to create a device that is specific to a child. The model of this anthropometrically parametrized orthosis is based on anthropometrics of a child measured by a therapist or clinician and will produce a model that is particular to the child. This is accomplished using a four-step process. First, the therapist or clinician will take measurements of the child, forming a set of measurable anthropometrics. Second, these anthropometrics are supplied to a body model to create a complete the set of necessary anthropometrics, including unmeasured variables. Third, these anthropometrics are then used to calculate a set of key orthosis parameters. Fourth and last, these key

Table V. Summary of the main features and nominal capabilities of the joint actuator

Powered using a Maxon EC 45 flat brushless DC electric motor
Three-stage toothed-belt transmission used to increase output torque by 40.6:1
Design incorporates co-axial sprockets to keep the design small
Screw-adjustable belt tensioning mechanisms can be used to tune for performance
Design includes magnetic angle sensor to measure output angle
Range of motion of the output is from –30 to 110 deg
Nominal output operating speed is 375 deg/s based on motor rating
Continuous output torque is 5.4 N·m based on motor rating
Stall output torque is 35.7 N·m based on motor rating
Nominal output power is 70 W based on motor rating
Actuator has a 46 mm thickness, 79 mm width, and 0.6 kg weight

orthosis parameters are used to define the model of the orthosis frame specific to the child in which it is designed for. Once produced using additive manufacturing techniques and assembled, the orthosis frame should be checked for how well it fits the subject.

The first two steps involve obtaining the set of necessary anthropometrics of the child. A set of measurable anthropometrics has been determined based on what child anthropometrics are available in the literature [59] and what was necessary for creating the set of key orthosis parameters. By using the anthropometrics of the child to create the orthosis model, the design can automatically account for the large range and changes in the weights, heights, geometry, and mass distributions of the child; this will include any sex- or age-based differences between subjects in the population. In addition, there can be some adjustment to the anthropometrics to account for any anatomical or physiological abnormalities that may be present. A list of anthropometrics can be found in Appendix A and can serve as a template for obtaining a set of measurements for a subject. Note that not all anthropometrics are inherently measurable; the anthropometrics in the set above are typically found from referencing bone structures. For instance, the knee height, defined here as the rotation axis of the knee, can easily be obtained from the closely located tibiale height, which here is referenced as the indenting point between the tibia and femur. By using a body model, some variables such as this can be calculated from the easily measurable anthropometrics. A statistical body model [60] could also be used to improve the calculation and detect incorrectly measured anthropometrics by accounting for the statistical relation between anthropometrics observed in the population, though only a simple algebraic model is used here. With the measured anthropometrics available, then a complete set of anthropometrics is formed by applying a body model, filling in the unmeasured anthropometrics necessary for creating the set of key orthosis parameters.

The last two steps involve defining and creating an orthosis model. The orthosis frame is primarily composed of three kinds of parts: a single hip cradle, two thigh components, and two shank components. The hip cradle wraps around the lower portion of the torso and connects the two legs of the orthosis together. The hip cradle includes a free adduction-abduction hip DOF at each of these connection points to allow for the subject to naturally walk and self-balance. The thigh component has two cuffs which partially wraps around the thigh of the user. Each cuff includes webbing slots for strapping the user in, keeping the exoskeleton thigh component closely mechanically coupled to the thigh of the user. Each thigh component houses two actuators to supply flexion-extension torque at the hip and knee joints. The actuator arms at the hips are used to connect to the hip cradle, and the actuator arms at the knee are used to connect to the shank components. The shank component also has two cuffs to wrap around the shank of the user. Similar to the thigh, each cuff also includes webbing slots. For this prototype version of the orthosis, a battery and other electronics are not embedded in the device and are external at this stage of development.

The frame of the anthropometrically parametrized orthosis is parametrically defined in terms of a set of key orthosis parameters. Each of the key orthosis parameters can calculated based on the complete set of anthropometrics. Most of these calculations are straightforward, such as the hip cradle breadth being proportional to the waist breadth. However, some care must be taken to check for compatibility of dimensions. For instance, if the hip breadth is too large, then some of the key orthosis parameters are modified such that the plane in which the actuator arms lie is shifted laterally to avoid the interfering components. A schematic of the orthosis with an outline of various key orthosis parameters can be seen in Figure 2.4. Once the full set of key orthosis parameters is determined, the orthosis frame model can be created for the particular child. For demonstration, this process is applied using anthropometrics available in the literature for average children ages 6, 8, and 11 years old [59], and rendered models can be viewed in Figure 2.5. An exploded view is depicted in Figure 2.6, showing each of the main components of the orthosis: a single hip cradle, two thigh components, two shank components, and four actuators. The actuators are reusable components of the orthosis and can be used for any particular fabrication of the anthropometrically parametrized orthosis since the orthosis frame is designed such that the actuator can be inserted regardless of the anthropometrics used. The plastic pieces of the hip cradle, thigh components, and shank components will need to be periodically redesigned based on this four-step process to refit the child as he or she grows.

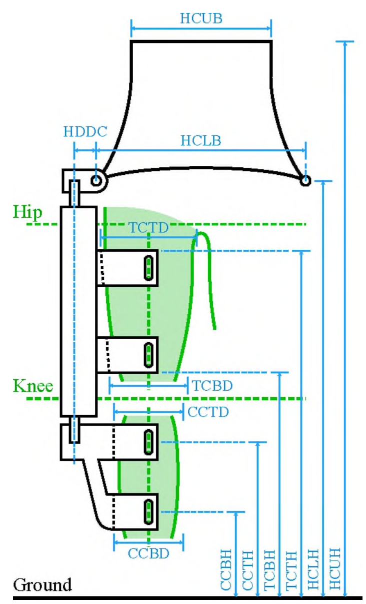

Figure 2.4 Partial schematic of the orthosis with some key orthosis parameters

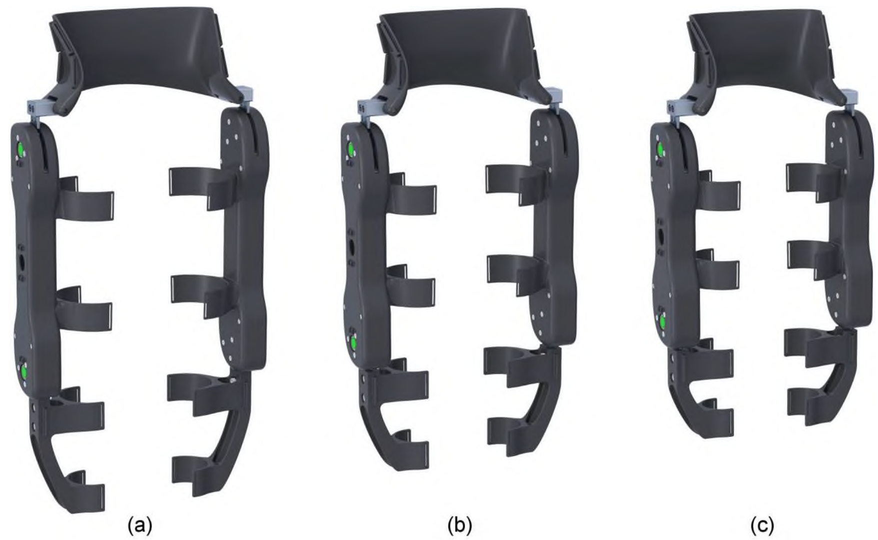

Figure 2.5 Rendered orthosis models for average children ages (a) 11, (b) 8, and (c) 6 years

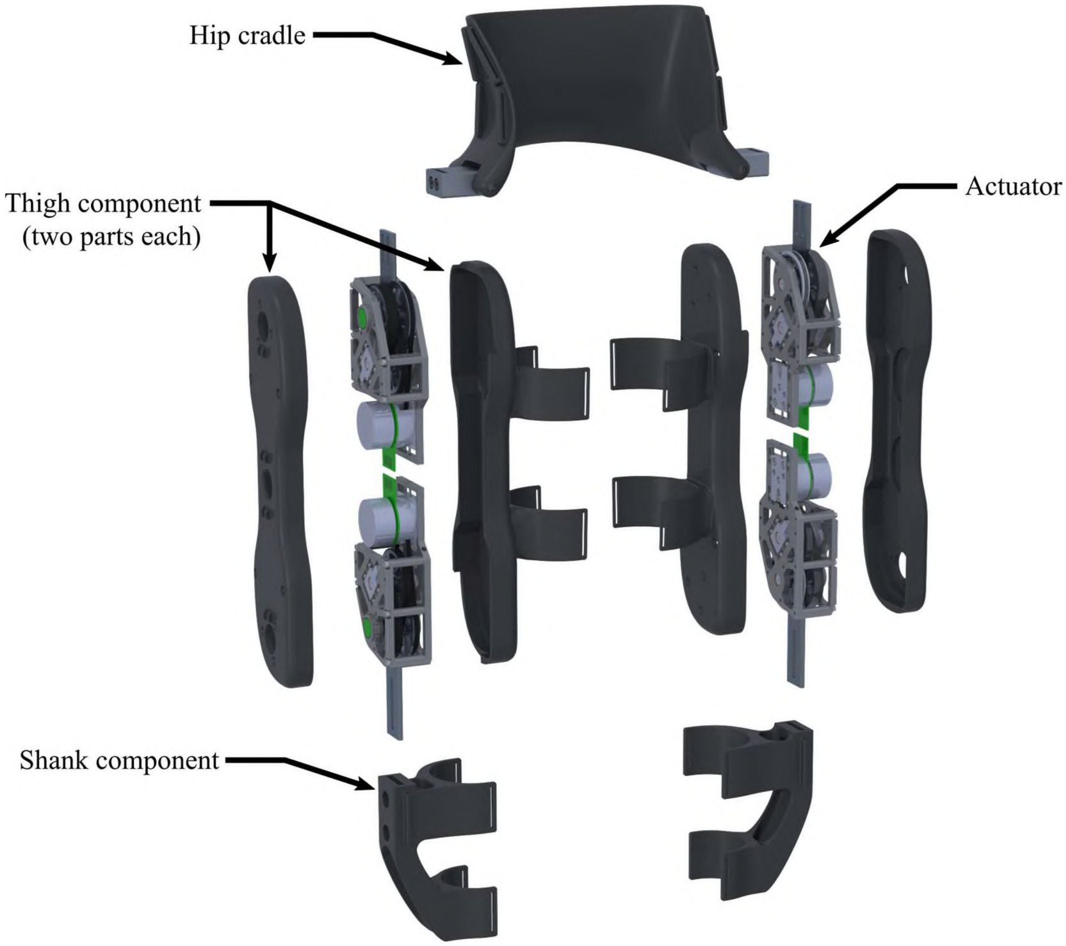

Figure 2.6 Rendered exploded view of the main orthosis components

Although this process was developed for the anthropometrics of children ages 6 to 11 years, the methodology also applies to adults and is compatible with the anthropometrics of some adults. The four steps for creating a model were applied to a healthy 27 year old adult. Anthropometrics were measured and then supplied to a body model. The complete set of anthropometrics was then used to calculate the key orthosis parameters which were used to create a model of the orthosis. This model was then deployed to fabricate a prototype of the orthosis, which can be seen in Figure 2.7. The plastic frame of the prototype was manufactured using the stereolithography additive manufacturing technique with Accura® Xtreme White 200, a polypropylene-like material

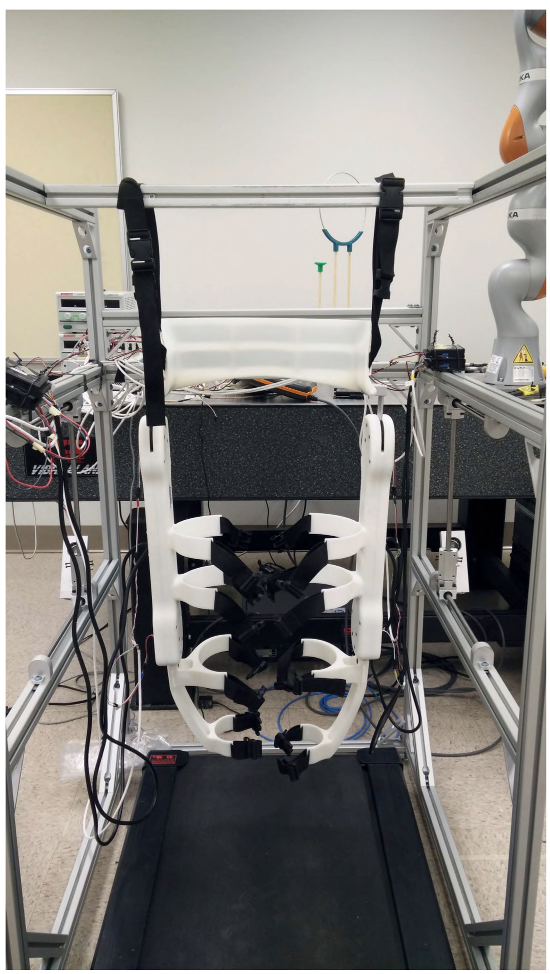

Figure 2.7 Fabricated and assembled orthosis for an adult

which allows for some compliance when put under load for safety and user comfort purposes. The cost of the manufactured orthosis frame was $5,500. With each actuator costing $2,200, the total orthosis cost was approximately $14,300, which excludes the servo-amplifiers, cables, and miscellaneous parts.

The orthosis will occasionally need to be re-fitted to the child as they grow, requiring a new set of measurements for the parametric model and a newly fabricated orthosis frame. It is expected that the orthosis will need to be re-fitted to the child roughly every one to three years, which is typical for children wearing AFOs [61]. This would mean about four device frames will need to be fitted to a child as he or she grows from 6 to 11 years of age before transitioning to an adult orthosis. As the child grows and body segment lengths increase over time, and the link lengths of the orthosis will begin to mismatch the corresponding body segment lengths of the child. Also, cuff sizes will start to poorly fit the child at some point in growth. The child may feel less comfortable using the device as they grow, and complaints of discomfort can serve as an indicator that it is appropriate to re-fit the orthosis. In addition, a worsening in gait or general functional use of the orthosis can also indicate that a re-fitting of the orthosis frame is necessary. When sizing the orthosis, it will be desirable to oversize the link lengths and cuff sizes by some margin. This will allow for the child to grow into the device, permitting longer use of the orthosis prior to needing a new orthosis frame. Note that oversizing the device can result in misalignment of the child and orthosis knee axes, which can increase interaction forces and torques at the thigh but can be partially compensated with control [62].

CHAPTER III

PRELIMINARY PERFORMANCE EVALUATION OF THE ACTUATOR AND PROVISIONAL ORTHOSIS

This chapter presents the preliminary work on experimentally evaluating the actuator and orthosis. First, some testing equipment and a testing platform are designed to facilitate performance evaluation of the actuator in a provisional orthosis. Second, the electronics and hardware used for performance evaluation are implemented and integrated. Third, an actuator is subjected to bench-top testing for assessing speed and torque capabilities. Fourth, the actuators are evaluated for their ability to perform gait tracking in a provisional orthosis. Lastly, control strategies are explored for standing balance and are applied in simulation and experiment. Actuator bench-top testing results presented in Section 3.3 and gait tracking results presented in Section 3.4 are based on the results published in [63]. Standing balance results presented in Section 3.5 are submitted for publication in [64].

3.1 Design of the Testing Equipment and Testing Platform

In order to evaluate the actuators in an orthosis prior to human subject testing, some testing equipment and a testing platform were developed. The testing equipment consists of a dummy and provisional orthosis, and the testing platform is a gantry-like system with a treadmill. They can be used together to allow early evaluation of the actuators and orthosis as a whole prior to fabrication of the anthropometrically parametrized orthosis and without human subject testing.

The dummy and provisional orthosis have been designed to be simple and function together. The dummy consists of a hip bridge, two thighs, and two shanks, with each component designed to make the addition of weights easy. This allows for adjusting the weight of the dummy body segments to represent children of different weights. The hip bridge is an aluminum bar with mounting holes for connecting to the provisional orthosis and mounting strut channels, which are used for attaching additional weights. These weights represent the collective weight and inertia of the head, arms, and torso of the dummy. The thigh and shank body segments of the dummy are also aluminum bars with mounting holes for connecting to the provisional orthosis and mounting slots for attaching additional weights. The hip and knee joints use clevis pins with hairpin cotter pins to connect the body segments together, restricting motion to the flexion-extension DOF at the joints. The College Park Truper prosthetic foot [65] is used for the ankle and foot, and acts as a stiffness and damping in the dorsiflexion-plantarflexion DOF, which should roughly represent ankle behavior of a person, albeit without performing positive work [66]. The dummy is sized based on the height of an average 8 year old child of about 131 cm [46] with body segment lengths proportional to this based on [67]. These values can be found in Table VI, in addition to the segment masses of the dummy without any additional weights.

The provisional orthosis has been designed to function with the dummy, and consists of a hip cradle, two thigh components, and two shank components. Each component has mounting holes in accordance with the design of the dummy for fastening the dummy body segments with the corresponding links of the provisional orthosis. The hip cradle includes slots for the actuator arms, which connects the hip cradle to the thigh components. Each thigh component fastens two actuators to the link, which are for driving the hip and knee joints within the sagittal plane. The shank component is a small connector for fastening the actuator arm driving the knee to the shank body segment of the dummy. The net weigh of the provisional orthosis is 5.1 kg. This does not include electronics since the servo-amplifiers and electrical power source are external in the provisional orthosis.

The testing platform has been designed as a testbed for the provisional orthosis operating with the dummy. It is custom-designed using ready-made aluminum t-slots, so it is heavy enough to remain stationary when the provisional orthosis is operating but light enough to be easily relocated as needed. In addition, t-slots allow for easy adjustment in position and mounting location, permitting easy alteration for future use cases if reconfiguration is necessary. It is designed to be tall enough to include an

Table VI. Segment lengths and masses

Link	Segment	Segment Length L_i (m)	Dummy Segment Mass (kg)	Provisional Orthosis Segment Mass (kg)
1	Shank	0.300	1.2	0.3
2	Thigh	0.301	1.2	1.8
3	Torso	0.472	0.3	0.9

overhead strut from which to hang the orthosis. It also includes guide rails which can optionally be used to restrict the motion of the orthosis and dummy to move within the sagittal plane. The testing platform includes an optional treadmill which can be used for testing the device with ground interaction when walking. Figure 3.1 shows the dummy fastened to the provisional orthosis hanging in the testing platform when fastened to the guide rails.

3.2 Implementation and Integration of Electronics and Hardware

The motors in the actuators are driven using servo-amplifiers, which can operate either in speed-controlled or current-controlled modes and require an input voltage signal for the desired current or velocity. The servo-amplifiers are configured to operate in the current-controlled mode and use internal proportional-integral-derivative current controllers, which were tuned automatically using provided ESCON Studio software

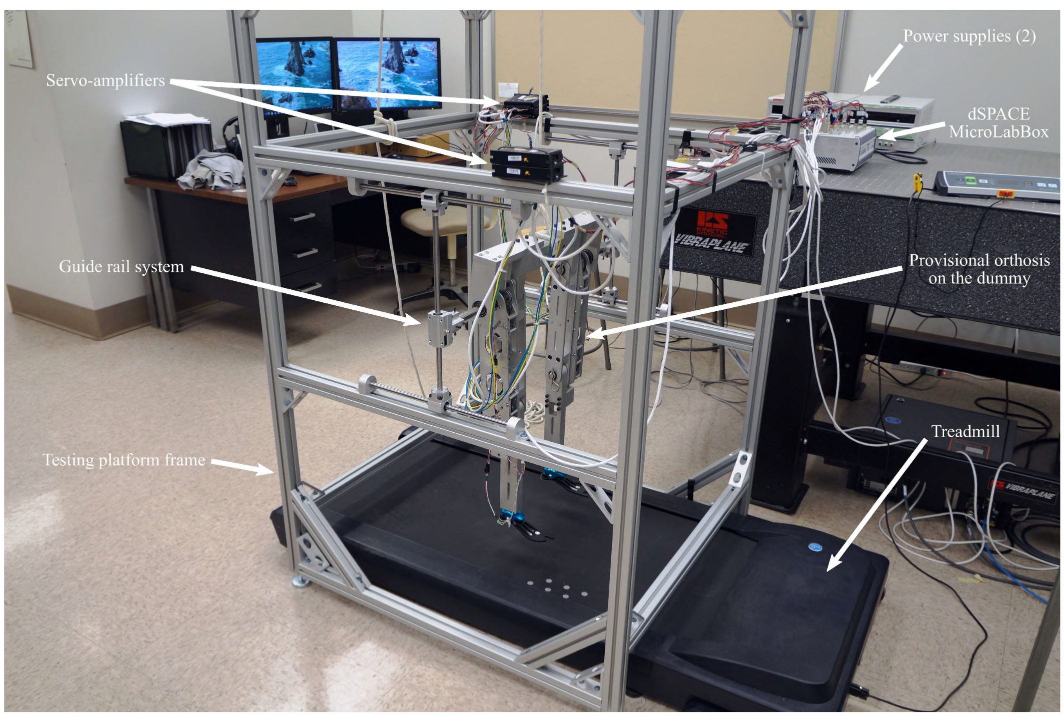

Figure 3.1 Provisional orthosis fastened to the dummy on the testing platform

[57]. The servo-amplifiers output a signal for the velocity of the motor, measured using the motor-integrated Hall-effect sensors, and a signal for the total drawn current. Each actuator incorporates a magnetic angle sensor (MAS) which produces a pulse-width modulated signal with duty cycle proportional to the absolute angular position of the output of the actuator, which represents the joint angle.

A reprogrammable inertial measurement unit (IMU) has been used to measure linear acceleration and angular velocity along the three cardinal directions on whichever link of the orthosis it is attached to. By incorporating this additional sensor, the link orientation for one of the orthosis links can be determined. In conjunction with the measured joint angles, full configuration of the orthosis can be calculated. As a result, the orientation of each link within the sagittal plane and the angle of each joint, including the ankle joint, can be calculated. The IMU was programmed to send a sequence of signed 16-bit integers in a transistor-transistor logic (TTL) serial interface, later converted to a UART RS232 bus, for acceleration along two axes and angular velocity in the orthogonal axis. It is configured to operate at a baud rate of 115,200 bits per second, which works out to sending packets of data at a frequency about 0.9 kHz when operating at full speed. This was chosen to work with a controller operating at 1 kHz, a value slightly faster as to avoid endlessly filling a buffer with data.

These signals, namely motor velocity, motor current, joint angles, and IMU serial data, are all connected to dSPACE MicroLabBox for data acquisition and control. The dSPACE configuration is set to provide a desired current (i.e., torque) signal to the servo-amplifiers. The dSPACE hardware is configured to work with five actuators concurrently, which allows for operating the four actuators in the orthosis plus an extra actuator for testing purposes. dSPACE is configured to operate at 1 kHz, which should be more than adequate for controlling the orthosis. It was programmed using dSPACE Simulink real-time packages and interfaced with using ControlDesk software. The dSPACE hardware is shown in Figure 3.2.

The IMU is ultimately used for obtaining the orientation of a link within a plane. However, pure integration of the angular velocity as measured by the gyroscope in the IMU results in undesired drift. To resolve this issue, this gyroscope measurement, which is accurate at high frequencies, is combined with orientation measurements using the accelerometer, which is accurate at low frequencies. The orientation of the IMU, and therefore the link on which it is attached, is found by adding the gyroscope-based measurement passed through a high-pass filter with the acceleration-based measurement passed through a low-pass filter with the same bandwidth. The selection of the bandwidth was determined experimentally by comparing the IMU orientation to the MAS measurement when the IMU is attached to the arm of the actuator, as shown in

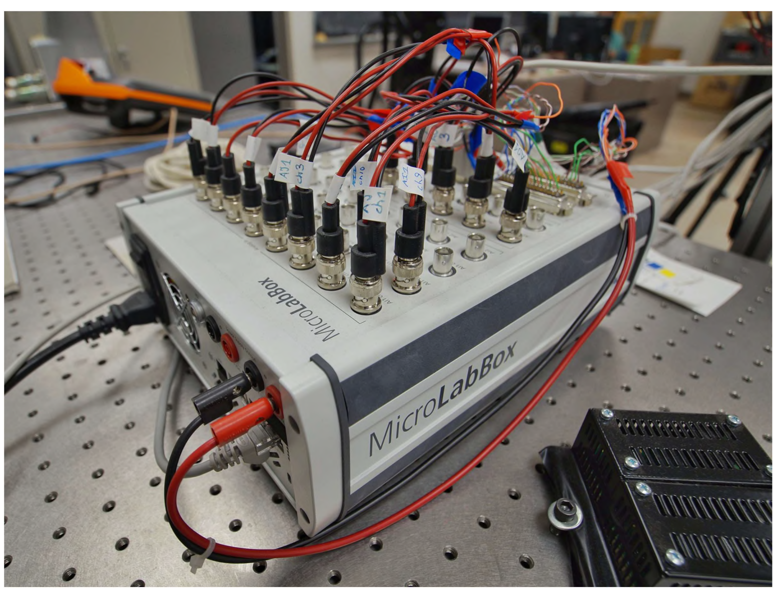

Figure 3.2 dSPACE MicroLabBox for data acquisition and control

Figure 3.3. A sinusoidal signal of varying frequency is set as the desired joint angle and controlled using a proportional-derivative (PD) control law. The comparison between the MAS and IMU measurements are depicted in Figure 3.4. The bandwidth was manually selected to be 0.065 Hz, which seemed to give the best agreement between the MAS measurement and IMU orientation measurement, which was about 0.284 deg of root-mean-square (RMS) error.

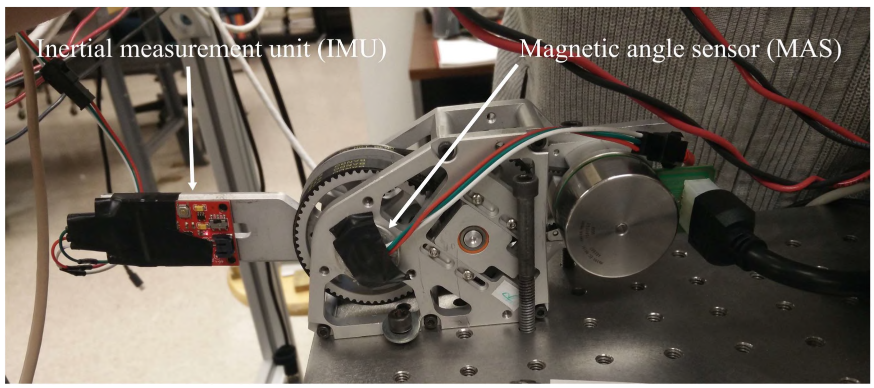

Figure 3.3 Experimental set up for comparing MAS and IMU measurements

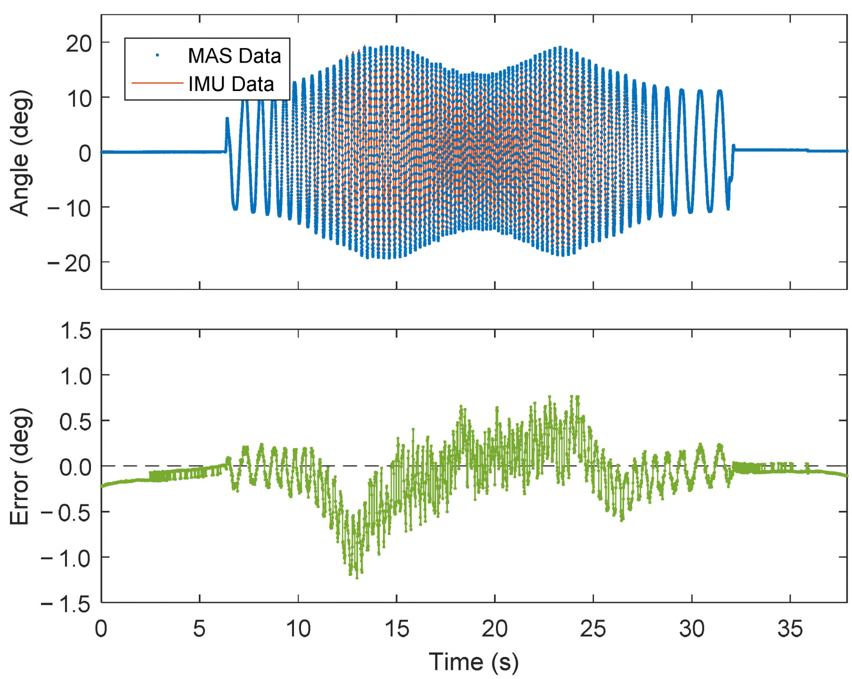

Figure 3.4 Experimental results comparing MAS and IMU measurements

3.3 Joint Actuator Capabilities

The actuator underwent basic testing to determine its capabilities. The power source for the servo-amplifier was set to the motor's nominal voltage rating of 48 V. First, the actuator speed was evaluated. With the actuator arm removed to allow for free rotation, the supplied motor current was increased until it ran up to a maximum speed of 480 deg/s. This was tested in both directions. For comparison, the maximum joint speed for an average healthy gait for the hip and knee is 159 and 369 deg/s, respectively.

Second, the static output torque capability of the actuator was evaluated. With the actuator arm attached, constant current was supplied to the motor at incrementally larger values from zero to four times the continuous current rating of the motor of 0.935 A. A force gauge was attached to the actuator arm, preventing motion in the actuator and measuring a value for the output torque. The resulting motor torque vs. output torque is reported in Figure 3.5 and appears as an approximately linear relation below the ideal transmission line. This is expected, as friction will reduce the amount of torque the actuator can transmit from the ideal friction-free value. The actuator is capable of achieving 4.2 N·m of continuous torque and at least 17.2 N·m of peak torque. Note that for each increment, current was supplied for more than one second due to the response time of the force gauge being about one second. Due to the nature of this experiment, this limited the tested peak torque since higher currents supplied for longer than one second could potentially damage the motor. The actual peak torque capability of the actuator is likely larger than the reported 17.2 N·m.

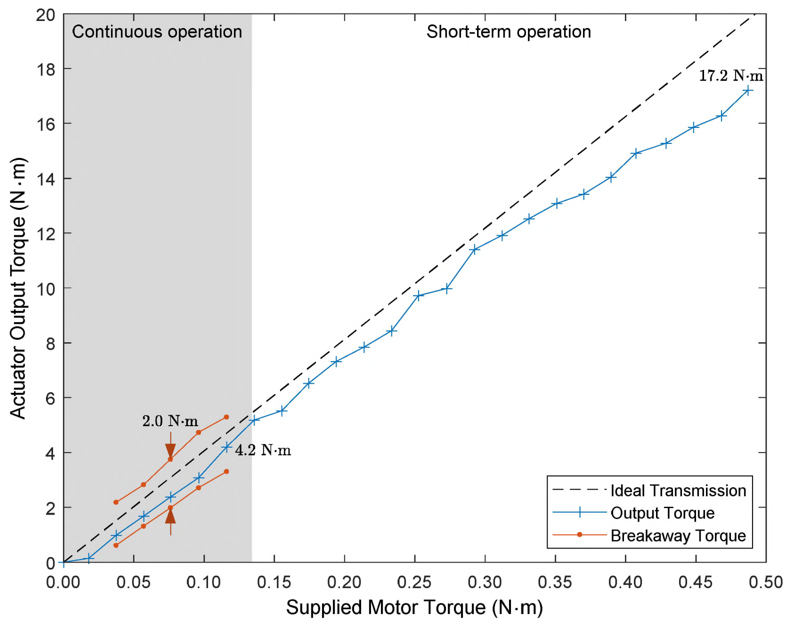

Figure 3.5 Actuator output torque vs. supplied motor torque in a motor stall test with incrementally increasing torque levels and breakaway test

Backdrivability of the actuator can be primarily characterized in terms of friction and inertial effects. In addition to the static output torque experiment, the level of friction was measured by finding the breakaway torque necessary to move the actuator when a constant current within the continuous operating region is supplied to the motor. This was accomplished by slowly reducing or increasing the amount of force at the force gauge by hand until the actuator started to move. This was done in both directions and gives some approximate accuracy bounds to the measured output torque, at least for the tested continuous-operation region, and is illustrated Figure 3.5. The average half-difference of the breakaway torque between the two tested directions can be used to estimate static friction, which is about 1.0 N·m.

Third, friction was measured in the non-static case when the actuator was set up with actuator arm removed. This was carried out for both a low- and high-tension belt states, though this is left without quantification due to lack of means to measure the tension in the belt. The motor operated at various constant speeds up to 400 deg/s in both directions, and electrical current drawn by the motor was recorded and is used as an estimate for the friction torque in the actuator. The current measurements did not vary significantly when changing the operating speed. This suggests that Coulomb friction is the dominant contribution for friction versus viscous friction, at least for the tested speeds. The friction torque at the output of the actuator is measured as 0.8 N·m and 1.1 N·m for the low- and high-tension states, respectively. This closely matches the measured 1.0 N·m static friction torque measured in the previous experiment and is within expected error.

For comparison purposes, the main results of this section are reported in Table VII along with reported values for the Indego exoskeleton. The reported continuous torque rating of the Indego is approximately 2.8 times larger than the tested value for the Cleveland State University actuator. Similarly, the reported maximum short-term operation torque for the Indego is approximately 2.3 times larger than the tested value for the Cleveland State University actuator. Comparing to an average adult weighing roughly 82 kg [46], torques are expected to be approximately 1.7 to 3.4 times larger than children in the target age group from 6 to 11 years.

Table VII. Summary of actuator capability results and comparison to Indego

	Cleveland State University Actuator	Indego Actuator [43]
Maximum no-load speed	480 deg/s	Not reported
Maximum continuous torque	4.2 N·m	12 N·m
Maximum short-term torque	17.2 N·m†	40 N·m‡
Coulomb friction	~1.1 N·m	Not reported
Viscous friction	~0 N·m·s/deg	Not reported

† For a duration about 1 second

‡ For a duration about 2 seconds

3.4 Gait Tracking with the Provisional Orthosis

Using the provisional orthosis, dummy, and testing platform described in Section 3.1, gait tracking experiments were carried out. The dummy was attached to the provisional orthosis, which had its hip cradle fastened to the top of the testing platform and therefore was fixed. This was to have both legs track a healthy gait without interaction with the ground, which serves as the first evaluation of the actuator in use in an orthosis, albeit a provisional orthosis without ground interaction. This was done for two cases, an unloaded case and a loaded case. For the unloaded case, no additional weights were added to the dummy. For the loaded case, additional weights were added to the dummy to represent an average 8 year old child, which would weigh about 32 kg [46]. Based on available data on the proportion of weight contributing to each body segment and their moments of inertial [67], for an average child this age, the thigh should have a weight and moment of inertia of about 3.2 kg and 344 kg·cm^2, respectively, and the shank and foot combination should have a weight and moment of inertia of about 2.0 kg and 471 kg·cm^2, respectively. For the loaded case, the thigh weighed 3.2 kg and shank weighed 2.2 kg, close to the desired value. The weights were positioned such that the moments of inertia of the dummy body segments closely matched that of the desired value.

The servo-amplifiers are four-quadrant units, meaning they were capable of regenerating power when braking the motors. However, the power supply does not support transferring power in the reversed direction. To avoid this, the supplied power was chosen to operate at 38 V instead of the nominal 48 V, which seemed to resolve the issue where the power supply would automatically shut down during the operation when operating at 48 V, turning off the supplied power to the actuators. Shunt regulators have since been installed in-line with the power source to avoid this issue, but were not yet installed when these gait tracking experiments were conducted.

A decentralized PD controller was used for gait tracking. Average healthy gait data, previously shown in Figure 2.1, with a gait period of 1.1 seconds was used as the desired trajectory. The MAS measurement was used for the proportional term, and the motor velocity, scaled up by the transmission ratio of 40.6:1, was used for the derivative term. Both were passed through a manually-tuned 35 Hz low-pass filter for noise attenuation.

3.4.1 Experimental Results

The same controller gains were used for both the unloaded case and loaded case, and were tuned for the loaded case. The hip proportional and derivative gains were 20 N·m/rad and 2.5 N·m·s/rad, respectively, and the knee proportional and derivative gains were 20 N·m/rad and 1.5 N·m·s/rad, respectively. Results for both the unloaded and loaded cases are illustrated in Figure 3.6.

In both the unloaded and loaded cases, the orthosis was able to consistently track the desired gait trajectories across many gait cycles. During swing phase, which is from around 62% to 100% in gait phase, the joint angles tended to overshoot the desired trajectory due to gravity assisting, particular at the knee. During early stance phase, which is from heel strike at 0% to around 30% in gait phase, the torque supplied by the hip actuator in the loaded case was much larger than in the unloaded case due to the larger moment of inertia. Measures of tracking performance are detailed in Table VIII, which includes RMS position tracking errors, both as absolutes and percent of full scale (FS). In addition, torque performance measures, which includes the peak and RMS torques, over the same timespan are detailed in Table IX, both as absolutes and percent of the tested continuous torque (CT, 4.2 N·m) or peak torque (PT, 17.2 N·m). These were taken over six gait cycles.

The gait tracking RMS errors were less in the unloaded case than the loaded case. This is not surprising, given the same controller gains were used in both experiments and there was additional mass on the body segments in the loaded case. The maximum RMS

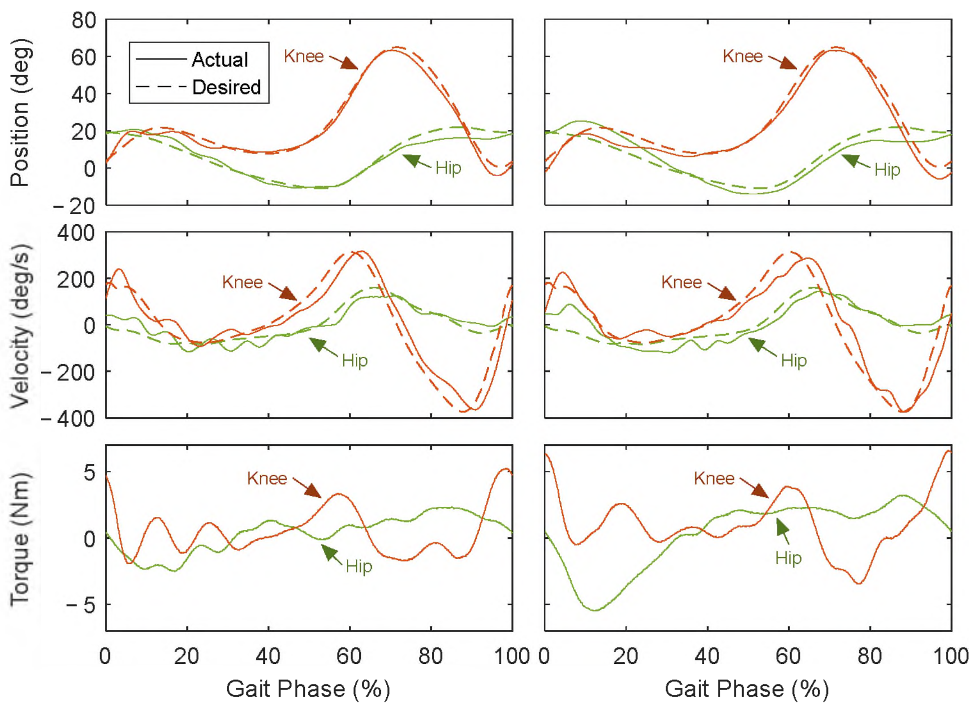

Figure 3.6 Gait tracking results for the (left) unloaded case and (right) loaded case

Table VIII. Joint position errors for both unloaded and loaded cases

	Unloaded Case	Loaded Case
Hip RMS Error	3.0 deg (9% FS)	5.1 deg (15% FS)
Knee RMS Error	2.7 deg (4% FS)	3.9 deg (6% FS)

Table IX. Joint peak and RMS torques for both unloaded and loaded cases

	Unloaded Case	Loaded Case
Hip peak torque	2.5 N·m (15% PT)	5.5 N·m (32% PT)
Knee peak torque	5.3 N·m (31% PT)	6.6 N·m (38% PT)
Hip RMS torque	1.4 N·m (33% CT)	2.6 N·m (61% CT)
Knee RMS torque	1.8 N·m (43% CT)	2.3 N·m (56% CT)

tracking error occurred at the hip in the loaded case at 15%. This tracking error is reasonable when observed in Figure 3.6 as the experimental data appear to approximately follow that of healthy gait patterns. Higher gains could be used to enforce the reference trajectory if desired. However, the primary purpose of this experiment was to validate the basic gait tracking capability of the actuators in an orthotic setting prior to use with subjects, which does not require very accurate gait tracking or high gains. The gait tracking experiment accomplished this objective. Note that when working with able-bodied subjects, higher gains are often undesirable since come compliant motion allows for the subject and orthosis to cooperate.

The largest peak torque was less than the tested peak torque capabilities of actuator. Similarly, the largest RMS torque was less than the tested continuous torque capabilities of the actuator. These results suggest that better tracking performance could have been achieved by increasing the controller gains at the cost of larger torques. However, the controller gains and gait cycle period selected in these experiments were limited due to observed erratic behavior that was more prevalent with higher controller gains and faster gait cycle.

3.4.2 Discussion and Conclusions

This set of experiments show that the actuators can be used to successfully track gait in a provisional orthosis on a dummy representing an 8 year old child. For the unloaded dummy, RMS gait tracking performance was measured as 9% of full scale for the hip and 4% for the knee. For the loaded dummy to represent an average 8 year old child, RMS gait tracking performance was measured as 15% for the hip and 6% for the knee. The successful tracking of gait indicates that the actuators are likely feasible devices to use in an orthosis with subjects and shows potential for rehabilitation and gait assistance in children at least 8 years old.

A number of issues were encountered in the gait tracking experiments. First, belt tension had a significant effect on the performance of the actuator. With the belt tension set too high, the actuators were much less compliant than when set low. In addition, friction levels were higher and the actuator made noises during operation with high belt tensions which were otherwise not heard when the belt tension was set lower. This can possibly be explained by imperfect meshing of the teeth in the sprockets and belts, which could have been exacerbated by the belt tension being too high. Second, it was difficult to set the belt tension in the actuators to levels of similar values without a means to directly measure the belt tension. Belt tensions in the aforementioned experiments were tuned manually until frictional resistances were similar when backdriving the actuator by hand. Third, erratic behavior was sometimes observed when conducting the gait tracking experiments. This was more prevalent when operating at faster gait periods or higher controller gains, and thus limited the chosen gait period and controller gains. The cause of this erratic behavior was later discovered as a bug in the servo-amplifiers where they tracked the incorrect sign of the desired current for a brief period of time; this has since been resolved. Lastly, one major limitation of this experiment is the lack of environmental interaction such as ground reaction forces when walking and the unrealistic scenario of the hip being pinned to ground, and partially motivates the next section on standing balance.

Further work [68] extended these experimental results on the same hardware set up but with the addition of an IMU and an extended Kalman filter to try to improve state estimation and tracking performance. Results for placing the IMU on the shank or thigh were each compared to no IMU. The conclusion was that, when using the extended Kalman filter, no benefit was gained with the addition of the IMU measurement to the MAS measurements.

3.5 Standing Balance of the Provisional Orthosis

Current exoskeleton designs often rely on the wearer using crutches, walkers, or hand rails when using the device, such as the Indego [41] and ReWalk [69] exoskeletons. Other devices, such as the Rex exoskeleton [70], have been designed to avoid the issue of balance altogether as they are self-supporting. However, this comes with the drawback of having slow operation, which can result in unnatural motion for the subject. Individuals with more severe gait impairment from CP, for example, can show poor standing balance [71]. Implementation of a controller that can balance a user can be beneficial for those with limited self-balancing ability. In the initial pursuit of this, this section covers the investigation of standing balance control strategies using the pediatric orthosis as a test platform.

In general, a robotic system is considered balanced if the components in contact with the ground are capable of providing the necessary reaction forces and torques, even during motion, without inadvertently partially or completely lifting off the ground. For the dummy-orthosis system, this would require the feet to remain in complete contact with the ground when applying a standing balance controller to the system. This is an interesting problem particularly for this system because it represents an under-actuated triple pendulum system; the hip and knee are actuated joints but the ankle is a passive joint, posing a challenging control problem.

There are a few balance criteria that have been used in the literature for exoskeletons. These balance criteria are usually based on the idea of keeping some calculated or measured point within the support region, which is defined as the convex hull of the points of contact with the ground. The simplest balance criterion is to keep the projected center of mass (COM) within the support region. Although this is easy to compute and check the condition for balance, requiring only geometric parameters, link masses and center of masses, and joint angles, it is limited to slow motion. González-Mejía et al. used this approach for statically balancing their exoskeleton [72]. This approach can be improved by using a simple inverted pendulum model to find the extrapolated COM [73]. This approach was taken by the MINDWALKER exoskeleton for controlling the step width using the hip adduction-abduction DOF for lateral balance [74]. A third condition used for balance is to keep the center of pressure (COP) far from the boundary of the support region. This approach is better than the projected and extrapolated COM approaches as it does not require the assumption of slow motion or a simplified model of the system. However, it does require direct measurement or calculation of the location of the equivalent net ground reaction force. This is easy to do if the feet of the exoskeleton or insoles inserted in the subject's shoes are equipped with a set of force sensors to measure the ground reaction forces. Tsukahara et al. [75] use a COP-based ankle strategy to balance the hybrid assistive limb (HAL) exoskeleton during sit-to-stand and stand-to-sit stance transitions. A closely related concept is the zero-moment point (ZMP) [76],

[77]. This point is defined as the point on the ground where the equivalent reaction horizontal moments are zero, and the point coincides with the COP when the system is balanced. It can be computed using the geometry of the system, link inertial properties, and measurement or estimation of the position, velocity, and acceleration of each joint. Although this does not require force sensors like the COP does, it is limited if used in real-time control since it requires a good model of the system and requires acceleration measurements, which can be inaccurate if obtained using numerical differentiation with a low-pass filter. The ZMP-based balance criterion is often used for trajectory generation and control of fully actuated systems, and is commonly applied to bipedal robots and other kinds of walking robots [78], [79]. Aphiratsakun and Parnichkun [80] use ZMP balance criterion for trajectory generation and a feedback fuzzy logic controller using the error between desired ZMP and measured COP for balance control. For a review on these and other balance strategies used in bipedal robots, see [78], [79].

For the purpose of pursuing standing balance of the pediatric orthosis, the system is treated as an under-actuated triple pendulum. This section proposes an extension of the work of Azad and Featherstone [81] where the authors control a double pendulum using a momentum-based control law. Motivated by the performance and robustness of their controller to their system, this section covers the direct extension of their work to a triple pendulum system using a similar control law. In the following sections, the model of the dummy-orthosis system will be experimentally identified, and then used for simulations and experiments with a linear-quadratic regulator (LQR) and momentum-based controller (MBC) for standing balance.

3.5.1 System Modeling and Identification

In order to run computer simulations and create a model-based controller, a model of the system must first be determined. The dummy-orthosis system used here is a triple pendulum system with the hip and knee joints controlled but the ankle joint unpowered. A schematic of this system is shown in Figure 3.7, with link lengths previously tabulated in Table VI and inertial parameter descriptions described in Table X.

3.5.1.1 Theory of System Modeling and Identification

There are two common approaches for obtaining the dynamic model of a serial-link robotic system, the Newton-Euler approach and the Lagrange-Euler approach [82], [83]. Given the geometry of the system and inertial parameters of each link, both approaches have algorithms or methods to programmatically obtain the equations of motion

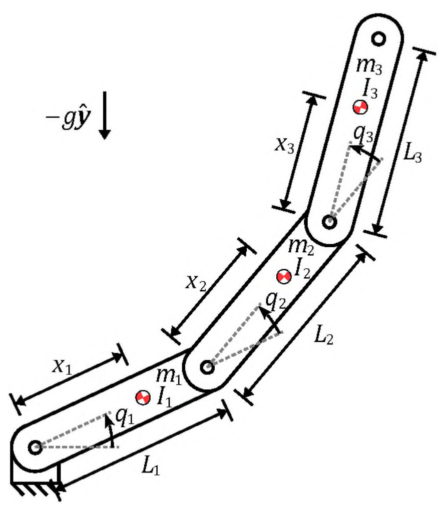

Figure 3.7 Schematic of a triple pendulum system

Table X. Parameter descriptions in the triple pendulum model

Variable	Description
m_k	Mass of link k
x_k	Center of mass of link k from joint k
I_k	Moment of inertia of link k at its COM

symbolically [82], [84], though there is consensus that the Newton-Euler approach is more computationally efficient than Lagrange-Euler approach [82], [84]. For a system with N degrees of freedom, these equations of motion can be written in a form that is linear in the inertial parameters, so that

$$\boldsymbol{u} = \boldsymbol{Y}(\boldsymbol{q}, \dot{\boldsymbol{q}}, \ddot{\boldsymbol{q}})\boldsymbol{\Phi} \tag{3.1}$$

where u is the force-torque input vector, $\boldsymbol{\Phi}$ in the inertial parameter vector, and $\boldsymbol{Y}(\boldsymbol{q}, \dot{\boldsymbol{q}}, \ddot{\boldsymbol{q}})$ is the matrix-valued coefficient which is a function of the joint position $\boldsymbol{q}$, velocity $\dot{\boldsymbol{q}}$, and acceleration $\ddot{\boldsymbol{q}}$ vectors. The algorithms can be modified to give $\boldsymbol{Y}$ and $\boldsymbol{\Phi}$, or this can be done by inspection. When done algorithmically or not carefully with inspection, the columns of $\boldsymbol{Y}$ will be linearly dependent [83], which can be problematic when doing model identification. This can be resolved either symbolically using an algorithm [85] or numerically using QR decomposition [76], modifying $\boldsymbol{Y}$ and $\boldsymbol{\Phi}$ such that the linear dependencies disappear. Note that with the dynamic model written in this form, it can be very easily modified to include more terms other than the nominal robot model, so long as the other terms are linear in the parameters, as is the case with bias torque, viscous friction, and Coulomb friction, to name a few examples.

With the model in this form, $\boldsymbol{Y}(\boldsymbol{q}, \dot{\boldsymbol{q}}, \ddot{\boldsymbol{q}})$ can be found symbolically knowing just the geometry of the system. The parameter vector $\boldsymbol{\Phi}$ contains all of the inertial parameters in the system and must be identified by direct calculation knowing geometry and material properties, with the assistance of computer-aided design software, by disassembling the system and directly measuring the properties of each component separately, or by designing and performing an experiment or series of experiments to identify the parameters. The last option is explored here.

Equation (3.1) holds true for every measured time step throughout an experiment. For an experiment with K measured time steps, every application of this equation can be concatenated together, forming a large system of linear equations:

$$\bar{\boldsymbol{u}} = \bar{\boldsymbol{Y}}\Phi \tag{3.2}$$

where

$$\bar{\boldsymbol{u}} = \begin{bmatrix} \boldsymbol{u}(t_1) \\ \boldsymbol{u}(t_2) \\ \vdots \\ \boldsymbol{u}(t_K) \end{bmatrix}, \quad \bar{\boldsymbol{Y}} = \begin{bmatrix} \boldsymbol{Y}(t_1) \\ \boldsymbol{Y}(t_2) \\ \vdots \\ \boldsymbol{Y}(t_K) \end{bmatrix}$$

are the concatenated input vector and the regressor matrix, respectively. When the inertial parameters $\boldsymbol{\Phi}$ are unknown and to be identified, Eq. (3.2) then represents an overdetermined system of linear equations where $\bar{\boldsymbol{u}}$ is directly measured as the applied joint forces and torques used in the experiment and $\bar{\boldsymbol{Y}}$ is calculated from measured joint positions, velocities, and accelerations. By left-multiplying Eq. (3.2) by the Moore-Penrose left pseudo-inverse $\bar{\boldsymbol{Y}}^{+} = (\bar{\boldsymbol{Y}}^{\mathrm{T}}\bar{\boldsymbol{Y}})^{-1}\bar{\boldsymbol{Y}}^{\mathrm{T}}$, which satisfies the property that the matrix product $\bar{\boldsymbol{Y}}^{+}\bar{\boldsymbol{Y}}$ gives the appropriately sized identity matrix, a closed-form solution for the unknown inertial parameters is found:

$$\Phi = \bar{\boldsymbol{Y}}^{+}\bar{\boldsymbol{u}} \tag{3.3}$$

The closed-form solution given by (3.3) is the solution to the unweighted linear regression problem and gives the best fit solution to Eq. (3.2) in the least-squares sense. That is, if there are measurement errors or the dynamic model does not match reality perfectly so that Eq. (3.2) is not satisfied exactly, the solution given by Eq. (3.3) is the solution that minimizes the vector 2-norm of the difference between both sides.

Note that the trajectory and input used in the experiment cannot be chosen arbitrarily. Enough data samples must be taken for a sufficiently exciting trajectory. That is, the condition number of the regressor matrix $\kappa(\bar{\boldsymbol{Y}})$ should be as small as possible because it bounds the errors in the linear regression solution (3.3) [86]. Note that the aforementioned reduction in the matrix $\boldsymbol{Y}$ is necessary to give a unique solution for $\boldsymbol{\Phi}$, provided enough data are taken for a sufficiently exciting trajectory. Otherwise, there will be the possibility of an infinite or very large condition number, indicating no upper bound on the error for $\boldsymbol{\Phi}$. The main drawback to this approach for identification is that it requires having the joint accelerations available. This is rarely directly measured and must be obtained by numerically differentiating joint velocities. However, since identification is done offline, the data can be processed to improve this estimation and avoid inaccuracy issues typically encountered with numerical differentiation.

The system used here is the triple pendulum system, which has the following nominal dynamic model in the form that is linear in the parameters, after removing linear dependencies:

$$\boldsymbol{Y}_{\mathrm{n}}\left(\boldsymbol{q},\dot{\boldsymbol{q}},\ddot{\boldsymbol{q}}\right)=\begin{bmatrix} gc_1 & \dot{\omega}_1 & Y_{13} & \dot{\omega}_2 & Y_{15} & \dot{\omega}_3 \\ 0 & 0 & Y_{23} & \dot{\omega}_2 & Y_{25} & \dot{\omega}_3 \\ 0 & 0 & 0 & 0 & Y_{35} & \dot{\omega}_3 \end{bmatrix}, \tag{3.4}$$

$$Y_{13}=-L_1s_2\dot{q}_2^2+gc_{12}+2L_1\ddot{q}_1c_2+L_1\ddot{q}_2c_2-2L_1s_2\dot{q}_1\dot{q}_2$$

$$Y_{23}=L_1s_2\dot{q}_1^2+gc_{12}+L_1c_2\ddot{q}_1$$

$$Y_{35} = s_3\left(c_2\left(L_1\dot{q}_1^2 - gs_1\right) - s_2\left(L_1\ddot{q}_1 + gc_1\right) + L_2\left(\dot{q}_1 + \dot{q}_2\right)^2\right)$$
$$+c_3\left(c_2\left(L_1\ddot{q}_1 + gc_1\right) + s_2\left(L_1\dot{q}_1^2 - gs_1\right) + L_2\left(\ddot{q}_1 + \ddot{q}_2\right)\right)$$

$$Y_{25} = Y_{35} + L_2 c_3 \dot{\omega}_3 - L_2 s_3 \omega_3^2$$

$$Y_{15} = Y_{25} + L_1 c_{23} \dot{\omega}_3 - L_1 s_{23} \omega_3^2$$

$$\mathbf{\Phi}_{\mathrm{n}} = \begin{bmatrix} m_1 x_1 + (m_2 + m_3) L_1 \\ I_1 + m_1 x_1^2 + (m_2 + m_3) L_1^2 \\ m_2 x_2 + m_3 L_2 \\ I_2 + m_2 x_2^2 + m_3 L_2^2 \\ m_3 x_3 \\ I_3 + m_3 x_3^2 \end{bmatrix}$$

where $c_j = \cos(q_j)$, $c_{jk} = \cos(q_j + q_k)$, $c_{123} = \cos(q_1 + q_2 + q_3)$, $s_j = \sin(q_j)$, $s_{jk} = \sin(q_j + q_k)$, $s_{123} = \sin(q_1 + q_2 + q_3)$, and

$$\omega_k = \sum_{j=1}^{k} \dot{q}_j \ , \ \dot{\omega}_k = \sum_{j=1}^{k} \ddot{q}_j$$

is the angular velocity and acceleration, respectively, of link k. Direct application of this technique for model identification of the triple pendulum proved difficult in practice and gave poor torque reproduction results with experiments conducted with the fully assembled triple pendulum system. Instead, the model identification problem is split into smaller problems that are easier to solve: finding the ankle stiffness model, the shank single pendulum model, and then the thigh and torso double pendulum model. These are then combined into the triple pendulum model. Each of these are covered in the forthcoming sections.

3.5.1.2 Ankle Stiffness Model Identification

The ankle is a passive, uncontrolled joint with stiffness and damping behavior with different properties when dorsiflexed than when plantarflexed. The difference in these properties is due to different pieces of material on either side of the ankle joint indicated in Figure 3.8. To experimentally identify the stiffness behavior of the ankle, a static displacement test is conducted. The ankle damping is later identified as part of the experiment identifying the shank model in the next section and is not considered in this experiment. For this experiment, the system is the shank with the prosthetic foot attached for the ankle, representing a single pendulum system. The foot was affixed to the ground and the IMU was attached to the side of the link to measure the orientation of the link, which is the ankle angle in this system, using the method described in Section 3.2. An approximately horizontal load was applied to the shank with a known moment arm, as shown in Figure 3.9. The applied weight was incrementally increased to find the displacement as a function of applied load. This was applied in both plantarflexion and dorsiflexion directions. The force load was directly measured using a force gauge to

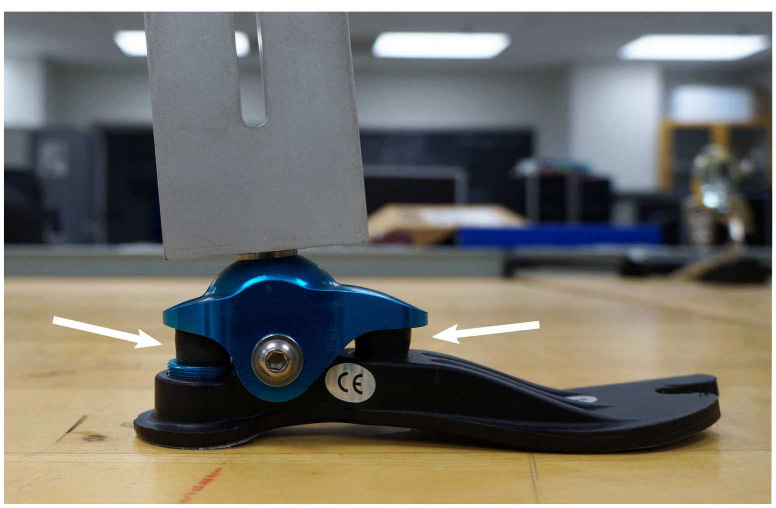

Figure 3.8 The prosthetic foot has different characteristics in the two directions

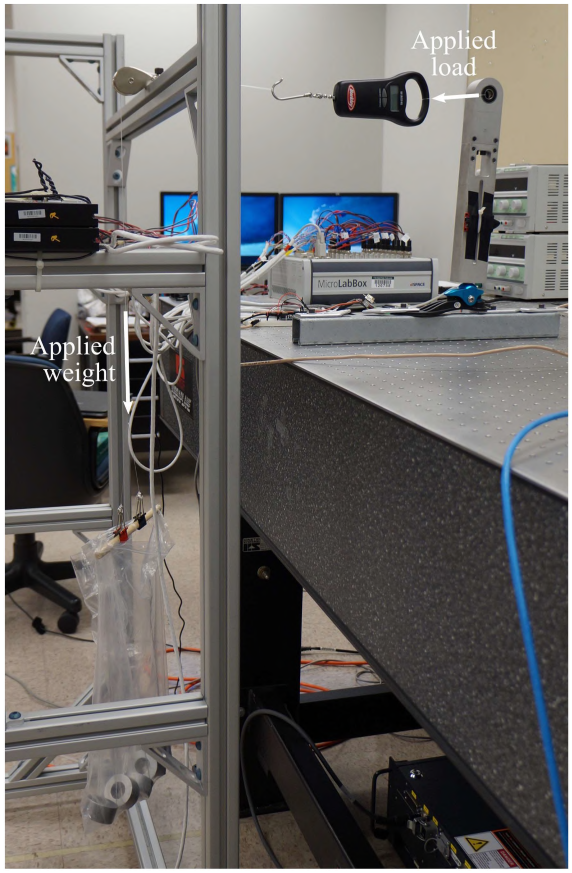

Figure 3.9 Experimental set up for ankle stiffness model identification

avoid inaccuracies from not accounting for frictional losses in the pulley used in the experiment. The displacement versus torque results are presented in Figure 3.10. For large displacements in either direction, the moment required for the observed angle appears affine in the displacement. For smaller displacements, the transition between these affine relations appears to be sigmoid-like curve. This prompts the ankle stiffness model to be a weighted sum of two linear polynomial functions with weights based on a sigmoid function:

$$M_{\mathrm{a}}(\theta) = k_{\mathrm{d}} S\left(\frac{\theta-\theta_0}{\beta}\right)(\theta-\theta_{\mathrm{d}}) + k_{\mathrm{p}}\left(1-S\left(\frac{\theta-\theta_0}{\beta}\right)\right)(\theta-\theta_{\mathrm{p}}) \tag{3.5}$$

where $S(x) = 1/(1 + e^{-x})$ is the sigmoid function and θ is the orientation of the shank relative to the vertical. The unknown parameters k_{d}, θ_{d}, k_{p}, θ_{p}, β, and θ_0 were determined using a quasi-Newton nonlinear numerical optimization solver, where k_{d} and k_{p} respectively represent the ankle stiffness in dorsiflexion and plantarflexion. The resulting values for these parameters are tabulated in Table XI and the predictive trace based on these parameters are illustrated in Figure 3.10. The RMS torque prediction error

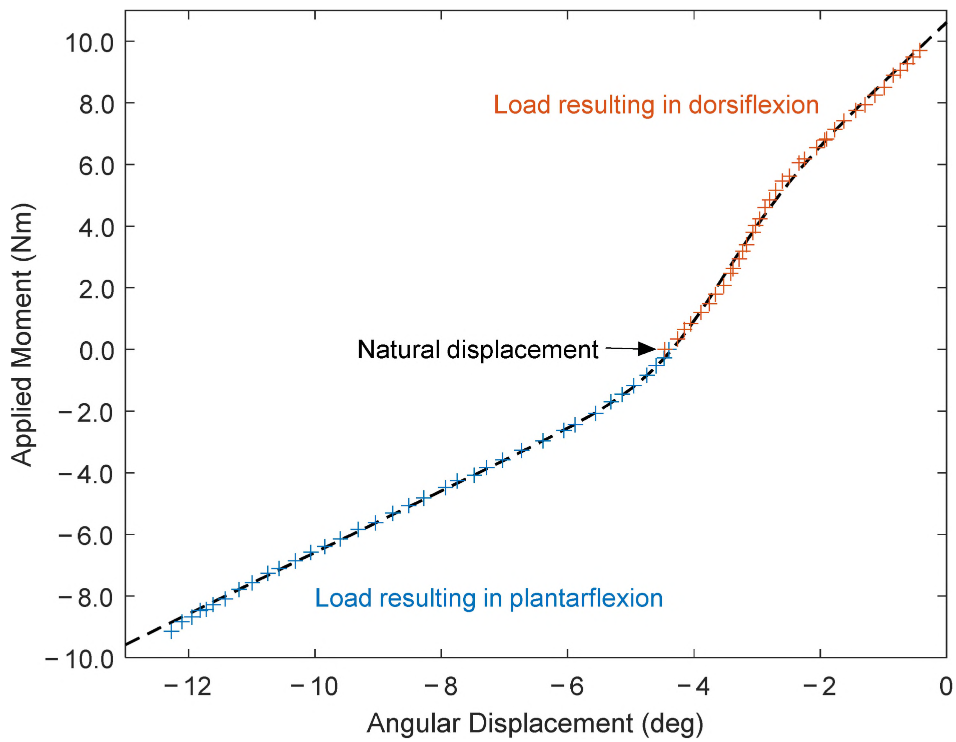

Figure 3.10 Experimental results for ankle stiffness model identification with ankle stiffness model

Table XI. Parameter values in the ankle stiffness model

Parameter	Value	Unit
k_{d}	109	N·m/rad
k_{p}	57.1	N·m/rad
θ_{d}	−0.0978	rad
θ_{p}	−0.0593	rad
θ_0	−0.0665	rad
β	0.0103	rad

with this ankle stiffness model is 0.13 N·m for dorsiflexion and plantarflexion directions combined.

3.5.1.3 Shank Model Identification

The experimental set up for shank model identification is identical to that of the ankle stiffness model identification. That is, the system is a single pendulum pinned to ground at the ankle. The ankle is an uncontrolled joint, so a desired trajectory cannot be tracked for identification purposes. Instead, an initial condition is set by applying a constant load to the system and suddenly releasing it, effectively applying a step response. This is accomplished by applying a horizontal load using a thin cable and releasing it by cutting the cable. This is done twice, once when the ankle is initially dorsiflexed and again when the ankle is initially plantarflexed. The theory described in Section 3.5.1.1 is applied for system identification. The stiffness model found in Section 3.5.1.2 is used as the input to the system after offsetting the supplied angle by 90 degrees. Here, the joint position, velocity, and acceleration vectors contain a single element for the ankle angle relative to the horizontal. The model for a single pendulum is formed as a nominal robot model that has been augmented with viscous damping with different properties depending on whether the ankle is dorsiflexed (d_{ad}) or plantarflexed (d_{ap}):

$$\boldsymbol{Y}_{\mathrm{s}}(\boldsymbol{q},\dot{\boldsymbol{q}},\ddot{\boldsymbol{q}})=\left[\boldsymbol{Y}_{\mathrm{sn}} \mid \boldsymbol{Y}_{\mathrm{sa}}\right]=\left[gc_1 \quad \ddot{q}_1 \mid \langle q_1<q_{\mathrm{r}}\rangle\dot{q}_1 \quad \langle q_1>q_{\mathrm{r}}\rangle\dot{q}_1\right] \tag{3.6}$$

$$\boldsymbol{\Phi}_{\mathrm{s}}=\begin{bmatrix}\boldsymbol{\Phi}_{\mathrm{sn}}\\ \hline \boldsymbol{\Phi}_{\mathrm{sa}}\end{bmatrix}=\begin{bmatrix} m_1x_1\\ I_1+m_1x_1^2\\ \hline d_{\mathrm{ap}}\\ d_{\mathrm{ad}}\end{bmatrix}$$

where

$$\langle P \rangle = \begin{cases} 1 & \text{if } P \text{ is true} \\ 0 & \text{if } P \text{ is false} \end{cases}$$

denotes the Iverson bracket function. The reference position q_r is manually found as the resting position of the shank and is used as the threshold between dorsiflexion and plantarflexion. The result of the two step responses can be found in Figure 3.11. The first brief portion of data were removed from the datasets to avoid interaction effects when cutting the cable and only 2.5 seconds of data were used from each experiment after this point.

Smoothing splines are fit to the measured position data with a manually-tuned smoothing parameter of a value slightly less than one (equal to $1 - 10^{-8}$) and then

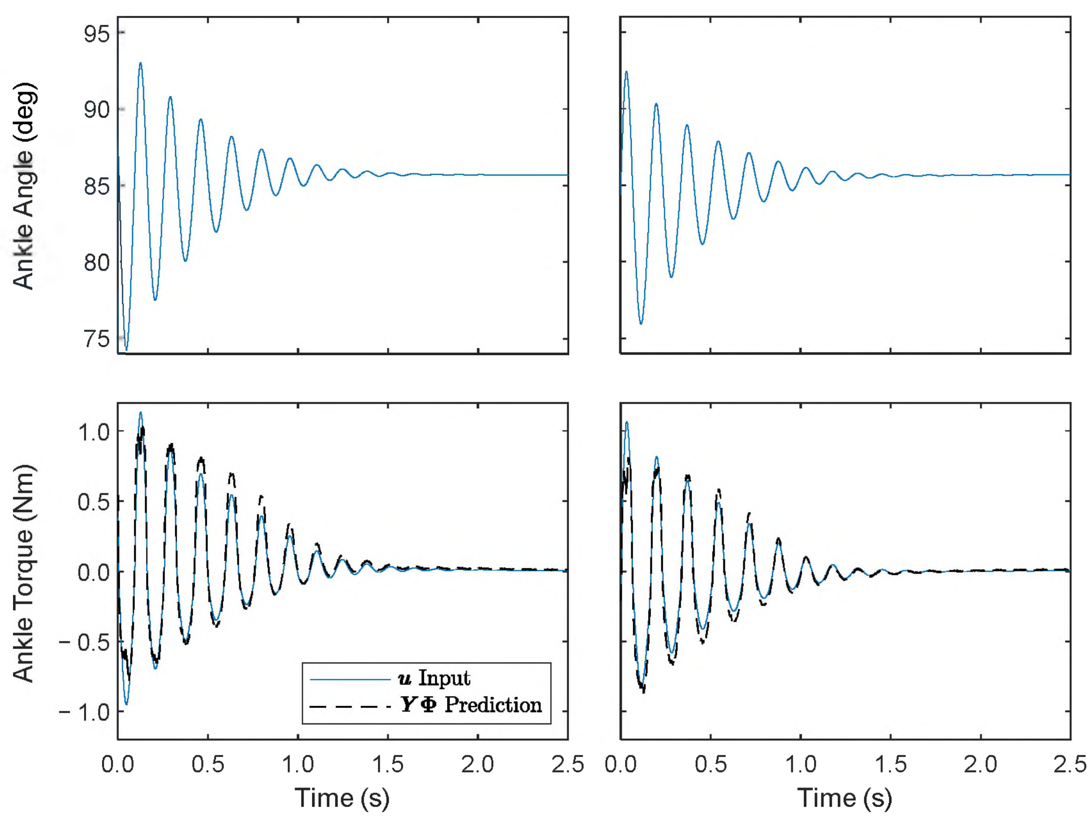

Figure 3.11 Response for (left) dorsiflexion and (right) plantarflexion initial configuration

differentiated once and twice to get angular velocity and acceleration, respectively, for both experiments. The two datasets are then combined into a single dataset and then supplied to Eq. (3.3) for model identification. The resulting parameters from model identification are shown in Table XII and a comparison between ankle stiffness model input torque and the dynamic model of the shank single pendulum system are also shown in Figure 3.11. The condition number was 72.0, smaller than the recommended value of 100 [76], indicating the parameters are not very sensitive to measurement noise and therefore unlikely biased estimates of the true value, assuming the model structure accurately represents reality. The RMS torque prediction error was 0.064 N·m for the combined dataset.

3.5.1.4 Thigh and Torso Model Identification

The assembled dummy-orthosis system was flipped upside down and the shank was rigidly attached to the testing platform, effectively resulting in a double pendulum system shown in Figure 3.12. Since both the hip and knee joints are actuated, this is a fully actuated system and therefore trajectory tracking is possible using a feedback control law. The same model identification theory described in Section 3.5.1, which was used in the shank model identification, is also used here for thigh and torso model identification. Here, the joint position, velocity, and acceleration vectors contain elements for the knee

Table XII. Parameter values in the shank model

Parameter	Value	Unit
$m_1 x_1$	0.00415	kg·m
$I_1 + m_1 x_1^2$	0.00452	kg·m^2
d_{ap}	0.0176	N·m·s/rad
d_{ad}	0.0266	N·m·s/rad

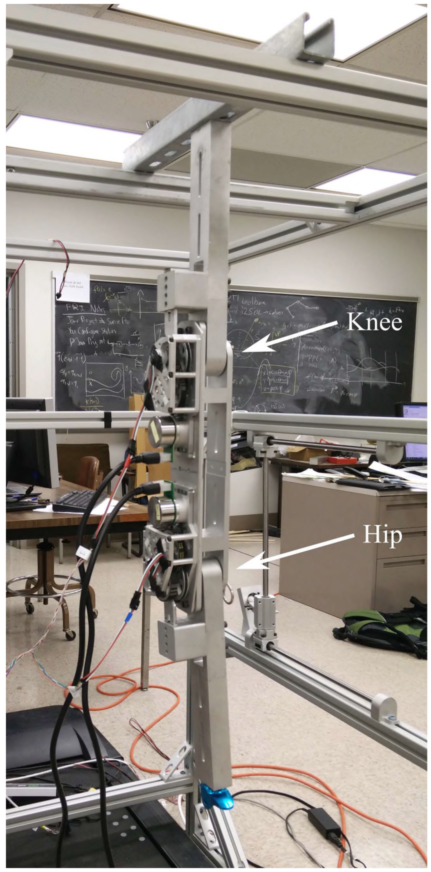

Figure 3.12 Experimental set up for thigh and torso model identification

and hip joints, in that order. The knee angle is relative to the horizontal and the hip angle is relative to the thigh link. The double pendulum model is the nominal robot model plus terms at both joints for viscous friction (d_{k} and d_{h} for the knee and hip, respectively) and torque measurement bias (b_{k} and b_{h} for the knee and hip, respectively).

$$\boldsymbol{Y}_{\mathrm{tt}}\left(\boldsymbol{q},\dot{\boldsymbol{q}},\ddot{\boldsymbol{q}}\right)=\left[\boldsymbol{Y}_{\mathrm{ttn}} \mid \boldsymbol{Y}_{\mathrm{tta}}\right]=\left[\begin{array}{cccc|cccc} gc_1 & \ddot{q}_1 & Y_{\mathrm{tt}13} & \ddot{q}_1+\ddot{q}_2 & \dot{q}_1 & 0 & 1 & 0 \\ 0 & 0 & Y_{\mathrm{tt}23} & \ddot{q}_1+\ddot{q}_2 & 0 & \dot{q}_2 & 0 & 1 \end{array}\right] \tag{3.7}$$

$$Y_{\mathrm{tt}23}=c_2\left(L_2\ddot{q}_1+gc_1\right)+s_2\left(L_2\dot{q}_1^2-gs_1\right)$$

$$Y_{\mathrm{tt}13}=Y_{\mathrm{tt}23}-L_2s_2\left(\dot{q}_1+\dot{q}_2\right)^2+L_2c_2\left(\ddot{q}_1+\ddot{q}_2\right)$$

$$
\mathbf{\Phi}_{\mathrm{tt}} = \left[\begin{array}{c}\mathbf{\Phi}_{\mathrm{ttn}} \\ \hline \mathbf{\Phi}_{\mathrm{tta}}\end{array}\right] = \left[\begin{array}{c} m_2 x_2 + m_3 L_2 \\ I_2 + m_2 x_2^2 + m_3 L_2^2 \\ m_3 x_3 \\ I_3 + m_3 x_3^2 \\ \hline d_{\mathrm{k}} \\ d_{\mathrm{h}} \\ b_{\mathrm{k}} \\ b_{\mathrm{h}} \end{array}\right]
$$

The desired trajectory used in the experiment was chosen to be a sine wave for each joint with amplitude of 20 degrees but with slightly different frequencies. The hip sine wave was chosen to have 11 cycles and knee chosen to have 10 cycles over a 90 second time interval. This gives a trajectory where the two sine waves begin out of phase, gradually come in phase, and return out of phase after the full 90 second period. A PD control law was implemented for trajectory tracking based on position measurements from the MASs at each joint passed through a first-order low-pass filter with a 25 Hz bandwidth. The proportional and derivative gains for the knee were 60 N·m/rad and 2 N·m·s/rad, respectively, and the proportional and derivative gains for the hip were 30 N·m/rad and 2 N·m·s/rad, respectively.

The trajectory tracking results are illustrated in Figure 3.13 and torques are illustrated in Figure 3.14. Both of these are based on an average of 10 cycles of data. Smoothing splines with a smoothing parameter of 0.9 are fit to hip and knee averaged position data and is then differentiated once and twice to get joint angular velocities and accelerations, respectively. Using the parameter identification theory described in Section 3.5.1.1, the model parameters are identified using Eq. (3.3) and tabulated in Table XIII. Figure 3.14 includes predicted torque in addition to torque measured in experiment. The RMS torque

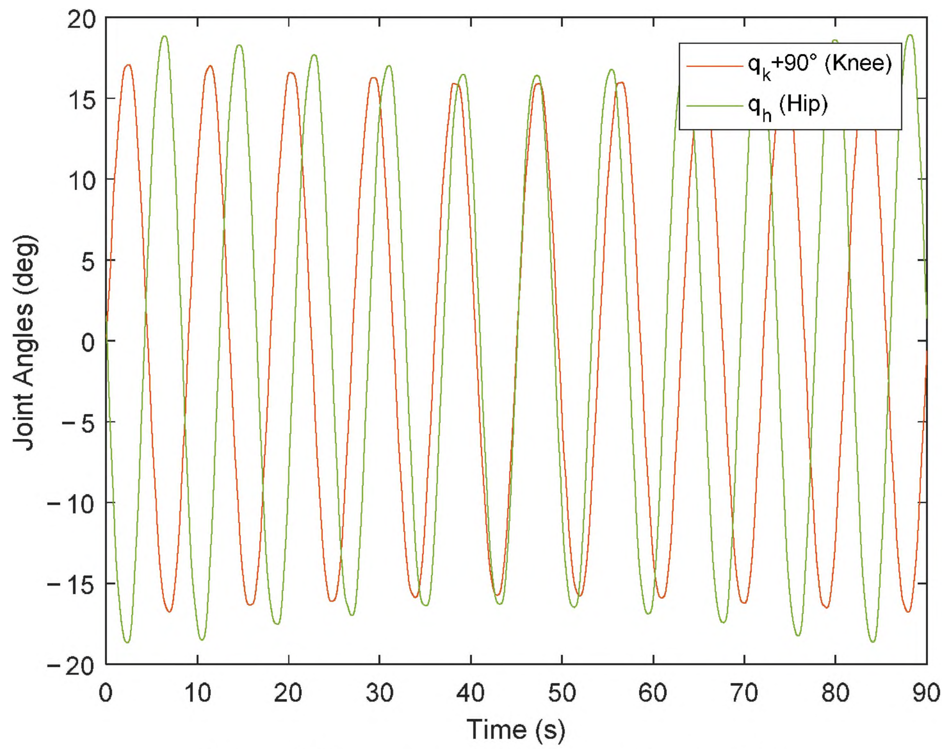

Figure 3.13 Averaged trajectory tracking results

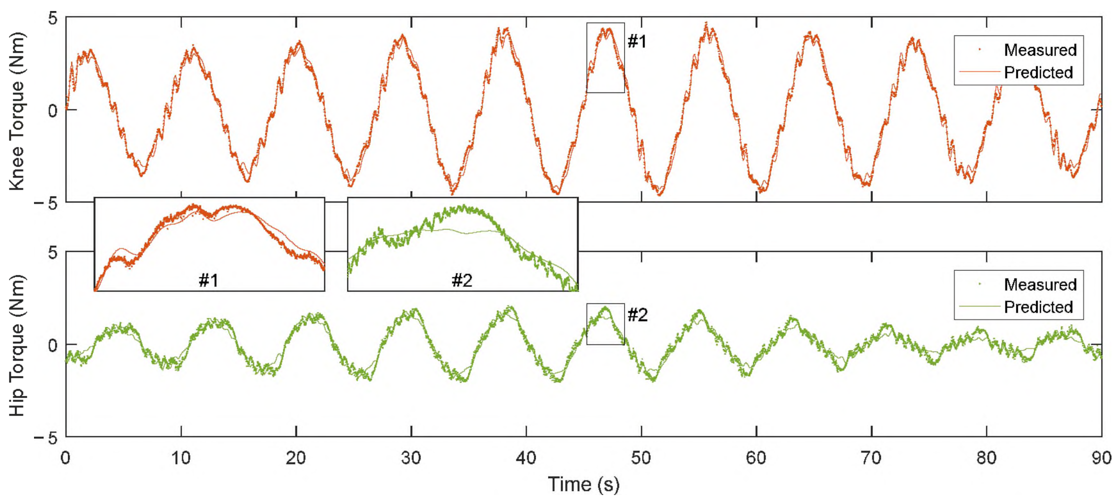

Figure 3.14 Measured and predicted torque for the hip and knee with blow-ups

prediction errors were 0.273 N·m for the knee and 0.285 N·m for the hip. The condition number is 33.1, indicating the identified parameters are robust to measurement noise.

Table XIII. Parameter values in the thigh and torso model

Parameter	Value	Unit
$m_2x_2 + m_3L_2$	1.0488	kg·m
$I_2 + m_2x_2^2 + m_3L_2^2$	1.2219	kg·m^2
m_3x_3	0.2827	kg·m
$I_3 + m_3x_3^2$	0.2923	kg·m^2
d_k	4.2349	N·m·s/rad
d_h	2.8423	N·m·s/rad
b_k	−0.1227	N·m
b_h	−0.02857	N·m

3.5.1.5 Combined Triple Pendulum Model

With the ankle stiffness model, shank model, and thigh and torso model each known, they can be combined into the triple pendulum model. The nominal robot model components of the shank model (3.6), and thigh and torso model (3.7) have many similar parameters when compared to the nominal triple pendulum model (3.4):

$$\boldsymbol{\Phi}_\mathrm{n} = \begin{bmatrix} m_1x_1 + (m_2+m_3)L_1 \\ I_1 + m_1x_1^2 + (m_2+m_3)L_1^2 \\ \hline m_2x_2 + m_3L_2 \\ I_2 + m_2x_2^2 + m_3L_2^2 \\ m_3x_3 \\ I_3 + m_3x_3^2 \end{bmatrix} = \begin{bmatrix} \boldsymbol{\Phi}_\mathrm{sn} \\ \hline \boldsymbol{\Phi}_\mathrm{ttn} \end{bmatrix} + \begin{bmatrix} (m_2+m_3)L_1 \\ (m_2+m_3)L_1^2 \\ \hline 0 \\ 0 \\ 0 \\ 0 \end{bmatrix} \tag{3.8}$$

All of the elements in $\boldsymbol{\Phi}_\mathrm{sn}$ and $\boldsymbol{\Phi}_\mathrm{ttn}$ appear in $\boldsymbol{\Phi}_\mathrm{n}$ but with the addition of two other terms in the first two elements of the vector, namely $(m_2 + m_3)L_1$ and $(m_2 + m_3)L_1^2$. The length of the shank is known as L_1 = 0.300 m, and the mass of the thigh and torso system is directly measured as $m_2 + m_3$ = 4.03 kg. Substituting these into (3.8) and adjusting the placement of the columns of the coefficient matrix and order of the parameters, the complete triple pendulum model is found:

$$\boldsymbol{u} = \boldsymbol{Y}(\boldsymbol{q},\dot{\boldsymbol{q}},\ddot{\boldsymbol{q}})\boldsymbol{\Phi} \tag{3.9}$$

$$\boldsymbol{Y}(\boldsymbol{q},\dot{\boldsymbol{q}},\ddot{\boldsymbol{q}}) = [\boldsymbol{Y}_\mathrm{n} \mid \boldsymbol{Y}_\mathrm{a}] = \left[\begin{array}{c|cc} \boldsymbol{Y}_\mathrm{n} & \boldsymbol{Y}_\mathrm{sa} & 0 \\ & \mathbf{0}_{2\times1} & \boldsymbol{Y}_\mathrm{tta} \end{array}\right]$$

$$\Phi = \begin{bmatrix} \Phi_\mathrm{n} \\ \hline \Phi_\mathrm{a} \end{bmatrix} = \begin{bmatrix} \Phi_\mathrm{n} \\ \hline \Phi_\mathrm{sa} \\ \Phi_\mathrm{tta} \end{bmatrix}$$

$$u_1 = -M_\mathrm{a}(q_1)$$

where, for completeness, all the values of the parameters $\boldsymbol{\Phi}$ are stated in Table XIV.

The dynamic model described by Eq. (3.9) can be rewritten in the form

$$\boldsymbol{u} = \boldsymbol{M}(\boldsymbol{q})\ddot{\boldsymbol{q}} + \boldsymbol{H}(\boldsymbol{q},\dot{\boldsymbol{q}}) + \boldsymbol{G}(\boldsymbol{q}) \tag{3.10}$$

where $\boldsymbol{M}$ is the inertia matrix, $\boldsymbol{G}$ is the gravity torque vector, and $\boldsymbol{H}$ is a torque vector that accounts for centrifugal effects, Coriolis effects, and other terms not part of the nominal robot model (excluding the ankle stiffness model). These can be found using:

$$\boldsymbol{M}(\boldsymbol{q}) = \frac{\partial\left(\boldsymbol{Y}(\boldsymbol{q},\dot{\boldsymbol{q}},\ddot{\boldsymbol{q}})\Phi\right)}{\partial\ddot{\boldsymbol{q}}}, \quad \boldsymbol{G}(\boldsymbol{q}) = \frac{\partial\left(\boldsymbol{Y}(\boldsymbol{q},\dot{\boldsymbol{q}},\ddot{\boldsymbol{q}})\Phi\right)}{\partial g}g$$

$$\boldsymbol{H}(\boldsymbol{q},\dot{\boldsymbol{q}}) = \boldsymbol{Y}(\boldsymbol{q},\dot{\boldsymbol{q}},\ddot{\boldsymbol{q}})\Phi - \boldsymbol{M}(\boldsymbol{q})\ddot{\boldsymbol{q}} - \boldsymbol{G}(\boldsymbol{q}).$$

Table XIV. Parameter values in the triple pendulum model

Parameter	Value	Unit
$\Phi_1 = m_1x_1 + (m_2 + m_3)L_1$	1.2132	kg·m
$\Phi_2 = I_1 + m_1x_1^2 + (m_2 + m_3)L_1^2$	0.3672	kg·m^2
$\Phi_3 = m_2x_2 + m_3L_2$	1.0488	kg·m
$\Phi_4 = I_2 + m_2x_2^2 + m_3L_2^2$	1.2219	kg·m^2
$\Phi_5 = m_3x_3$	0.2827	kg·m
$\Phi_6 = I_3 + m_3x_3^2$	0.2923	kg·m^2
$\Phi_7 = d_\mathrm{ap}$	0.0176	N·m·s/rad
$\Phi_8 = d_\mathrm{ad}$	0.0266	N·m·s/rad
$\Phi_9 = d_\mathrm{k}$	4.2349	N·m·s/rad
$\Phi_{10} = d_\mathrm{h}$	2.8423	N·m·s/rad
$\Phi_{11} = b_\mathrm{k}$	−0.1227	N·m
$\Phi_{12} = b_\mathrm{h}$	−0.02857	N·m

3.5.2 Simulation and Analysis Requisites

For simulation and analysis purposes, the robot model (3.10) is rewritten in nonlinear state-space representation with the states $\boldsymbol{z} = [\boldsymbol{q}^{\mathrm{T}} \quad \dot{\boldsymbol{q}}^{\mathrm{T}}]^{\mathrm{T}}$ as follows:

$$\boldsymbol{G}: \begin{cases} \dot{\boldsymbol{z}} = \boldsymbol{f}(\boldsymbol{z}) + \boldsymbol{g}(\boldsymbol{z})\boldsymbol{u} \\ \boldsymbol{y} = \boldsymbol{z} \end{cases}$$

$$\boldsymbol{f}(\boldsymbol{z}) = \begin{bmatrix} z_4 \\ z_5 \\ z_6 \\ -\boldsymbol{M}^{-1}(\boldsymbol{z})\left(\boldsymbol{H}(\boldsymbol{z}) + \boldsymbol{G}(\boldsymbol{z})\right) \end{bmatrix}, \quad \boldsymbol{g}(\boldsymbol{z}) = \begin{bmatrix} \mathbf{0}_{3\times3} \\ \boldsymbol{M}^{-1}(\boldsymbol{z}) \end{bmatrix}$$

The input $\boldsymbol{u}$ to the system $\boldsymbol{G}$ is the vector of torques supplied to the joints and the output $\boldsymbol{y}$ is the vector of the system states containing joint positions and velocities. The ankle is not directly controlled, and is equal to the ankle stiffness model, so $u_1 = -M_{\mathrm{a}}(q_1)$. For the purpose of having the equilibrium point in the upright position $\boldsymbol{q}^{\mathrm{d}} = [\pi/2 \quad 0 \quad 0]^{\mathrm{T}}$ in simulation, the input to the ankle stiffness model was offset such that $M_{\mathrm{a}}(\pi/2) = 0$. The other two inputs to the system are directly controlled using a feedback controller of choice, here chosen to be a memoryless control law $[u_2 \quad u_3]^{\mathrm{T}} = \boldsymbol{K}(\boldsymbol{q}, \dot{\boldsymbol{q}})$ which algebraically relates its outputs to its inputs without having any internal states. A block diagram for this system is shown in Figure 3.15.

The control law does not directly impact the value of u_1. Accordingly, the ankle stiffness model is effectively part of the plant as far as the controller is concerned. By closing the upper-loop by substituting $u_1 = -M_{\mathrm{a}}(q_1)$ as the first input to model $\boldsymbol{G}$, a modified system $\boldsymbol{G}'$ is found as

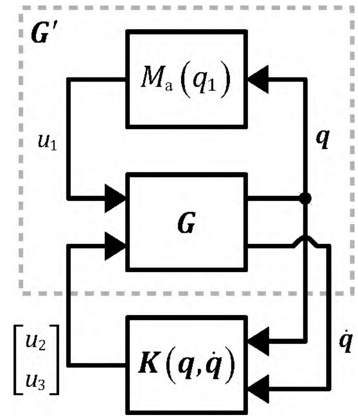

Figure 3.15 Block diagram for controlling the triple pendulum system

$$G': \begin{cases} \dot{\boldsymbol{z}} = \boldsymbol{f}'(\boldsymbol{z}) + \boldsymbol{g}'(\boldsymbol{z}) \begin{bmatrix} u_2 \\ u_3 \end{bmatrix}. \\ \boldsymbol{y} = \boldsymbol{z} \end{cases} \tag{3.11}$$

This modified system is used for controller synthesis in the next section.

3.5.3 Controller Synthesis

The controller gains of the MBC and LQR should to be selected based on some criteria. In the work of Azad and Featherstone [81], which is the basis for the MBC, the authors linearized their closed-loop system and found the control gains that exactly placed the closed-loop poles at a desired location. However, this exact pole placement was not possible in the later-described MBC in Section 3.5.6 due to the higher dimensionality from the increased number of control gains for the triple pendulum. Instead of exact pole placement, this section presents an approximate pole placement through numerical optimization.

The optimization problem constructed to find controller gains based on a few criteria. First, the system response should not be too slow. Second, the closed-loop system should be sufficiently damped to avoid large oscillatory behavior. Third, the controller gains should not have too fast as a response as to require large controller magnitudes and actuator torques while ensuring closed-loop stability.

For a given controller $\boldsymbol{K}(\boldsymbol{q}, \dot{\boldsymbol{q}})$, the closed-loop system can be found by substituting the control law into the system $\boldsymbol{G}'$ in (3.11) in Figure 3.15. A local analysis is performed by linearizing the closed-loop system about the equilibrium point and finding the possibly complex eigenvalues λ_k of the state matrix $\boldsymbol{A}''$ as a function of the controller gains.

$$\boldsymbol{G}'': \quad \begin{cases} \dot{\boldsymbol{z}} = \boldsymbol{f}''(\boldsymbol{z}) \approx \boldsymbol{A}''\left(\boldsymbol{z} - \boldsymbol{z}^{\mathrm{d}}\right) \\ \boldsymbol{y} = \boldsymbol{z} \end{cases}$$

$$\boldsymbol{A}'' = \left.\frac{\partial \boldsymbol{f}''}{\partial \boldsymbol{z}}\right|_{\boldsymbol{z}=\boldsymbol{z}^{\mathrm{d}}}, \quad \lambda_k = r_k + i_k i$$

These eigenvalues are used in the objective function to be minimized, which is composed of three terms for the three criteria:

$$J = w_{\mathrm{R}} \max_{k=1\ldots6} \left| r_k^{-1} \right| + w_{\mathrm{I}} \sum_{k=1}^{6} \left| i_k \right| + P \tag{3.12}$$

The first term corresponds to the first criterion, ensuring the system response is not too small. This is accomplished by keeping the eigenvalues far from the imaginary axis. The second term corresponds to the second criterion, bringing the eigenvalues close to the real axis to increase damping effects. The coefficients w_{R} and w_{I} are weights to be manually tuned. The third term corresponds to the third criterion and is a penalty term

$$\begin{aligned} P = {} & 10^9 \sum_{k=1}^{6} \langle R_k > 0 \rangle \left(1 + R_k\right) + \\ & 10^6 \sum_{j=1}^{2} \sum_{k=1}^{3} \langle P_{jk} > 100 \rangle \left(1 + P_{jk}/100\right) + \\ & 10^6 \sum_{j=1}^{2} \sum_{k=1}^{3} \langle D_{jk} > 10 \rangle \left(1 + D_{jk}/10\right) \end{aligned}$$

where P_{jk} and D_{jk} correspond to the components of the block elements of the linearized controller for the position term $\boldsymbol{P}$ and velocity term $\boldsymbol{D}$, respectively.

$$\boldsymbol{P} = \left.\frac{\partial \boldsymbol{K}(\boldsymbol{q},\dot{\boldsymbol{q}})}{\partial \boldsymbol{q}}\right|_{\substack{\boldsymbol{q}=\boldsymbol{q}_0 \\ \dot{\boldsymbol{q}}=\boldsymbol{0}}}, \quad \boldsymbol{D} = \left.\frac{\partial \boldsymbol{K}(\boldsymbol{q},\dot{\boldsymbol{q}})}{\partial \dot{\boldsymbol{q}}}\right|_{\substack{\boldsymbol{q}=\boldsymbol{q}_0 \\ \dot{\boldsymbol{q}}=\boldsymbol{0}}}$$

The first term in P heavily penalizes unstable systems which occur when there are positive real components of the eigenvalues r_k. The second and third terms penalize large gains in the controller, which will limit how quickly the system can respond and also control torques.

3.5.4 Simulations of Crouch-to-Stand Motion

In the forthcoming simulations, the initial conditions were chosen such that the system is in a balanced upright configuration without any velocity. This happens when the CoM of the system C is aligned above the ankle.

$$\begin{aligned} C &= \frac{\begin{bmatrix} c_1 & 0 & c_{12} & 0 & c_{123} & 0 \end{bmatrix} \boldsymbol{\Phi}_{\mathrm{n}}}{m_1 + m_2 + m_3} = 0 \\ \Rightarrow \quad & c_1 \Phi_1 + c_{12} \Phi_3 + c_{123} \Phi_5 = 0 \end{aligned} \tag{3.13}$$

Setting the initial configuration such that the constraint (3.13) is true leaves two algebraic degrees of freedom open. That is, given any two joint angles, the third can be calculated. Joint velocities were chosen to be zero for the initial conditions in the upcoming simulations.

3.5.5 LQR Control Synthesis and Simulation

A linear-quadratic regulator (LQR) is an optimal controller to regulate the system to a desired setpoint for a given linear plant. The modified system $\boldsymbol{G}'$ from Section 3.5.2 is linearized about the equilibrium point $\boldsymbol{z}^{\mathrm{d}} = \begin{bmatrix}\boldsymbol{q}^{\mathrm{d}\,\mathrm{T}} & \boldsymbol{0}_{1\times 3}\end{bmatrix}^{\mathrm{T}}$, giving a linear time-invariant approximation of the model near the equilibrium point:

$$\boldsymbol{G}': \begin{cases} \dot{\boldsymbol{z}} \approx \boldsymbol{A}'\left(\boldsymbol{z}-\boldsymbol{z}^{\mathrm{d}}\right)+\boldsymbol{B}'\begin{bmatrix} u_2 \\ u_3 \end{bmatrix} \\ \boldsymbol{y}=\boldsymbol{z} \end{cases}$$

where

$$\boldsymbol{A}' = \left.\frac{\partial \boldsymbol{f}'}{\partial \boldsymbol{z}}\right|_{\boldsymbol{z}=\boldsymbol{z}^{\mathrm{d}}}, \quad \boldsymbol{B}' = \boldsymbol{g}'\left(\boldsymbol{z}^{\mathrm{d}}\right).$$

An LQR controller takes the form

$$\begin{bmatrix} u_2 \\ u_3 \end{bmatrix} = \boldsymbol{K}\left(\boldsymbol{q},\dot{\boldsymbol{q}}\right) = -\boldsymbol{P}\left(\boldsymbol{q}-\boldsymbol{q}^{\mathrm{d}}\right)-\boldsymbol{D}\dot{\boldsymbol{q}}$$

where the controller gains $\boldsymbol{P}$ and $\boldsymbol{D}$ are found by minimizing the cost function

$$J_{\mathrm{LQR}} = \int_0^{\infty}\left(\boldsymbol{z}^{\mathrm{T}}\boldsymbol{Q}\boldsymbol{z}+\boldsymbol{u}^{\mathrm{T}}\boldsymbol{R}\boldsymbol{u}\right)dt$$

for the given plant and where the weight matrices $\boldsymbol{Q}$ and $\boldsymbol{R}$ should be chosen to be positive definite. The decision variables in the optimization from Section 3.5.3 are the elements of the matrices $\boldsymbol{Q}$ and $\boldsymbol{R}$, up to symmetry. The weights $\boldsymbol{Q}$ and $\boldsymbol{R}$, with 24 total elements to be chosen, were essentially replaced with new weights w_{R} and w_{I}, with merely 2 parameters to tune. This simplified the weight selection process drastically. This choice also allowed the controllers to be synthesized using identical cost function, thereby allowing the two controllers more directly comparable. The objective function (3.12) is augmented with an additional penalty term to constrain the definiteness of these matrices, applying an additional penalty when any of the eigenvalues of $\boldsymbol{Q}$ and $\boldsymbol{R}$ are non-positive. The optimization weights were manually tuned as $w_{\mathrm{R}} = 10$ and $w_{\mathrm{I}} = 1$ to give satisfactory results, and were tuned concurrently in the later-described optimization for the MBC in Section 3.5.6.

The LQR synthesis problem is accomplished using the `lqr` function in Matlab from the Control System Toolbox. This function gives the optimal feedback controller by minimizing the cost function J_{LQR}, which can be formulated as an equivalent problem of solving the Riccati equation. This is effectively a nested optimization problem, with the high-level optimization being performed to minimize J numerically in (3.12) by varying the controller gains and the low-level optimization being used to minimize J_{LQR} through solving the Riccati equation. The resulting controller gains that gave the smallest objective function value J follows:

$$\boldsymbol{P} = \begin{bmatrix} 51 & 39 & 20 \\ -20 & -12 & 19 \end{bmatrix}, \quad \boldsymbol{D} = \begin{bmatrix} 10 & 8.2 & 4.6 \\ -6.2 & -1.2 & 2.2 \end{bmatrix}.$$

This controller is then applied to balance the triple pendulum system starting at the initial configuration $\boldsymbol{q}(t = 0) = [94 \quad -23.64 \quad 54]^{\text{T}}$ deg with no initial velocity. In this configuration, the system satisfies (3.13) so the center of mass of the system is directly above the ankle joint. The resulting response to this system is presented in Figure 3.17 with snapshots in Figure 3.16.

3.5.6 Momentum-Based Balance Control Synthesis and Simulation

The momentum-based balance controller (MBC) described in this section is based on the work of Azad and Featherstone [81]. In their paper, the authors state how an equivalent condition for static balance of the double pendulum, where the center of mass of the system is at the zero position with zero joint velocity, can be stated in terms of

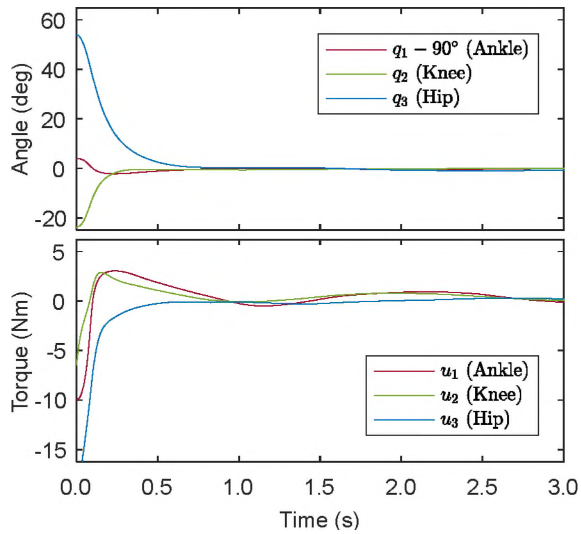

Figure 3.17 Balancing simulation results of the triple pendulum using a LQR

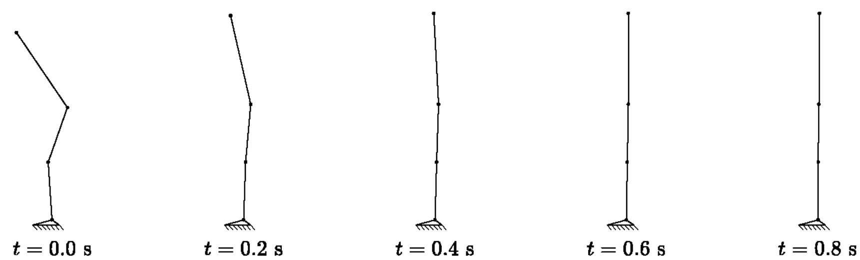

Figure 3.16 Snapshots of the balancing simulation of the triple pendulum using a LQR

angular momentum and its derivatives. Specifically, the angular momentum L, its first time-derivative $\dot{L}$, and second time-derivative $\ddot{L}$ of the system in the base frame are all zero. Motivated to drive angular momentum and its derivatives to zero, the authors design the structure of the control law to be a linear combination of L, $\dot{L}$, and $\ddot{L}$ which controls the second, topmost joint in the double pendulum with the first joint uncontrolled. They also include a term for gravity compensation at the desired configuration and a term proportional to the joint angles to balance the system in other configurations and improve performance.

A similar approach is taken here for the triple pendulum, where the knee and hip joints of the triple pendulum are each controlled as a linear combination of the angular momentum and its first and second derivative of the system plus gravity compensation and proportional terms. Gravity compensation is used at the current configuration rather than the desired configuration since there would be no impact of gravity compensation at the desired upright configuration and was kept in the control law to improve performance. The control law follows as

$$\begin{bmatrix} u_2 \\ u_3 \end{bmatrix} = \boldsymbol{K}(\boldsymbol{q},\dot{\boldsymbol{q}}) = \boldsymbol{K}_{\mathrm{MBC}} \begin{bmatrix} L \\ \dot{L} \\ \ddot{L} \end{bmatrix} + \begin{bmatrix} k_{\mathrm{h}} & 0 & 0 \\ 0 & k_{\mathrm{k}} & 0 \end{bmatrix} (\boldsymbol{q} - \boldsymbol{q}_0) + \begin{bmatrix} G_2(\boldsymbol{q}) \\ G_3(\boldsymbol{q}) \end{bmatrix} \tag{3.14}$$

where $\boldsymbol{K}_{\mathrm{MBC}}$, k_{h}, and k_{k} are controller gains to be chosen.

The angular momentum L is found by adding the contribution of each link due to the linear motion of the center of mass, which respectively has position and velocity vectors $\boldsymbol{C}_k$ and $\dot{\boldsymbol{C}}_k$ in the base frame, and angular motion of the links. It turns out that the angular momentum at the base frame in the direction normal to the plane in which the pendulum lies $\hat{\boldsymbol{z}}$ is linear in the inertial parameters and is determined by inspection as:

$$\begin{aligned} L &= \sum_{k=1}^{3} m_k \left(\boldsymbol{C}_k \times \dot{\boldsymbol{C}}_k\right) \cdot \hat{\boldsymbol{z}} + I_k \omega_k \\ &= \begin{bmatrix} 0 & \omega_1 & c_2 L_1(\omega_1+\omega_2) & \omega_2 & c_{23} L_1(\omega_1+\omega_3) + c_3 L_2(\omega_2+\omega_3) & \omega_3 \end{bmatrix} \boldsymbol{\Phi}_{\mathrm{n}} \end{aligned} \tag{3.15}$$

By Euler's second law of motion in rigid body dynamics, the first time-derivative of the angular momentum $\dot{L}$ is equal to the net external moment acting on the system, which for this system is just gravitational effects. The second time-derivative of the angular momentum $\ddot{L}$ can be obtained by simple differentiation with respect to time. Each of these are written as a linear combination of the inertial parameters by inspection.

$$\dot{L} = -g\sum_{k=1}^{3} m_k \boldsymbol{C}_k \cdot \hat{\boldsymbol{x}} = \begin{bmatrix} -c_1 g & 0 & -c_{12} g & 0 & -c_{123} g & 0 \end{bmatrix} \boldsymbol{\Phi}_{\mathrm{n}} \tag{3.16}$$

$$\ddot{L} = -g\sum_{k=1}^{3} m_k \dot{\boldsymbol{C}}_k \cdot \hat{\boldsymbol{x}} = \begin{bmatrix} \omega_1 s_1 g & 0 & \omega_2 s_{12} g & 0 & \omega_3 s_{123} g & 0 \end{bmatrix} \boldsymbol{\Phi}_{\mathrm{n}} \tag{3.17}$$

Substituting (3.15), (3.16), and (3.17) into (3.14) symbolically in terms of controller gains and substituting the result into (3.11) closes the lower-loop of the system. This is used in in controller synthesis. A set of 100 controller gains that have stable closed-loop eigenvalues were randomly generated. These were used as initial conditions for solving the unconstrained optimization problem in parallel using a quasi-Newton nonlinear numerical optimizer. The weights in the cost function were tuned as the same values of $w_{\mathrm{R}} = 10$ and $w_{\mathrm{I}} = 1$ to give a control law that gave satisfactory performance. This process of choosing weights took some iteration to obtain reasonable results, without a clear pattern emerging on the effect from the weights. As such, they were chosen nearly arbitrarily, and were tuned concurrently in the previously described optimization for the LQR in Section 3.5.5. The weights were chosen to be identical to what was done with LQR, which allows the controllers to be comparable by being synthesized using the same cost function. The resulting controller gains that gave the smallest objective function value follows:

$$\boldsymbol{K}_{\mathrm{MBC}} = \begin{bmatrix} -25.8 & -0.38 & 1.9 \\ -13.2 & 0.0 & 1.1 \end{bmatrix},\ k_{\mathrm{h}} = 2.8,\ k_{\mathrm{k}} = 19.4.$$

For reference and comparison, the linearized controller gains are:

$$\boldsymbol{P} = \begin{bmatrix} 58 & 51 & 16 \\ 11 & -8.1 & 11 \end{bmatrix},\ \boldsymbol{D} = \begin{bmatrix} 5.0 & 6.1 & 5.1 \\ -8.9 & -3.4 & 0.58 \end{bmatrix}$$

Similar to before, this control law is applied to balance the triple pendulum system in simulation with the same initial static configuration as was used in the simulation using a LQR, specifically $\boldsymbol{q}(t=0) = [94 \quad -23.64 \quad 54]^{\mathrm{T}}$ deg. The simulation results are presented in Figure 3.19 which includes the linearized MBC response. Snapshots are shown in Figure 3.18.

3.6 Region of Viability

To evaluate the robustness of the MBC to initial conditions, similar simulations were performed as done in the Section 3.5.4 but for a range of statically balanced initial conditions. The simulation can be considered a failure when an undesired event happens. A failure occurs when the knee hyperextends by at least 2 deg, which is close to average

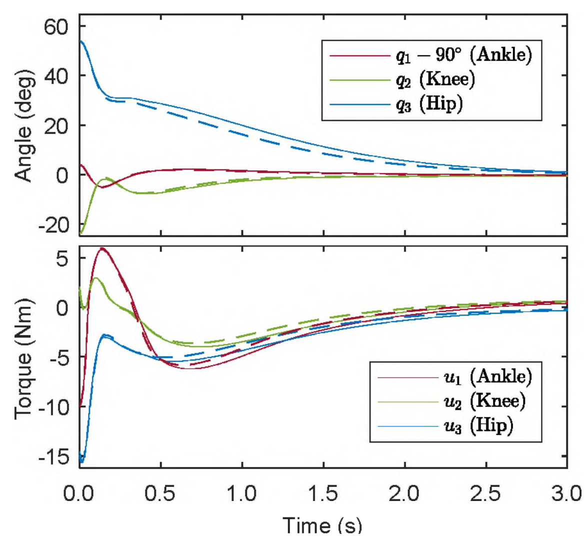

Figure 3.19 Balancing simulation results of the triple pendulum using a MBC (solid) and its linearization (dashed)

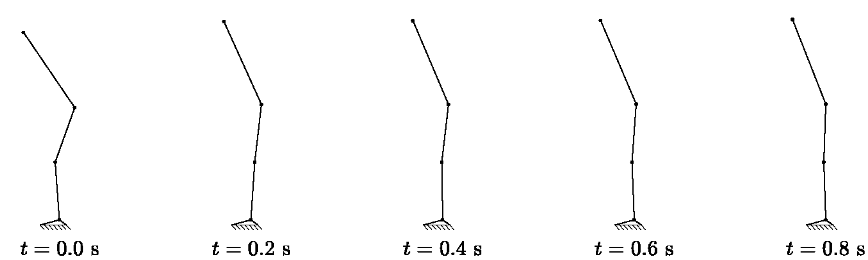

Figure 3.18 Snapshots of the balancing simulation of the triple pendulum using a MBC

in healthy adults [87]. The maximum torque observed in the simulation is quantified to better understand the limits of the controller gains and capabilities.

$$u_{\max} = \max_{i \in \{2,3\},\, t} u_i(t)$$

This set of simulations is used to display a region of viability, which shows for which initial conditions a failure occurs from knee hyperextension, and shows the maximum torque recorded for the set of simulations. The region of viability for the LQR is shown in Figure 3.20 and for the MBC is shown in Figure 3.22. These simulations use the same controllers synthesized previously.

3.7 Experimental Results

In addition to simulations, the standing balance controllers, namely the LQR and MBC, are validated in hardware in the system shown in Figure 3.21. However, the configuration of the system is such that both legs are included but the controllers only consider a single leg. As such, a controller is implemented for each leg separately. In

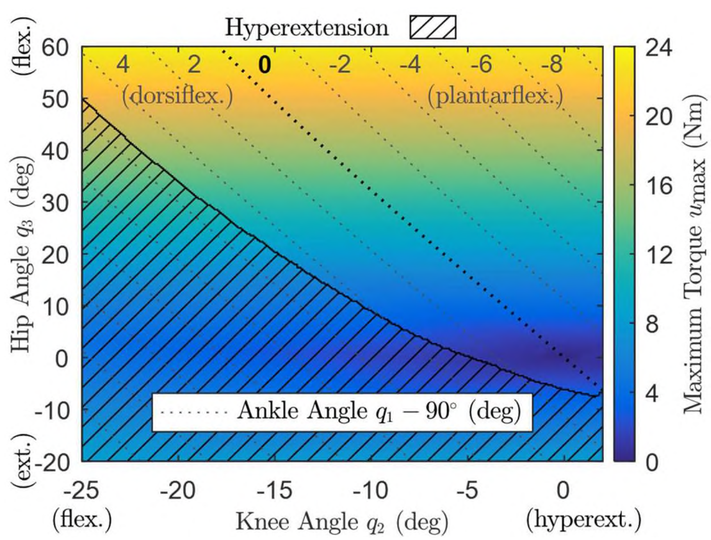

Figure 3.20 Region of viability with maximum actuator torque of the triple pendulum using a LQR

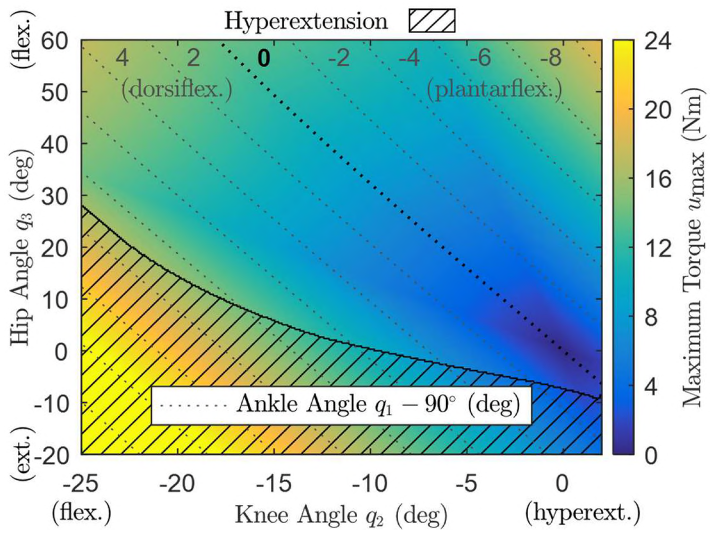

Figure 3.22 Region of viability with maximum actuator torque of the triple pendulum using a MBC

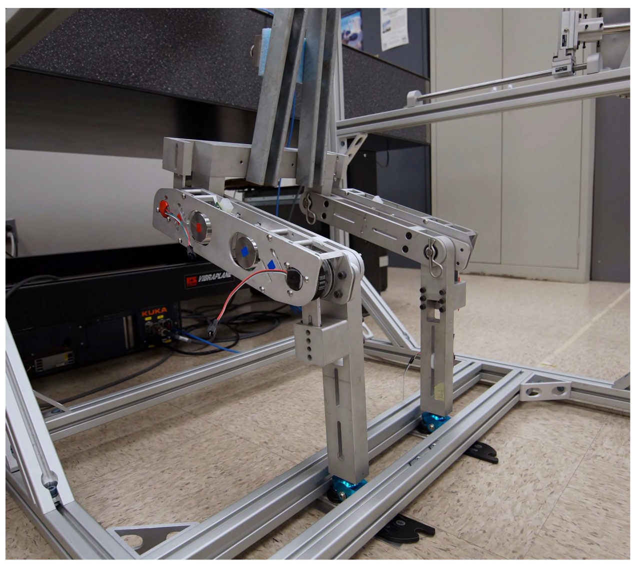

Figure 3.21 Experimental set up for running the standing balance controllers

addition, only one IMU is used to measure the position and velocity of the ankle degree of freedom of one leg; the other ankle is assumed behave similarly with equal values. For testing purposes, the foot of each leg is clamped to the ground to keep the system from toppling. The system is initially configured in a crouched position with no motion.

During conducted experiments, the system exhibited noisy, high frequency phenomena primarily at the motors at roughly 43 Hz. This is due to poor controllability of the motors when operating at low speeds. When one motor would start chattering, the other motors would sometimes begin chattering as well and result in large motion of the entire system which could destabilize the system. This resulted in high velocities, making the controllers impractical for direct implementation in the system. This issue is exacerbated with higher gains, particularly for the derivative term, and were a determining factor in choosing the thresholds in the controller gain penalties in (3.12). To mitigate the issue, control signal amplitude was scaled down by a factor when joint acceleration exceeded a threshold in absolute value for a brief period of time. In addition, friction material was manually added to the system at the motors to reduce the likelihood of chatter and reduce chatter amplitude, though left unmodeled. The implementations of the control laws were possible due to these provisions.

The two controllers synthesized in Sections 3.5.5 and 3.5.6 were applied to balance the triple pendulum system. The system response for the LQR controller is shown in Figure 3.23 and the MBC is shown in Figure 3.24, both starting in approximately the same configuration. Both controllers successfully brought the system to an upright configuration. Steady-state was reached after 2.9 s for the LQR and 1.7 s for the MBC, settling at 1.9 deg for the LQR and 5.8 deg for the MBC at the hip, with smaller values for the ankle and knee. Since both controllers are memoryless so do not have any integrating action, a non-zero steady-state error is reached due to the uncompensated Coulomb friction. The largest recorded torque happened around the start which was 45.6 Nm for the LQR and 59.4 Nm for the MBC at the hip, with smaller values for the knee. These values are larger than those reported in the region of viability due to the initial conditions of the experiments being outside this region.

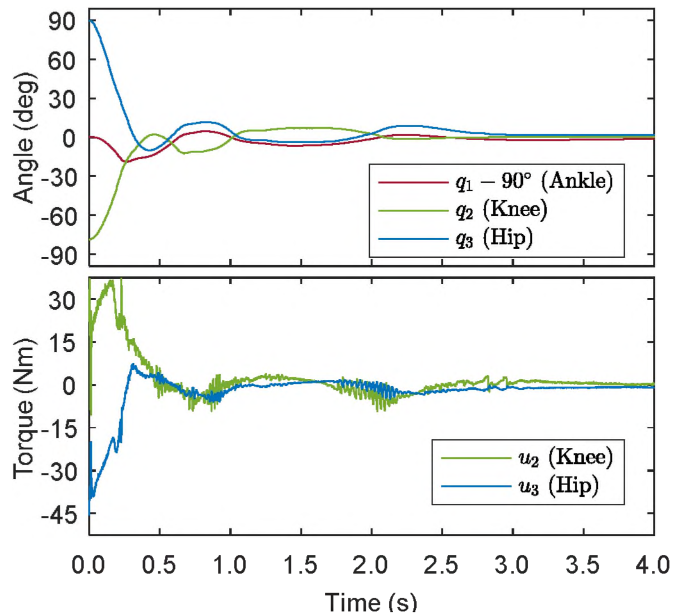

Figure 3.23 Experimental results for the triple pendulum using a LQR

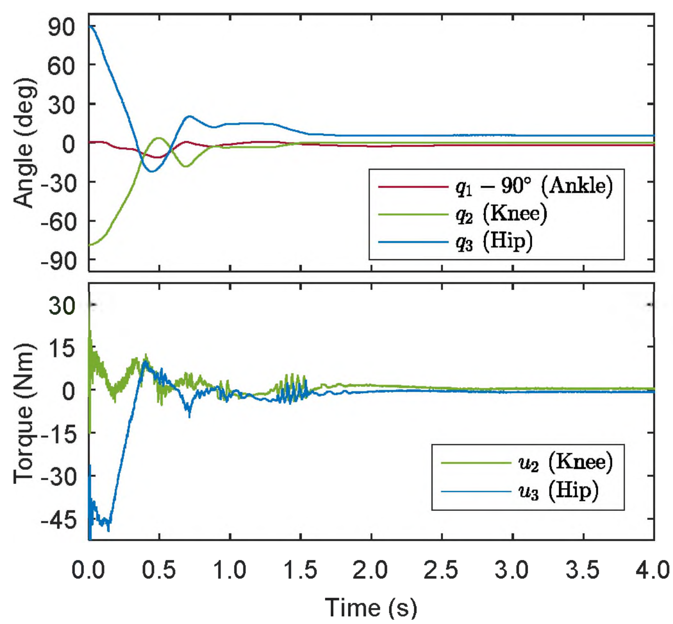

Figure 3.24 Experimental results for the triple pendulum using a MBC

3.8 Discussion and Conclusions

In simulation, both the LQR and MBC were able to stabilize the system about the equilibrium point and balance the system for a given initial static configuration. The LQR had a quicker settling time than the MBC, taking only 0.5 s using LQR rather than the

2.7 s for MBC to reach 2 deg of the upright configuration. However, this required a peak torque of 21.3 Nm, larger than the 15.5 Nm reached by the MBC. This peak torque occurred at the hip joint near the initial condition. It proved difficult to synthesize an MBC using the optimization process discussed in Section 3.5.3, much more so than LQR. In conclusion, an LQR control strategy will likely be easier to synthesize than an MBC while possibly also giving a faster response but perhaps at the cost of higher torque. However, tuning of the optimization or application in other systems may change this. The linearized MBC seemed to behave similarly to the nonlinear MBC, suggesting that a linear memoryless state-feedback control strategy has the potential for similar performance than the nonlinear version. The nonlinearity may add unnecessary extra complexity without much benefit. It is for these reasons that a linear memoryless state-feedback control law such as an LQR is a better choice since similar performance can be achieved. However, many poor performing controllers were encountered, particularly for the MBC, due to numerous local minima in the optimization problem. The best performing controllers for MBC and LQR were hand-picked. There may be some better performing MBC that were not encountered.

In the regions of viability, both controllers were fairly robust to the starting configuration. Specifically, neither controller destabilized the system for any of the initial configurations, which was determined if any joint exceeded 95 deg from the upright configuration. However, there were knee hyperextension issues with both control strategies with about 30% of the MBC and 44% of the LQR starting configurations resulting in hyperextension. This primarily occurred at the bottom of the plots where hip was initially straight or extended and the knee was initially flexed. However, MBC may be better than LQR at the top left of the plots where the knee begins flexed. This suggests that, for the considered system, the MBC may improve upon the region of viability compared to the LQR. However, tuning of knee damping may change this which is likely the primary determining factor of knee hyperextension. When considering initial conditions in the region of viability, the MBC had less peak torque than LQR, which agrees with the previous simulations for a particular initial condition. It appears as though the MBC peak torque is a function of both initial hip and knee joint angles whereas LQR is only a function of primarily hip angle. The peak torques are reasonable as compared to the actuator capabilities described in Section 3.3. The LQR reached 23 Nm and the MBC reached 19 Nm, whereas the actuator capabilities were tested up to a peak short-duration torque of 17.2 Nm, which was tested for a duration about 1 s. The actuators simulation values occurred at the initial condition and lasted less than 0.1 s; the actuators would likely handle these larger torques without issue.

Although the controllers successfully stabilized the systems in simulations, the controllers seemed to be reliant on the ankle stiffness to balance the system. Controllers synthesized based on a plant $\boldsymbol{G'}$ with little or zero ankle stiffness (not shown in this document) had difficulties creating closed-loop systems robust to initial conditions; the closed-loop systems seemed to have very small regions of attraction in these cases. This suggests that, at least for the system used here and the kinds of controllers considered here, the ankle torque plays a crucial role in balancing and stabilizing a system. In addition, the controllers do not account for the limited range of motion of the joints, particularly for hyperextension at the knee. Simulations using other initial conditions could result in undesired hyperextension at the knee.

In experiments, the controllers also were able to bring the system to an upright configuration. This validates the feasibility of implementation of such controllers in powered orthotic systems. However, the experimental results seem to not closely resemble simulation results. The initial condition in experiment differed from the simulations and Coulomb friction is likely underestimated. Bringing the initial condition of the simulation to match that of the experiment and increasing the friction levels resulted in similar performing LQR simulations results but destabilized the MBC system in simulation. An experiment (unreported) using an initial condition in a balanced configuration from the simulation, which is within the region of viability, resulted in oscillations upwards of a 30 deg magnitude at the hip for MBC. This indicates that the model has a poor resemblance of the true system and suggests the simulations may not accurately predict system behavior. Even though the controllers did drive the system to a balanced, upright configuration in simulation and experiments reported here, the generalizability of these results may be in question.

The work presented in this section did not directly consider knee hyperextension or loss of balance. These factors were only considered after controller synthesis through manual observations of the simulations. These can be directly considered in the control synthesis process through a brute-force approach by running a set of simulations for each iteration of the optimization problem. The set of simulations should be representative of the expected operational space. Each simulation can monitor the ZMP to ensure it remains in the support region of the system to maintain balance at all points in time. In addition, each simulation can monitor the ankle angle to ensure it does not hyperextend. If either of these are not satisfied for any of the simulations, an additional penalty can be added to the objective function. The main drawback of this approach is that it would be computationally expensive, and perhaps making the control synthesis problem even more difficult for MBC than it currently is. Note that if a brute-force approach is taken, the LQR cost function J_{LQR} could be considered directly at this stage in the many simulations without the need of a linearized model, similar to the optimization as done in [88]. Alternative to running many simulations, a heuristic or indirect approach can be taken. By adjusting the cost function to keep knee damping high, knee hyperextension would be less likely to occur. In addition, tighter bounding of the control gains would likely result in the ZMP not deviating as far from the origin, improving the likelihood it will not exit the support region. The control law could also be modified to include additional nonlinear stiffness or damping at the knee which specifically addresses the knee hyperextension issue, having an increased effect near the fully extended configuration. It may be possible to formulate a theoretical framework for ZMP which can consider balance in the synthesis process without a brute force approach or based on heuristics, however the nonlinearity of the computed ZMP, controller, and system makes this a difficult problem to investigate.

CHAPTER IV

ASSISTIVE CONTROL OF THE PROTOTYPE ANTHROPOMETRICALLY PARAMETRIZED ORTHOSIS

One of the primary long-term goals for the powered lower-limb orthosis in this dissertation is for use as an assistive device. This chapter presents the first human trial evaluating the anthropometrically parametrized orthosis from Section 2.3 for assistance. First, background information is briefly covered on powered assistive orthoses for healthy subjects and how this is quantified throughout the literature. Second, the methods for the experiment are discussed, including recruitment, experimental protocol, and how the data was processed and analyzed. Finally, the experimental results are shown and discussed. The contents of this chapter are based on the results submitted for publication in [89].

4.1 Background on Assistive Devices

A powered lower-limb orthosis for assistance is designed for making some task such as walking easier to perform. Various control strategies have been used to accomplished this for healthy subjects, primarily for walking. Myoelectric-based control strategies are a common theme, particularly for powered AFOs, where control signals are typically proportional to EMG measurements [90]–[92]. Scaled user torque can also be taken as the control approach, which can be estimated from EMG measurements through a neuromusculoskeletal model [93] or from known torque patterns in healthy walking for a feed-forward control approach [94]. A bang-bang controller, enabled via a foot-switch, can also be used [90]. Approaches akin to inverse dynamics can also be applied, such as partial inertia compensation [95] or gravity compensation [96]. Trajectory tracking controllers have also been applied, such as one with time-varying cyclic reference [97]. These control strategies have all been used in assistive applications for a variety of types of exoskeletons.

It is important to quantify the degree of user effort when evaluating the assistive capability of a powered orthotic device. However, to understand if a control strategy is able to help a subject perform a task, user effort when using the device must be compared to another case. Typically, user effort is compared to when the subject is using the orthosis in an unpowered state or when the subject is not wearing the orthosis. A decrease of user effort from either of these condition (unpowered or no orthosis) to the condition with the orthosis powered and controlled can show the device can make performing a task easier. Metabolic cost is a gold standard in such comparisons and has been used throughout the literature [91], [96], [97]. Metabolic cost has even been suggested to be the main goal in the design and evaluation of powered orthotic devices in [98]. However, other measures have been used. Muscle activation is another very common measure used for comparison [90], [91], [94], [96], [97]. Other less common measures include user torque [93], [99], mechanical power or energy of the joint [91], [99], and heart rate [96].

4.2 Methods

4.2.1 Participant Recruitment

As discussed in Section 2.3, the anthropometrically parametrized orthosis has been developed for a particular adult subject. The individual agreed to partake in the study after being informed about the purpose of the study and the risks involved with participating in the study. The subject provided informed written consent, as mandated by the Cleveland State University institutional review board. At the time of participation, the male volunteer was 29 years of age, weighed 78.0 kg, and was 178 cm tall. The experimental study took place at the Human Motion and Control lab at Cleveland State University, which is depicted in Figure 4.1.

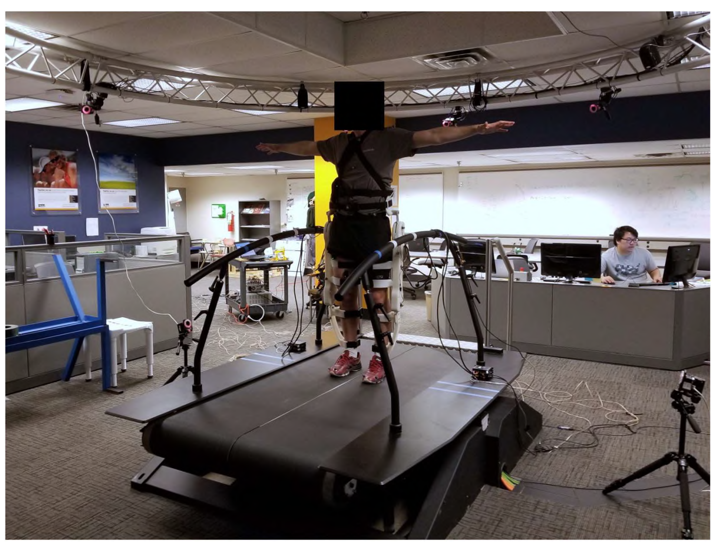

Figure 4.1 The experimental set-up, including the motion capture system and the powered lower-limb orthosis on the subject

4.2.2 Experimental Protocol

The subject participated in the experiment for two sessions which were separated by two weeks. The sessions entailed the subject walking on a level treadmill without or with the exoskeleton. The participant became acquainted with the exoskeleton in the first session, which was treated as a training session. The subject chose a comfortable walking speed in the first session for the treadmill speed. A comfortable gait period and the controller parameters were chosen in the second session.

The subject walked on the treadmill in the second session under four scenarios: initial baseline condition, unassisted condition, assisted condition, and final baseline condition. In both baseline conditions, the subject walked naturally without the exoskeleton. In the unassisted condition, the subject walked while wearing the exoskeleton but without assistance; the orthosis was unpowered. In the assisted condition, the subject walked while wearing the exoskeleton but this time with assistance; the orthosis was powered and the controller was enabled. In each of the conditions, the subject walked for at least six minutes. The subject walked with the use of a metronome to keep correct heel-strike timing of both legs.

4.2.3 Control Strategy

The control strategy used for assistance in this chapter is a PD controller for trajectory tracking. The reference was the nominal healthy gait pattern using data from Winter [53]. The reference trajectory assumed the gait period to be constant. Each leg was controlled independently. The controller took the form

$$\boldsymbol{u} = \boldsymbol{P}\tilde{\boldsymbol{q}} + \boldsymbol{D}\dot{\tilde{\boldsymbol{q}}} \tag{4.1}$$

where $\boldsymbol{u}$ is the vector of control torques supplied by the actuators, $\tilde{\boldsymbol{q}}$ and $\dot{\tilde{\boldsymbol{q}}}$ are the vector of joint angle and velocity errors, and $\boldsymbol{P}$ and $\boldsymbol{D}$ are the diagonal matrix controller gains. The elements of $\boldsymbol{P}$ and $\boldsymbol{D}$ varied in value depending whether the leg was in stance or swing phase. A leg was in stance phase when the ground reaction force for that leg exceeded an experimentally tuned threshold, and otherwise was in swing phase. The control system block diagram is shown in Figure 4.2 and the controller gains are shown in Table XV.

4.2.4 Recording and Processing the Data

To record kinematics, 27 reflective markers were placed on the subject and the coordinates were recorded using the Vicon motion capture system (Oxford, UK). For the conditions when the subject wore the exoskeleton (unassisted and assisted conditions), some markers were placed on the orthosis rather than the participant. The recorded data were measured with a 100 Hz sampling frequency. In some instances, the cameras in the motion capture system were unable to view some markers due to the treadmill handrail, subject arms, etc. This resulted in some missing datapoints. The marker coordinates were

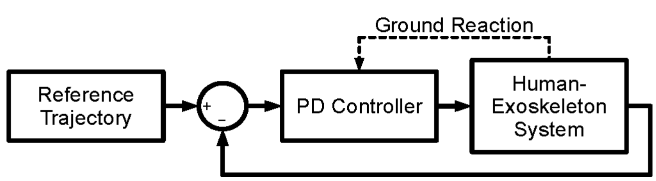

Figure 4.2 Block diagram of the PD control strategy to control the human-orthosis system

Table XV. PD controller gains during the stance and swing phases of gait

	Stance Phase		Swing Phase	
	Hip	Knee	Hip	Knee
$\boldsymbol{P}$ (N·m/rad)	40	20	30	20
$\boldsymbol{D}$ (N·m·s/rad)	2	2	1	1

passed through a smoothing spline with a smoothing parameter which gave a roll-off frequency of 13.1 Hz. This was used to interpolate the missing data points while also providing an initial low-pass filter on the data. The joint angles, velocities, and accelerations were calculated based on the marker coordinate data using a kinematic model based on the subject height and derived body segment lengths from Winter [67]. The center of mass of the body segments were calculated similarly. These calculated values were passed through a 6th-order Butterworth filter with a cut-off frequency of 3 Hz.

The ground reaction force and center of pressure of each leg were measured using a Motek Medical B.V. split-belt treadmill (Amsterdam, Netherlands). The recorded data were also measured with a 100 Hz sampling frequency. A smoothing spline with the same 13.1 Hz roll-off frequency was also used to pre-process the data. The final data were passed though a 6th-order Butterworth filter with a cut-off frequency of 3 Hz. Note that these vertical ground reaction force measurements were used to partition the gait into stance and swing phases. The beginning of gait at 0% of the gait cycle was defined as the moment of heel-strike, which occurs at the beginning of stance phase.

The orthosis in the unassisted and assisted conditions interfaced with dSPACE MicroLabBox (Paderborn, Germany) for data acquisition and control. The software was configured to record and control at 1000 Hz sampling frequency and the hardware was arranged to measure the raw vertical ground reaction force data. The ground reaction force data were used to determine whether the legs were in stance or swing phase, which affected the later-described controller. In addition, these data were used to synchronize dSPACE with other data acquisition sources. The orthosis torques were assumed to be proportional to the actuator currents, with proportionally constant based on the actuator transmission ratio and motor constant.

Inverse dynamics was used to calculate the net torque of the joints, using a different model for the conditions. Since the subject did not wear the exoskeleton in the baseline condition, the links of the models were only based on body segment masses and inertias of the subject. The model parameters of the body segments were calculated from Winter [67] using the bodyweight and height of the subject. For the other conditions, namely unassisted and assisted conditions, the model used in the inverse dynamics calculation incorporated additional mass and inertia representing the orthosis. The device component weights were directly measured, and inertias were approximated using simple geometry.

The user torque can be calculated from the net joint torque previously described and powered orthosis torque measured by dSPACE. In the baseline and unassisted conditions, the powered orthosis torques were a constant zero since the device was either not worn or worn in an unpowered state. In these two conditions, user torque simply equals net joint torque. However, the net torque in the assisted condition also includes torques from the powered orthosis. User torque in this condition was calculated by subtracting the orthosis torque from the net joint torque.

The user power was calculated by taking the product of user torque calculated via net joint torque and inverse dynamics, and joint angular velocity calculated from the motion capture system marker coordinates. This user power was separated into positive values corresponding to the mechanical power generated for positive work done by the user, and negative values corresponding to the mechanical power absorbed for negative work done by the user. The separated signed user powers were integrated to calculate mechanical energy generated and mechanical energy absorbed.

Note that the models used in inverse dynamics are based on pure rigid body dynamics. Any unmodeled dynamics would result in inaccuracies in the net torque calculations, and thereby also affect the user torque, power, and energy calculations. The primary source of unmodeled dynamics would be from the orthosis. Specifically, the actuators exhibit Coulomb friction, previously calculated at around 1.1 Nm in Section 3.3. Subsequent observations working with the hardware suggests there may be other, more sophisticated dynamic behavior, such as LuGre friction. Since the orthosis torque was assumed to be proportional to motor current and the inverse dynamics calculation ignored frictional effects, the net joint torque and user torque calculations in the unassisted and assisted condition may be inaccurate, possibly up to around 1.1 Nm for torque.

Delsys surface EMG sensors (Massachusetts, USA) were placed on the subject to measure the activation of various muscles on the left leg of the subject, which was the dominant leg of the subject. Specifically, the sensors were placed on the Gluteus Maximus, Semitendinosus, Biceps Femoris, Rectus Femoris, Vastus Lateralis, Vastus Medialis, Medial Gastrocnemius, and Soleus. A sampling frequency of 1000 Hz was used to record the data. A linear envelope [100] was then used to process the data. This is accomplished by first applying a 20th-order bandpass filter with frequencies ranging from 25 to 400 Hz, second passing the data through a full-wave rectifier to make the values positive, and third applying a 2nd-order low-pass filter with cut-off frequency of 8 Hz. To represent the overall muscle activation magnitudes throughout gait, these were integrated across each full gait cycle. All reported EMG linear envelopes and integrated values are normalized such that the EMG values in the final baseline condition for each muscle were equal to one.

The Butterworth filters in this section were each applied two times, once in the usual forward direction and once in the reverse direction, to give zero phase offset. The EMG measurements were shifted in time to account for latency in the used wireless EMG sensors. The ground reaction force data were used to synchronize the various data acquisition sources. The convention for joint angles and joint torques are such that flexion and dorsiflexion are positive and extension and plantarflexion are negative. The convention for power and energy are such that energy generated by the user are positive and energy absorbed by the user are negative. The torque and energy values that are reported are normalized to the subject bodyweight. Grubb's two-sided test was used to systematically remove outliers using the variables: stride period, toe-off timing, RMS net joint torque, and EMG values.

4.2.5 Statistical Analyses

The calculations and analyses were done for the left leg of the subject, which was the dominant leg of the subject. The significance level in statistical analyses was set to $\alpha = 0.05$ prior to any correction factors for multiple-comparison analyses. The primary multiple-comparison results compare the following conditions: final baseline condition (B), unassisted condition (U), and assisted condition (A).

The mean toe-off timing, mechanical energy generated, mechanical energy absorbed, and muscle EMG values were statistically compared across the three conditions in a multiple-comparisons analysis using paired t-tests. None of these variables demonstrated clear severe violations of the conditions necessary for t-test, namely the variables were normally distributed and their standard deviations were approximately equal. The multiple-comparison analyses were each Tukey-Kramer corrected. Additional Bonferroni corrections were applied across joint-wise comparisons for mechanical energy generated and absorbed, and across muscle-wise comparisons for EMG values.

The mean torque as a function of percent of the gait cycle also underwent a multiple-comparisons analysis using paired t-test. Since these are functions of an independent variable rather than scalar values, a statistical parametric mapping (SPM) framework was used [101]. The independent variable was the percent of the gait cycle, which was treated as cyclic in the analysis. A Bonferroni correction was applied to the multiple-comparisons analysis.

4.3 Experimental Results

This study did not follow the protocol that was original sought and was modified to follow what was described Section 4.2.2. The original protocol included the four conditions taking place on each of three sessions. The control law for the assisted condition was planned to include a gravity compensation term, and the healthy gait from the baseline condition in the first session was planned to be used as a control reference trajectory for the subsequent second and third sessions. However, due to technical difficulties and time constraints, not all conditions were completed in the first session and the gravity compensation term was not implemented. The healthy gait from the second condition was planned to be used in the third condition for the reference trajectory.

However, the third session was cancelled due to circumstances relating to the 2020 COVID-19 pandemic. The results presented in this chapter are based on the second session. In this session, the gravity compensation term was not included in the controller and Winter gait data was used as the reference trajectory rather than the planned baseline data.

In the second session, a hardware connection issue resulted control during the assisted condition to become inadvertently disabled on the right leg. The controller went offline mid-experiment and remained offline for the remainder of the assisted condition. The data after this moment was not used in analysis.

During the unassisted condition of the first session, the subject chose the walking speed of 0.8 m/s. In a control test with the exoskeleton, the participant chose a comfortable cadence of 80 steps/min, which was used to determine the reference trajectory period. This cadence was kept consistent throughout the conditions by using a metronome, which was aligned to match heel-strike of the participant and reference gait for both legs.

The results presented in the subsequent sections use data which were trimmed to remove the first 20 s of data. This was done to avoid affects from the participant starting the treadmill walk. The data were trimmed to discard data after the moment the right leg controller became disconnected in the assisted condition. For analysis, 58 gait cycles, which is around 87 s of data, were used from all conditions.

4.3.1 Kinematics

The subject gait for the three compared conditions is shown in Figure 4.3 with Winter data [53] superimposed. The three conditions behaved similarly and resembled the healthy gait pattern from Winter. A change in gait at the hip and knee joints from baseline to unassisted was observed with a respective RMS difference of 4.61 and 11.11 deg, which may be due to wearing the orthosis when unpowered. The assisted condition partially restored the gait pattern to be closer to baseline and Winter data. The RMS difference between of the baseline and assisted condition was 2.17 and 7.73 deg at

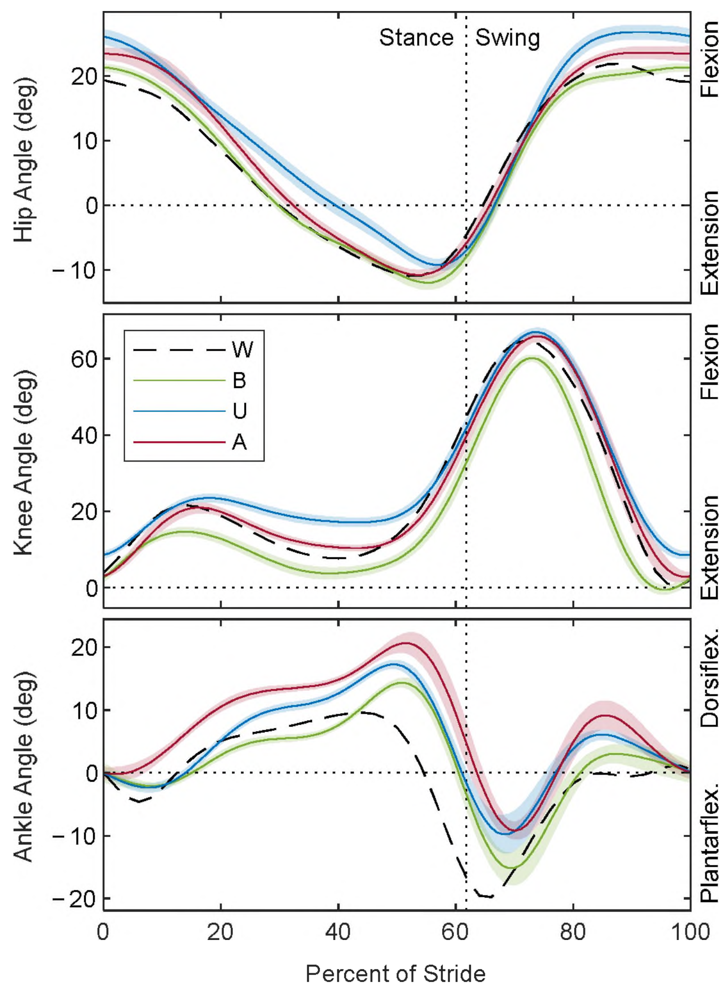

Figure 4.3 Ensemble average and standard deviation of gait for the baseline (B), unassisted (U), and assisted (A) conditions with Winter data (W) superimposed

the hip and knee, respectively, a reduction in both cases. A change in gait at the ankle joint from baseline to unassisted was also observed, with an RMS difference of 3.59 deg. However, this was not restored in the assisted condition, where the RMS difference between baseline and assisted conditions was the larger value of 6.26 deg. This may be due to the ankle joint being an unactuated joint.

The ankle angle differed considerably from Winter data for all three conditions, more so than the hip and knee joints. The RMS error between the baseline and Winter data, normalized to the RMS Winter data, was 0.13 for the hip and 0.23 for the knee, versus the larger 0.65 for the ankle. Similar larger ankle errors than hip and knee errors are observed for the unassisted and assisted conditions. For the unassisted condition, the values were 0.37 for the hip and 0.18 for the knee, versus 0.84 for the ankle. For the assisted condition, the values were 0.20 for the hip and 0.09 for the knee, versus 1.21 for the ankle. The larger ankle deviation compared to hip and knee deviation from Winter data is likely due to a different procedure being done for calibration for this joint over the other joints. The hip and knee angles were defined as zero when the body segments were oriented such that the torso, thigh, and shank were vertical. However, the ankle angle was defined differently due to not having a clear vertical orientation. Rather, the ankle angle was defined as zero at heel-strike. Although this may not perfectly align with the standard definition being 90 deg between the foot and shank body segments, this definition does not affect the calculations and presented comparisons of user effort. Data with the foot resting flat on the treadmill would resolve this issue, but data in this scenario was not recorded.

The timing of the toe-off of the foot is depicted in Figure 4.4. For comparisons of scalar quantities using paired t-tests, a statistically significant difference would be indicated by the pair of confidence intervals for the conditions of interest being disjoint. Figure 4.4 includes the 95% confidence intervals of toe-off timing, after multiple comparisons correction, for each of the three conditions and marks the pair of conditions where a statistically significant difference was found. There was not a statistically significant difference in toe-off timing between unassisted and baseline conditions ($p = 0.063$), and the assisted and baseline conditions ($p = 0.16$). The only comparison with a statistically significant difference found was the unassisted-assisted comparison ($p < 0.001$). However, this was by a small margin, with less than a 1% absolute difference in the mean values. Overall, all values were around 62% to 63%, which is the expected timing for toe-off [15].

4.3.2 Kinetics

The user torque for the three compared conditions is shown in Figure 4.5 with the controller torque for the assisted condition superimposed. Each pair of conditions is compared using a paired t-test via SPM analysis; the test statistic is shown in Figure 4.6. Suprathreshold clusters, which occur in intervals where the absolute value of the test

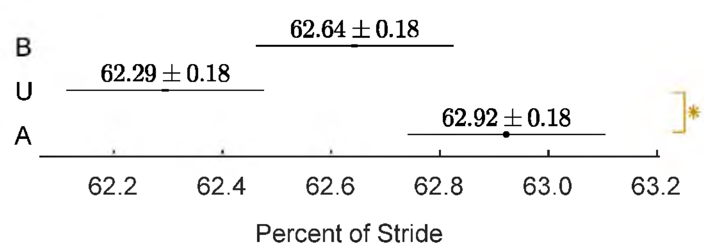

Figure 4.4 Mean with 95% confidence interval of toe-off timing for the baseline (B), unassisted (U), and assisted (A) conditions

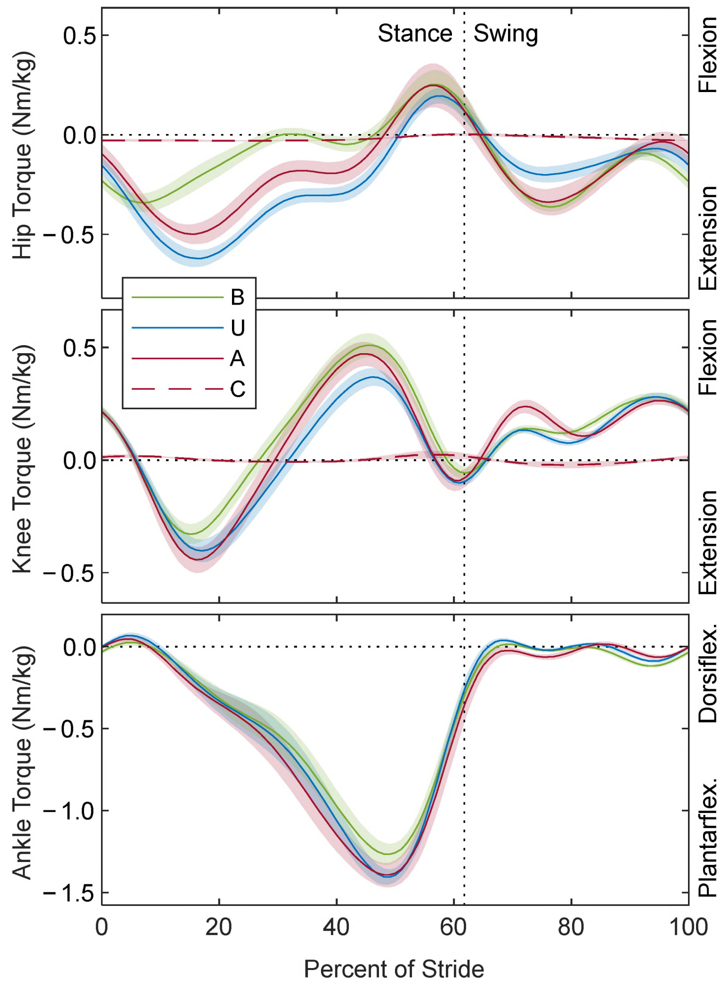

Figure 4.5 Ensemble average and standard deviation of user torque for the baseline (B), unassisted (U), and assisted (A) conditions with Winter data (W) superimposed

statistic exceeds some SPM-determined value, show over which time intervals statistical significance is found for the differences in torques.

User torque at the hip in mid-stance increased in magnitude in the unassisted and assisted conditions compared to baseline. The assistive condition restored this closer to baseline to a statistically significant but marginal degree. This was also noted for early- to mid-swing.

User torque at the knee in mid- to late-stance was higher in value in baseline than unassisted condition. This had the effect of an increase in magnitude in mid-stance and

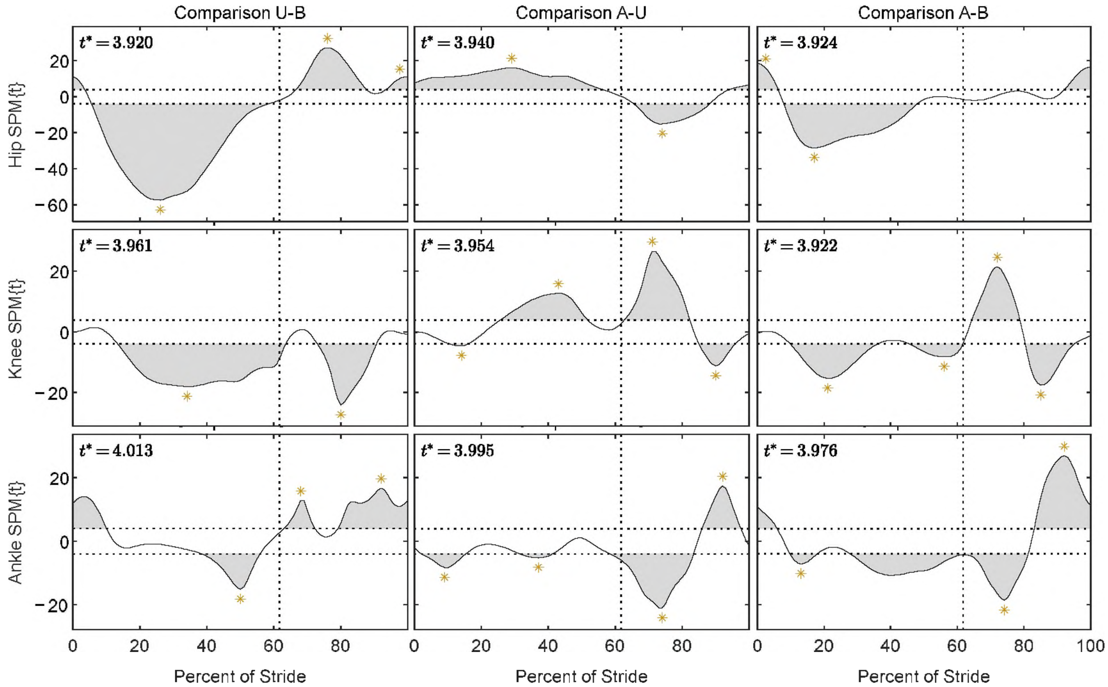

Figure 4.6 Paired t-test test statistic in user torque SPM analysis comparing the baseline (B), unassisted (U), and assisted (A) conditions

decrease in magnitude in late-stance from baseline to unassisted condition. For the unassisted and assisted condition comparison, a statistically significant difference was found for mid- to late-stance but not for early- to mid-stance. For the assisted condition and baseline comparison, a statistically significant difference found in increase in magnitude in early- to mid-stance and a decrease in magnitude in late-stance. The assisted condition showed larger magnitudes in early-swing in the unassisted than baseline conditions. The torque was only marginally lower in late-stance. The unassisted condition had smaller torque magnitudes than baseline in mid-swing.

User torque at the ankle saw an increase in torque from baseline to both unassisted and assisted conditions in late-stance, near push-off. This may be due to the added weight of the exoskeleton. Swing phase differed in torque values over many intervals. However, the data in swing may be unreliable for the ankle since the foot has low mass.

4.3.3 Mechanical Energy

The mechanical energy of the subject joints generated and absorbed throughout locomotion for the three conditions are shown in Figure 4.7. For the energy generated case, all pair of conditions for each joint saw a statistically significant difference. An increase in energy generated by the subject was observed from baseline to unassisted condition at the hip and ankle joints, and a decrease was observed at the knee joint for the same comparison. A decrease in energy generated was observed from unassisted to assisted condition at the hip and ankle joints, whereas an increase was observed at the knee joint. At all three joints, the assisted condition returned the energy values closer to baseline value to a statistically significant degree.

For the energy absorbed case, all pairs of conditions for each joint saw a statistically significant difference except for the assisted-baseline comparison at the hip joint and unassisted-baseline comparison at the ankle joint. A decrease in energy generated was observed at the hip from the baseline to unassisted condition, whereas an increase was

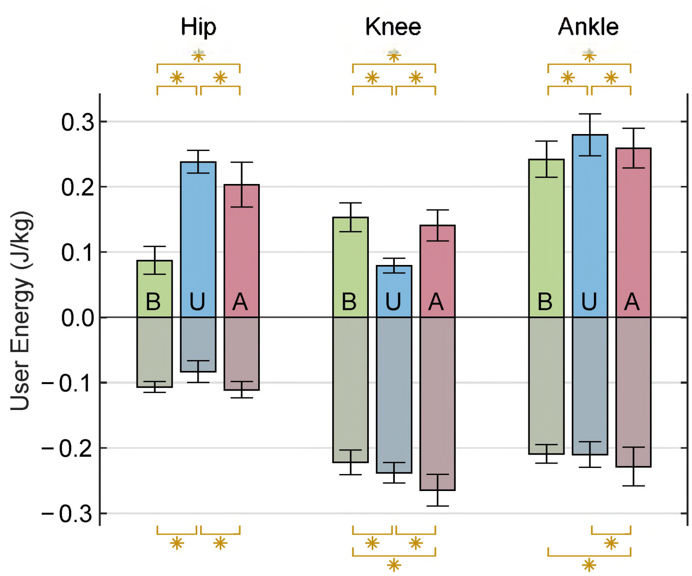

Figure 4.7 Mean and standard deviation of mechanical energy of the subject generated (positive) and absorbed (negative) for the baseline (B), unassisted (U), and assisted (A) conditions

observed at the knee. Interestingly, an increase occurred at all joints from unassisted to assisted condition.

4.3.4 Electromyography

The linear envelopes of the EMG signals for each of the muscles is presented in Figure 4.8. The comparisons of the EMG values representing the cumulative effect throughout locomotion are shown in Figure 4.9. The figures are normalized such that the EMG values in the baseline condition are one. The Gluteus Maximus was excluded from the results due to the EMG sensor for that muscle becoming unintentionally inactive in the assisted condition.

A statistically significant difference across the conditions was not found in the EMG values for the Semitendinosus and Rectus Femoris. The Biceps Femoris demonstrated smaller EMG values in the unassisted condition compared to both baseline and assisted conditions. Smaller values were also observed in the same muscle from baseline to assisted condition. The Medial Gastrocnemius similarly had smaller EMG values in the unassisted condition than in the baseline condition. However, there was no observed statistically significant difference between the assisted and baseline conditions. The Vastus Lateralis and Vastus Medialis saw increase in EMG values from the unassisted condition to the assisted condition. Only the Vastus Medialis saw an increase from baseline to assisted condition. The Soleus demonstrated a decrease in EMG values from the unassisted and assisted to assisted condition.

For the purpose of checking if EMG sensor measurement or properties have changed

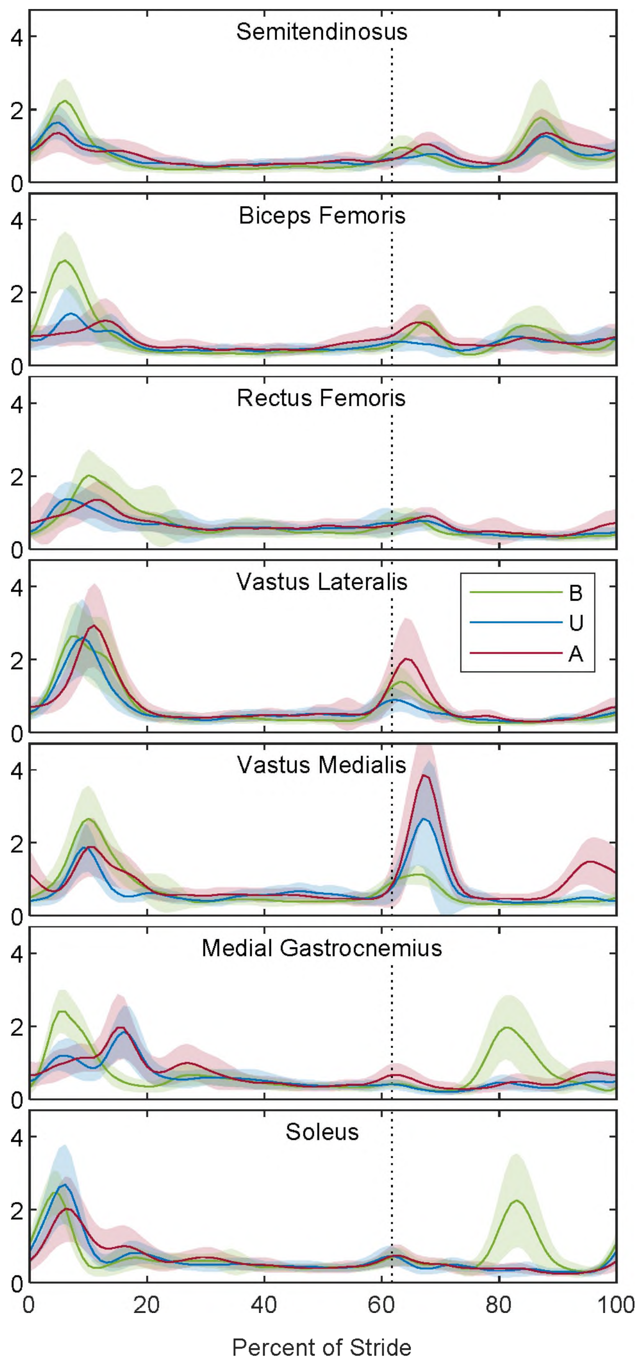

Figure 4.8 Ensemble average and standard deviation of the linear envelopes of EMG measurements of the subject muscles for the baseline (B), unassisted (U), and assisted (A) conditions

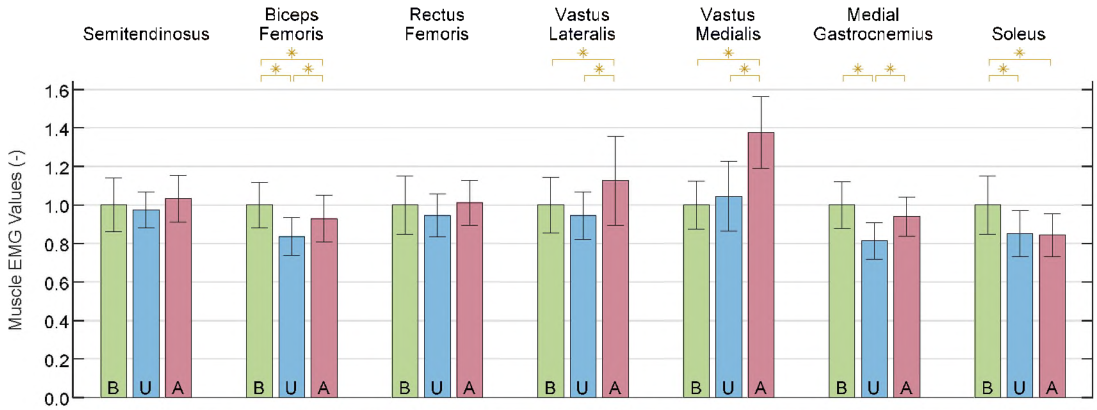

Figure 4.9 Mean and standard deviation of EMG values for the baseline (B), unassisted (U), and assisted (A) conditions

from the beginning of the session to the end of the session, a separate comparison was conducted between the initial baseline (I) and the final baseline (F) conditions. The EMG values for the Semitendinosus and Biceps Femoris were not included because they were removed from the subject and replaced after the initial baseline condition so they did not interfere with the cuffs of the orthosis. The comparisons of the EMG values between these two conditions are shown in Figure 4.10. A statistically significant difference was found in the Vastus Lateralis, Medial Gastrocnemius, and the Soleus, but not found in the Rectus Femoris and Vastus Medialis.

4.4 Discussion

4.4.1 Comparisons

The kinematic data did change across the conditions but only by a marginal degree. The gait patterns for the unassisted and assisted conditions resemble healthy walking data from baseline, and the gait patterns for all conditions resemble healthy walking data from Winter [53]. The ankle tended to have more error than the hip and knee joints, likely due to the method for calibration being different. The toe-off timing only changed marginally

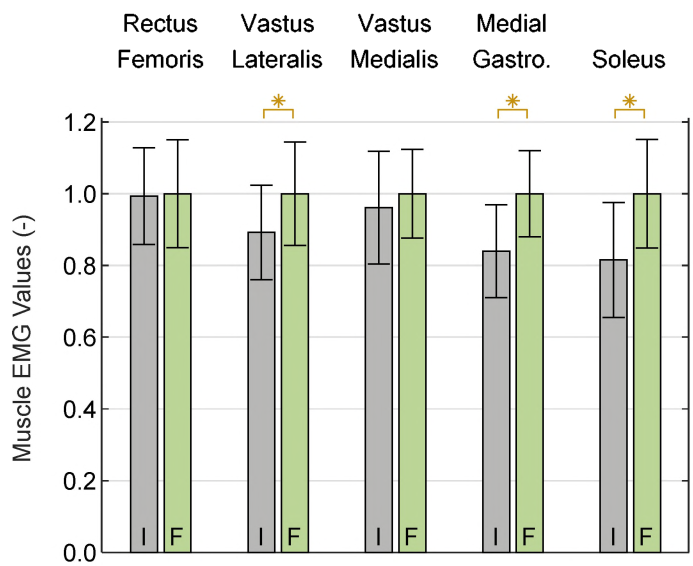

Figure 4.10 Mean and standard deviation of EMG values for the initial baseline (I) and final baseline (F) conditions

or did not change to a statistically significant degree. It is reasonable to expect these two facts of small or no change in gait and toe-off. When mass is added to the waist, thigh, or shank weighing roughly equal to or less than the 6 kg powered orthosis in this chapter tends to give not change or marginally change gait [102]. This is promising since it suggests the powered orthosis may be light enough to not interfere with gait.

Note that preferred gait parameters such as walking speed and cadence could change from the baseline to the unassisted or assisted conditions. However, subject preference for these parameters were not experimentally tested in the conducted study. A constant treadmill speed and the use of a metronome controlled for these parameters, keeping them constant across conditions.

A decrease in torque levels from baseline or unassisted to assisted would indicate walking assistance. However, the kinetics showed the user torque magnitudes primarily increased from the baseline and unassisted conditions to the assisted condition. An increase in torque occurred at the hip and knee joints in most gait phases. At these joints, an increase was noted from baseline to unassisted conditions. The assisted condition marginally restored this closer to baseline levels. These changes were not solely due to the power supplied by the powered orthosis at the actuated hip and knee joints, but also due to changes in the gait of the subject even though the changes were relatively small. An increase in ankle torques occurred from the baseline to the unassisted and assisted conditions. This is likely due to the added weight from the orthosis in these conditions and how the orthosis did not actuate the ankle joint. In addition, the change in ankle torque are relatively small, which suggests the powered orthosis may be light enough to not significantly affect ankle joint torques near push-off.

The calculation for torques at the hip and knee joints relied on a model of the system which excluded friction. However, the friction in the actuators at these joints were roughly 1.1 Nm, or 0.014 Nm/kg. Any statistically significant differences in torque at the hip and knee joints at around this value or smaller may be unreliable. This does not apply to the ankle joint since the orthosis did not include an AFO component.

The actuators supplied a maximum of 2.3 Nm in the assisted condition, which is significantly smaller than the peak torque of 39.7 Nm observed from the subject in the baseline condition. This is not surprising for two reasons. First, the controller gains were selected conservatively, chosen to be small for safety reasons and to permit human-robot cooperation. The values were increased from smaller values in a different assisted condition not shown in this work. However, the researchers that were conducting the experiment decided the gains were not sufficiently large. The condition was repeated using higher gains, which the results here are based on. A further increase in controller gains could have been possible. The second reason for the small actuator torque is due to gait not deviating significantly from the healthy gait pattern used for the reference. It is possible that the subject became acclimated to the particular reference enforced by the assistive controller. In this case, the subject would still be putting in significant effort in walking. In order for the controller to possibly assist, the participant would need to relax the muscle, thereby lagging behind the reference trajectory, which was not strictly observed. Note that the inclusion of the gravity compensation term in the controller which was originally planned would have likely increased the torque magnitudes supplied by the powered orthosis. In this scenario, user effort would more likely be reduced, and the subject would not necessarily need to have this lag behind the reference. However, this term was not incorporated so the controller presented here is not ideal for the application of assistance.

A decrease in mechanical energy generated from baseline or unassisted to assisted would indicate walking assistance. However, the changes observed across conditions were inconsistent. The hip increased in energy generated from baseline to both unassisted and assisted conditions, likely due to requiring more effort from the subject to move the combined mass of the human body and orthosis. The hip decreased in energy generated from the unassisted to assisted condition, since power supplied by the powered orthosis can help with the motion. Interestingly, the knee behaved in an opposite manner. The energy generated decreased from baseline to unassisted condition, and the energy generated increased from unassisted to assisted condition. Friction may have contributed to the decrease by reducing knee motion in swing phase. The reason for the increase is not known. An increase was observed in mechanical energy absorbed at the ankle from the baseline to the unassisted and assisted conditions. This may be due to similar reasons for the increase in ankle torque. That is, the additional mass of the orthosis without supplemented power at the ankle would mean the subject requires more effort at the ankle.

An increase in mechanical energy absorbed from baseline or unassisted to the assisted condition would indicate the subject absorbed some of the energy supplied by the powered orthosis. An inconsistent change was observed. At all joints, this absorption was observed from the unassisted to assisted condition. Only at the knee and ankle joints was this observed from the baseline to assisted condition. The magnitude of the increase was marginal, being only around 0.03 J/kg from unassisted to assisted conditions at the hip and knee joints.

Although the joint-level energy calculations can provide some meaning, caution should be taken to not overextend the practical interpretation. Metabolic cost tends to be poorly estimated from joint-level measurements due to the muscle biarticulation of the joints and elastic effects in the tendons [11]. The decrease in the mechanical energy generated from the unassisted to assisted condition at the hip does not necessarily mean there was a decrease in the energy generated by the muscles that articulate the hip.

A decrease in muscle activation as measured using EMG from the baseline or unassisted condition to the assisted condition would indicate assistance. However, the changes in the recorded EMG values were inconsistent. The EMG values of the Biceps Femoris decreased from baseline to the unassisted and assisted conditions. This primarily occurred in early stance phase, where the knee was more flexed at the beginning of the gait cycle thereby requiring less motion in early- to mid-stance phase from the subject. In addition, control in the assisted condition may have contributed to the decrease from baseline. The EMG values of the Vastus Lateralis and Vastus Medialis increased from the baseline to assisted condition, primarily around early swing phase. The reason for this increase is unclear since knee extension appears similar around this time the gait cycle. The EMG values of the Medial Gastrocnemius decreased from the baseline condition to the unassisted conditions. This occurred mostly around mid-swing phase and may have occurred due to friction may have contributed to the deceleration of the knee extension. Also, the EMG values throughout the entirety of the gait cycle increased from the unassisted condition to the assisted condition. This may be due to the orthosis motion not being perfectly coordinated with the subject with the knee being more flexed in most of the gait cycle of the assisted condition than in the unassisted condition. The EMG values of the Soleus also decreased from baseline to unassisted and assisted condition. This occurred primarily in mid- to late-swing phase, though the reason for this decrease is unknown. The lack of an AFO component of the orthosis should only indirectly affect ankle plantarflexion during swing phase.

In the above comparisons of EMG value involving the baseline condition, some caution must be taken with interpreting the results. Specifically, comparisons with the Vastus Lateralis, Medial Gastrocnemius, and Soleus muscles should consider how the initial baseline and final baseline conditions differed to a statistically significant degree. The non-marginal change in muscle activation between these conditions may be due to muscle fatigue or sweat. However, some evidence suggests EMG measurements should decrease with prolonged activity and increased subject fatigue rather than increase [103].

During the walking experiment in the assisted condition, the participant commented how the powered orthosis made walking feel easier. However, when comparing the assisted and unassisted conditions, the torque magnitudes, mechanical energy generated, and EMG measurements did not consistently decrease user effort. The contradiction between the inconsistent measures quantifying user effort and subjective experience of decrease in user effort may be due to the energy absorbed. Some amount of energy absorbed was observed when comparing the assisted condition to the unassisted condition the participant completed just before.

4.4.2 Limitations and Future Work

The assistive control work presented in this chapter is limited in several ways and can be improved in future work. First, the PD control approach from this chapter is less than ideal for its ability to provide assistance to a subject since it does not promote cooperation between the subject and the powered orthosis. The gravity compensation term originally planned to be included in the control law would increase the torque provided by the orthosis significantly. The additional torque would increase the likelihood for an observable decrease in user effort and give more consistent results. In addition, the trajectory tracking control approach enforces a specified reference. The powered orthosis could hinder the user if the reference trajectory differs from the desired motion of the subject. A control strategy that does not enforce a particular reference trajectory may be better suited. For example, adaptive oscillators can be used to derive a reference in cyclic motions, which has the potential to improve cooperation and assistance [97]. Another approach could be to employ a control strategy that does not use any reference trajectory. For example, one could take a feed-forward approach [53]. Alternatively, a dynamic model can be used for pure gravity compensation control [96], inertia compensation control [95], or combined inverse dynamics control. A body-in-the-loop approach can be taken to optimize user effort in real-time [104].

Second, only a single healthy subject was used in this study, which limits the generalizability of the results. The hardware design will undergo further design changes to allow fitting of multiple users. This will permit conducting a larger scaled study involving multiple healthy subjects. Note that the design requirements were dictated from the needs of the pediatric population, which can limit the assistive capability of the orthosis on adults. The conclusions drawn from results carried out on adults may not carry over to children.

Third, only torques, mechanical energy, and EMG measurements were compared in this work. Metabolic cost was not measured nor compared, which is considered important for design and evaluation of assistive powered orthotics [98]. In addition, the SPM analysis was only applied to the torque values. It may also be applied to EMG measurements and joint mechanical power calculations, providing a systematic way to choose intervals throughout the gait cycles in which a statistically significant difference is found for further post-hoc investigation. This is in contract with the current approach, which compares scalar values representing the cumulative effect of the entire gait cycle and, for EMG measurements, noting where the most significant contribution occurred by looking at the time series figure. Also, friction was excluded from the dynamic model used in the joint torque calculations at the hip and knee joints, which can call to question the accuracy of the comparisons of user torque and mechanical energy at some points in the gait cycle. The reliability of the comparisons could be improved by incorporating friction and possibly other unmodeled dynamics.

Fourth, the statistical analyses assumed that the gait cycles and test conditions were completely independent. However, fatigue and other factors could result in a time-varying effect which would make this assumption false. These effects could perhaps be separated and removed through other statistical analyses.

4.4.3 Conclusions

In summary, this chapter presented an experimental study using the anthropometrically parametrized orthosis for assisting a subject in level walking on a treadmill. Results show user torque primarily increased in magnitude, mechanical energy generated changed inconsistently, and muscle activations changed inconsistently. In conclusion, the results are inconclusive whether the device can be used for assistance, at least for the particular control strategy, version of the orthosis, and participant.

This inconclusive result is likely due to the control strategy applied in the study not being well designed for assistance of able-bodied subjects. The peak torque produced by the actuators was around 2.3 Nm, much smaller than the 39.7 Nm of the healthy walking of the subject without the orthosis. This small value in the actuator torque may be due to low gains and the subject following a similar gait pattern as the healthy gait pattern used as a reference trajectory in the controller. A PD controller may be more appropriate for use in a clinical context, such as for gait guidance or rehabilitation of patients with unhealthy gait. A control law with gravity compensation was originally planned. However, the last session in the study was canceled and gravity compensation was not included due to technical difficulties and time constraints.

Even though the study did not follow the original protocol and has some limitations, it does show promising preliminary results. This work will act as a foundation for future endeavors of studies involving subjects and development of the powered orthosis. There were not any significant problems with the first trial in the conducted study. The orthosis will undergo future revisions based on feedback from the participant and to make it applicable to multiple subjects. Future work entails extending these initial results to involve multiple participants and explore other control approaches, generalizing the results. This work is the first major milestone involving subject in taking steps towards the development of a pediatric version of the orthosis designed for assisting and rehabilitating children with CP.

4.5 Acknowledgements

The contributions of Huawei Wang and Anthony Goo are greatly appreciated, as they have devoted significant amount of time and assistance in conducting the experiment described in this chapter. In addition, I would like to thank the subject for volunteering numerous hours to participate in this study and for providing feedback on possible future improvements of the powered orthosis.

CHAPTER V

CONCLUSIONS

This dissertation presented the development of a powered pediatric lower-limb orthosis and evaluation of the developed hardware. Specifically, development entailed (1) design requirements, (2) design of joint actuators, (3) design and fabrication of a provisional orthosis, and (4) design and fabrication of a prototype anthropometrically parametrized orthosis. Evaluation entailed (5) actuator capabilities testing, (6) gait tracking experiments, (7) standing balance simulations and experiments, and (8) assistive control experiments. This final chapter summarizes the work accomplished in this dissertation with context for its contribution to society, and outlines possible future directions of research towards the development of the pediatric orthosis.

5.1 Contributions

This work entailed three major components. The first component included researching the design requirements, developing the joint actuators, and functional testing of the actuators. The design requirements were based on the target population age range of 6 to 11 years with the eventual goal of using the device for children with gait disorders like CP for walking assistance and rehabilitation. These requirements were used to determine the desired specifications of the actuator, which were fabricated for use in an orthosis. Some basic characteristics of the actuators were measured or experimentally evaluated, namely continuous and peak torque capability, maximum operational speed, and friction levels.

The second component entailed the development of a provisional version of the orthosis, the development of a testing platform, and experimental evaluation of the actuators in gait tracking and standing balance. The provisional orthosis was designed to house the actuators and was fabricated for the size of an average 8 year old child. It was designed for use in basic testing of the actuators in an orthosis in a well-controlled manner. A testing platform was also developed as a test bed for experimental testing with the provisional orthosis. The provisional orthosis was then used to test the actuators using the testing platform in a couple experiments. A gait tracking experiments were performed to test the actuators in controlling to follow a healthy gait pattern without contact with the ground, and standing balance simulations and experiments was performed to further test the actuators for a different objective when the orthosis is in contact with the ground.

The third component included the development of the anthropometrically parametrized orthosis and its experimental evaluation for walking assistance. This part of the research extended the provisional version of the orthosis to include the possibility to work with a subject. The orthosis frame was developed in terms of the anthropometrics of the subject and was fabricated using additive manufacturing for a particular individual which is compatible with the actuators. The newly developed orthosis was then used for experimentally testing the hardware for walking assistance with an able-bodied subject.

The main contribution of this dissertation is the development of the anthropometrically parametrized orthosis. Put concisely, the experiments conducted above have shown the actuators are capable and the orthosis can be used with a subject. All developments were made with the target children in mind, namely children 6 to 11 years with walking abnormalities from disorders such as CP. The works presented here were the necessary first steps to this end and will act as a foundation for continued development of the powered orthosis towards this long-term goal.

5.2 Research Prospects

This dissertation covered the initial development of a powered orthosis designed for rehabilitation and assistance of children. The primary result of this work is the realization of an anthropometrically parametrized orthosis with a design methodology applicable to children in the target age group. This lays the foundation for future endeavors in pursuit of a device capable of assisting and rehabilitating children ages 6 to 11 years with CP—the long-term goal of the device. One possible path towards this goal is depicted in Figure 5.1 and is described in more detail in the subsequent paragraphs.

With the initial development complete, the next primary objective is to make the orthosis hardware applicable to more than a single subject. The current version of the orthosis was designed for a particular individual, which limits its possible use. The next version of the orthosis design should be able to accommodate multiple adults without needing to fabrication of a new frame for each subject, a limitation of the current

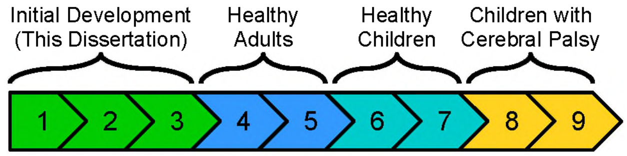

Initial Development (This Dissertation)

1. Determine design requirements, develop actuator, and perform testing of basic actuator capabilities
2. Develop provisional orthosis, develop testing platform, and perform testing with provisional orthosis
3. Develop anthropometrically parametrized orthosis and perform assistive control on a healthy adult subject

Healthy Adults

4. Extend the powered orthosis design from part 2 to be compatible with multiple adult subjects
5. Generalize results from part 3 using the newly developed orthosis from part 4 to multiple healthy adult subjects

Healthy Children

6. Modify the powered orthosis design from part 4 to be compatible with children ages 6 to 11 years
7. Generalize results of part 5 using the newly developed pediatric orthosis from part 6 to multiple healthy children

Children with Cerebral Palsy (Long-Term Goal)

8. Develop a walking assistance control strategy specific for children with cerebral palsy and apply the assistive controller to multiple children in the target age group
9. Develop a rehabilitative control strategy for children with cerebral palsy and experimentally evaluate the controller for lasting positive outcomes in gait

Figure 5.1 Outline of a possible path towards the vision of a pediatric orthosis for walking assistance and rehabilitation of children with cerebral palsy

hardware. This can be accomplished by making the link lengths adjustable without considerably sacrificing the weight of the orthosis. In addition, the new design should address issues encountered with the current version of the hardware. For example, the thigh cuffs are thin and fragile, and the shank cuffs are excessively thick and can cause comfort issues for the subject. With new hardware developed, the powered orthosis can then be tested on multiple healthy adult subjects. This will generalize the results from the assistive control work in this dissertation to a broader adult population. In this process, the limitations of the study described in Section 4.4.2 can be addressed.

Once the adjustable version of the device has been well-tested with multiple healthy adults for walking assistance, the next objective is to repeat the same process but with children. The adult orthosis at this stage will certainly have some limitations and room for improvement. The orthosis design can be revised to accommodate children, while also addressing the limitations of the adult device. At this point of device iteration, the design should be becoming less of a prototype and more finalized. Electronics should be mostly or completely internal; the device should be lightweight and approachable; donning, doffing, and adjustment should be quick. With the new pediatric hardware developed, the powered orthosis can then be tested on multiple healthy children for walking assistance, possibly following a similar protocol as done for adults. This will be a major milestone towards the long-term goal of a working pediatric device. The result of this work would bridge the gap from a device for adults in previous versions of the hardware to a device for children in the latest version of the hardware.

With a working adjustable pediatric orthosis fabricated and tested for functionality in walking assistance on healthy children, the next major objective is to work with children with walking disorders, specifically CP. There are two primary purposes of the pediatric orthosis, namely, to provide walking assistance and walking rehabilitation to children with gait disorders. Walking assistance will be addressed to children in a similar manner as done previously with healthy children and healthy adults. However, the control strategy may need to be modified to accommodate the specific needs of these children, such spasticity and contractures, which are common in those with CP [2]. For walking rehabilitation, gait will be one of the primary clinical outcomes to be measured. A particular intervention protocol will have to be determined and the choice of control strategy will need to be considered. For rehabilitation to successful, a lasting effect should occur after the rehabilitation sessions have taken place. Patient gait can be recorded when the subject is not wearing the orthosis, prior to and after the powered orthosis intervention. Ideally, a follow-up or multiple follow-ups should occur months or possibly years after the intervention to determine if the intervention had a lasting effect and rehabilitation was successful. Possibly as a different study, robot-assisted gait training using the pediatric orthosis could be compared to other interventions such as traditional overground or treadmill gait training (without a powered orthosis) [2], [8], [9] or surgery [2], [5]. Such a comparison would show how robot-assisted gait training compares to other interventions for gait rehabilitation.

5.3 Evaluate Technology Readiness for Transitioning to Clinical Testing

The design methodology for the anthropometrically parametrized orthosis allows for the creation of a model for a particular individual. Given the anthropometrics of a person, a model of the orthosis can be created, manufactured, and assembled for the particular individual. This methodology was successfully able to create an orthosis model based on the anthropometrics of average children ages 6, 8, and 11 years old. In addition, this methodology was also successfully applied using the anthropometrics of a healthy 27 year old adult, and a prototype version of the orthosis was manufactured and tested for assistance on the same individual. However, there are some problems with the orthosis in its current form that will need to be addressed prior to clinical work after the work of this dissertation. The lower shank cuff is thicker than desirable, as it does not flex very much when undergoing loads and can be uncomfortable for the user if undersized. In addition, it may need to be modified to account for an AFO the child may be wearing. This is important to address since about half of those with CP use an AFO [50]. The cuffs on the thigh are thinner than ideal and can become damaged easily so should be thickened. The cuffs can also be made significantly smaller in circumference, making them less fragile and also making material deformation for comfort less important but requiring longer straps for affixing the device to the subject.

The hip cradle can use some in-built or attachable padding to improve fit and comfort. The hip cradle or other links will also need design revisions to include electronics internally such as a battery, microprocessor for control, IMU, etc.

The current actuator design is promising given the experimental results in Sections 3.3 and 3.4. However, there are also some issues with the actuator. Although it was designed to be a compliant actuator with compliance dependent on the belt tension, most of the compliance seems to be in the form of backlash and not stiffness, which is an undesirable characteristic in the actuator. In addition, the compliance level in the actuator cannot be modified during operation and must be set prior to use in the orthosis, making a controller that can modulate stiffness during operation not possible. A significant design change will be necessary if the actuator used in the anthropometrically parametrized orthosis is to behave like a variable-stiffness series-elastic actuator found in the literature. See [105] for a review on design approaches used for these kinds of actuators. Another actuator design change that can potentially improve controller performance is the incorporation of an actuator output torque sensor, which can be used in feedback for an inner-loop actuator torque controller. This will make it unnecessary to account for or make it easier to incorporate friction compensation and actuator dynamics in the control law. Also, direct measurement of the output torque can make intrinsic compliance in the actuator unnecessary as it can be accounted for via a control law, provided sufficient data can be taken with a fast enough controller and capable motors. Another change would be to resolve the chatter issue encountered in the standing balance experiments from

Section 3.5. This could be resolved by replacing the brushless DC motors with brushed motors, removing the discrete locations of the magnets which are suspected cause for the chatter effect. Alternatively, a motor-side braking system could be employed to address chatter as soon as it occurs, though possibly at the cost of increased power consumption. These changes can be taken into account in future design revisions.

Based on the experiments done in this dissertation, the pediatric orthosis technology has made significant progress towards a workable device. However, the device will need to undergo further work prior to working with children. An example outline of this plan is outlined in Figure 5.1 in Section 5.2. Up to this point, the device be judged for its readiness in a clinical setting. In addition to the aforementioned design changes, further work will be necessary prior to clinical testing with children with gait impairments after this dissertation. Not all children with CP, for example, will be able to use the device, especially considering CP is a very heterogeneous condition [1]. The chosen inclusion and exclusion criteria will need to be determined. For example, gross motor function classification system is often used for categorizing children with CP based on gross motor skills and functional ability [1]; those with a gross motor function measure at most III or IV are usually considered for treadmill-based gait rehabilitation [10]. Special care will also have to be considered for spasticity and contractures, which are common in those with CP [2] and can be measured using the modified Ashworth scale, Tardieu scale, or other measures [106].

BIBLIOGRAPHY

[1] S. K. Campbell, R. J. Palisano, and M. N. Orlin, *Physical Therapy for Children*. Elsevier Saunders, 2012.

[2] M. A. Alexander, D. J. Matthews, and K. P. Murphy, *Pediatric Rehabilitation: Principles and Practice*, 5th ed. Demos Medical Publishing, 2015.

[3] R. White, I. Agouris, R. D. Selbie, and M. Kirkpatrick, "The variability of force platform data in normal and cerebral palsy gait," *Clinical Biomechanics*, vol. 14, no. 3, pp. 185–192, Jan. 1999.

[4] Q. Peng, H.-S. Park, P. Shah, N. Wilson, Y. Ren, Y.-N. Wu, J. Liu, D. J. Gaebler-Spira, and L.-Q. Zhang, "Quantitative evaluations of ankle spasticity and stiffness in neurological disorders using manual spasticity evaluator," *Journal of Rehabilitation Research and Development*, vol. 48, no. 4, pp. 473–481, May 2011.

[5] T. A. Wren, S. Rethlefsen, and R. M. Kay, "Prevalence of specific gait abnormalities in children with cerebral palsy: Influence of cerebral palsy subtype, age, and previous surgery," *Journal of Pediatric Orthopaedics*, vol. 25, no. 1, pp. 79–83, Jan. 2005.

[6] M. Shin, L. M. Besser, C. Siffel, J. E. Kucik, G. M. Shaw, C. Lu, and A. Correa, "Prevalence of spina bifida among children and adolescents in 10 regions in the United States," *Pediatrics*, vol. 126, no. 2, pp. 274–279, Aug. 2010.

[7] A. E. H. Emery, "Population frequencies of inherited neuromuscular diseases—A world survey," *Neuromuscular Disorders*, vol. 1, no. 1, pp. 19–29, Jan. 1991.

[8] D. L. Damiano and S. L. DeJong, "A systematic review of the effectiveness of treadmill training and body weight support in pediatric rehabilitation," *Journal of Neurologic Physical Therapy*, vol. 33, no. 1, pp. 27–44, Mar. 2009.

[9] J. Mehrholz, M. Pohl, and B. Elsner, "Treadmill training and body weight support for walking after stroke," in *The Cochrane Library*, John Wiley & Sons, Ltd, 2014.

[10] A. Mutlu, K. Krosschell, and D. G. Spira, "Treadmill training with partial body-weight support in children with cerebral palsy: A systematic review," *Developmental Medicine & Child Neurology*, vol. 51, no. 4, pp. 268–275, Apr. 2009.

[11] D. P. Ferris, G. S. Sawicki, and A. R. Domingo, "Powered lower limb orthoses for gait rehabilitation," *Topics in Spinal Cord Injury Rehabilitation*, vol. 11, no. 2, pp. 34–49, Sep. 2005.

[12] S. Viteckova, P. Kutilek, and M. Jirina, "Wearable lower limb robotics: A review," *Biocybernetics and Biomedical Engineering*, vol. 33, no. 2, pp. 96–105, 2013.

[13] K. P. Westlake and C. Patten, "Pilot study of Lokomat versus manual-assisted treadmill training for locomotor recovery post-stroke," *Journal of NeuroEngineering and Rehabilitation*, vol. 6, no. 1, p. 18, Jun. 2009.

[14] M. Volpini, V. Bartenbach, M. Pinotti, and R. Riener, "Clinical evaluation of a low-cost robot for use in physiotherapy and gait training," *Journal of Rehabilitation and Assistive Technologies Engineering*, vol. 4, Jan. 2017.

[15] A. M. Dollar and H. Herr, "Lower extremity exoskeletons and active orthoses: Challenges and state-of-the-art," *IEEE Transactions on Robotics*, vol. 24, no. 1, pp. 144–158, Feb. 2008.

[16] A. Young and D. Ferris, "State-of-the-art and future directions for robotic lower limb exoskeletons," *IEEE Transactions on Neural Systems and Rehabilitation Engineering*, vol. 25, no. 2, pp. 171–182, Feb. 2017.

[17] R. Riener, "Technology of the robotic gait orthosis Lokomat," in *Neurorehabilitation Technology*, V. Dietz, T. Nef, and W. Z. Rymer, Eds. London: Springer London, 2012, pp. 221–232.

[18] M. Pajaro-Blazquez, R. Shetye, J. Gallegos-Salazar, and P. Bonato, "Robotic-assisted gait training in children with cerebral palsy in clinical practice," in *Converging Clinical and Engineering Research on Neurorehabilitation*, vol. 1, J. L. Pons, D. Torricelli, and M. Pajaro, Eds. Berlin, Heidelberg: Springer Berlin Heidelberg, 2013, pp. 29–33.

[19] J. Sancho-Pérez, M. Pérez, E. García, D. Sanz-Merodio, A. Plaza, and M. Cestari, "Mechanical description of ATLAS 2020, a 10-DOF paediatric exoskeleton," in *Proceedings of the 19th International Conference on CLAWAR*, 2016, pp. 814–822.

[20] D. Sanz-Merodio, J. Sancho, M. Pérez, and E. García, "Control architecture of the ATLAS 2020 lower-limb active orthosis," in *Proceedings of the 19th International Conference on CLAWAR*, 2016, pp. 860–868.

[21] M. Cestari, D. Sanz-Merodio, J.C. Arevalo, and E. Garcia, "ARES, a variable stiffness actuator with embedded force sensor for the ATLAS exoskeleton," *Industrial Robot: An International Journal*, vol. 41, no. 6, pp. 518–526, Oct. 2014.

[22] "Marsi Bionics," *Marsibionics*. [Online]. Available: http://www.marsibionics.com/?lang=en. [Accessed: 31-Aug-2016].

[23] F. Patané, S. Rossi, F. D. Sette, J. Taborri, and P. Cappa, "WAKE-up exoskeleton to assist children with cerebral palsy: Design and preliminary evaluation in level walking," *IEEE Transactions on Neural Systems and Rehabilitation Engineering*, vol. 25, no. 7, pp. 906–916, Jul. 2017.

[24] Z. F. Lerner, D. L. Damiano, and T. C. Bulea, "A lower-extremity exoskeleton improves knee extension in children with crouch gait from cerebral palsy," *Science Translational Medicine*, vol. 9, no. 404, Aug. 2017.

[25] Z. F. Lerner, D. L. Damiano, H. S. Park, A. J. Gravunder, and T. C. Bulea, "A robotic exoskeleton for treatment of crouch gait in children with cerebral palsy: Design and initial application," *IEEE Transactions on Neural Systems and Rehabilitation Engineering*, vol. 25, no. 6, pp. 650–659, Jun. 2017.

[26] C. Copilusi, A. Margine, and N. Dumitru, "Case study regarding a new knee orthosis for children with locomotion disabilities," *Mechanisms, Transmissions and Applications*, vol. 31, pp. 147–155, Apr. 2015.

[27] C. Copilusi, "Design of a new knee modular orthotic device from cinematic considerations," in *Proceedings of the World Congress on Engineering 2012 Vol III*, London, U.K., 2012.

[28] C. Copilusi, N. Dumitru, and A. Margine, "Children locomotion rehabilitation test bed designed from kinematic considerations," in *New Advances in Mechanism and Machine Science*, 2018, vol. 57, pp. 171–179.

[29] M. Giergiel, A. Budziński, G. Piątek, and M. Wacławski, "Personal lower limb rehabilitation robot for children," in *Advances in Intelligent Systems and Computing*, 2015, vol. 317, pp. 169–176.

[30] M. Canela, A. J. del Ama, and J. L. Pons, "Design of a pediatric exoskeleton for the rehabilitation of the physical disabilities caused by cerebral palsy," in *Converging Clinical and Engineering Research on Neurorehabilitation*, 2013, vol. 1, pp. 255–258.

[31] G. J. Androwis, P. A. Michael, A. Strongwater, and R. A. Foulds, "From hip-knee-ankle orthosis to pediatric exoskeleton," in *The 36th Annual International Conference of the IEEE Engineering in Medicine and Biology Society (EMBC'14)*, Chicago, Illinois, 2014.

[32] J. Kang, D. Martelli, V. Vashista, I. Martinez-Hernandez, H. Kim, and S. K. Agrawal, "Robot-driven downward pelvic pull to improve crouch gait in children with cerebral palsy," *Science Robotics*, vol. 2, no. 8, Jul. 2017.

[33] H. I. Krebs, K. P. Michmizos, L. Monterosso, and J. Mast, "Pediatric Anklebot: Pilot clinical trial," in *IEEE International Conference on Biomedical Robotics and Biomechatronics*, Singapore, 2016, pp. 662–666.

[34] K. P. Michmizos, S. Rossi, E. Castelli, P. Cappa, and H. I. Krebs, "Robot-aided neurorehabilitation: A pediatric robot for ankle rehabilitation," *IEEE Transactions on Neural Systems and Rehabilitation Engineering*, vol. 23, no. 6, pp. 1056–1067, Nov. 2015.

[35] T. Yan, M. Cempini, C. M. Oddo, and N. Vitiello, "Review of assistive strategies in powered lower-limb orthoses and exoskeletons," *Robotics and Autonomous Systems*, vol. 64, pp. 120–136, Feb. 2015.

[36] M. R. Tucker, J. Olivier, A. Pagel, H. Bleuler, M. Bouri, O. Lambercy, J. del R. Millán, R. Riener, H. Vallery, and R. Gassert, "Control strategies for active lower

extremity prosthetics and orthotics: A review," *Journal of NeuroEngineering and Rehabilitation*, vol. 12, no. 1, Jan. 2015.

[37] L. E. Miller, A. K. Zimmermann, and W. G. Herbert, "Clinical effectiveness and safety of powered exoskeleton-assisted walking in patients with spinal cord injury: Systematic review with meta-analysis," *Medical Devices (Auckland, NZ)*, vol. 9, pp. 455–466, Mar. 2016.

[38] G. Carpino, A. Pezzola, M. Urbano, and E. Guglielmelli, "Assessing effectiveness and costs in robot-mediated lower limbs rehabilitation: A meta-analysis and state of the art," *Journal of Healthcare Engineering*, vol. 2018, Jun. 2018.

[39] D. R. Louie and J. J. Eng, "Powered robotic exoskeletons in post-stroke rehabilitation of gait: A scoping review," *Journal of NeuroEngineering and Rehabilitation*, vol. 13, no. 53, Jun. 2016.

[40] T. Chau and J. Fairley, *Paediatric Rehabilitation Engineering: From Disability to Possibility*. CRC Press, 2016.

[41] R. J. Farris, H. A. Quintero, and M. Goldfarb, "Preliminary evaluation of a powered lower limb orthosis to aid walking in paraplegic individuals," *IEEE Transactions on Neural Systems and Rehabilitation Engineering*, vol. 19, no. 6, pp. 652–659, Dec. 2011.

[42] C. Hartigan, M. Goldfarb, R. Farris, K. Ha, and S. Murray, "Newly developed robotic exoskeleton that provides mobility and option for functional electrical stimulation," *Archives of Physical Medicine and Rehabilitation*, vol. 94, no. 10, pp. e18–e19, Oct. 2013.

[43] H. A. Quintero, R. J. Farris, C. Hartigan, I. Clesson, and M. Goldfarb, "A powered lower limb orthosis for providing legged mobility in paraplegic individuals," *Topics in spinal cord injury rehabilitation*, vol. 17, no. 1, pp. 25–33, 2011.

[44] "School-age children development," *MedlinePlus*, 20-Nov-2014. [Online]. Available: https://medlineplus.gov/ency/article/002017.htm. [Accessed: 11-Jan-2017].

[45] M. Hartig and F. H. Kanfer, "The role of verbal self-instructions in children's resistance to temptation," *Journal of Personality and Social Psychology*, vol. 25, no. 2, pp. 259–267, Feb. 1973.

[46] C. D. Fryar, Q. Gu, and C. L. Ogden, *Anthropometric reference data for children and adults: United States, 2007-2010*, vol. 252. Hyattsville, MD: National Center for Health Statistics, 2012.

[47] "REX for Clinic Use," *Rex Bionics*. [Online]. Available: http://www.rexbionics.com/rex-for-clinic-use/. [Accessed: 11-Jan-2017].

[48] "Ekso | FAQ." [Online]. Available: http://staging.eksobionics.com/FAQ. [Accessed: 08-Jan-2016].

[49] "Indego Datasheet," *Indego*, 2014. [Online]. Available: http://www.indego.com/Indego/ImageDownload?staticfile=/Indego/Images/Indego_%20datasheet.pdf. [Accessed: 12-Jan-2017].

[50] M. Wingstrand, G. Hägglund, and E. Rodby-Bousquet, "Ankle-foot orthoses in children with cerebral palsy: A cross sectional population based study of 2200 children," *BMC Musculoskeletal Disorders*, vol. 15, Oct. 2014.

[51] R. E. Behrman, R. Kliegman, and H. B. Jenson, Eds., *Nelson Textbook of Pediatrics*, 16th ed. Philadelphia: W.B. Saunders Co, 2000.

[52] S. Lefmann, R. Russo, and S. Hillier, "The effectiveness of robotic-assisted gait training for paediatric gait disorders: Systematic review," *Journal of NeuroEngineering and Rehabilitation*, vol. 14, no. 1, Dec. 2017.

[53] D. A. Winter, *The Biomechanics and Motor Control of Human Gait: Normal, Elderly and Pathological*. University of Waterloo Press, 1991.

[54] Maxon Motor, "Maxon Flat Motor Catalog: EC 45 Flat." Jun-2013.

[55] S. Wolf, G. Grioli, O. Eiberger, *et al.*, "Variable stiffness actuators: Review on design and components," *IEEE/ASME Transactions on Mechatronics*, vol. 21, no. 5, pp. 2418–2430, Oct. 2016.

[56] H. Yu, S. Huang, G. Chen, Y. Pan, and Z. Guo, "Human–robot interaction control of rehabilitation robots with series elastic actuators," *IEEE Transactions on Robotics*, vol. 31, no. 5, pp. 1089–1100, Oct. 2015.

[57] "ESCON 50/5, 4-Q Servocontroller for DC/EC motors, 5/15 A, 10 - 50 VDC." [Online]. Available: https://www.maxonmotor.com/maxon/view/product/control/4-Q-Servokontroller/409510. [Accessed: 26-Nov-2018].

[58] J. T. Sawicki, C. A. Laubscher, R. J. Farris, and S. J.-S. Etheridge, "Actuating Device for Powered Orthosis," U.S. Patent Application No. 15/485,962, 2017.

[59] R. G. Snyder, L. W. Schneider, C. L. Owings, H. M. Reynolds, D. H. Golmb, and M. A. Schork, *Anthropometry of Infants, Children, and Youths to Age 18 for Product Safety Design. Final Report*. 1977.

[60] K. H. E. Kroemer, H. J. Kroemer, and K. E. Kroemer-Elbert, *Engineering Physiology: Physiologic Bases of Human Factors/Ergonomics*. Elsevier, 1986.

[61] "Key Insights On Orthotics, AFOs And Casting For Kids | Podiatry Today." [Online]. Available: https://www.podiatrytoday.com/key-insights-orthotics-afos-and-casting-kids. [Accessed: 20-Sep-2018].

[62] D. Zanotto, Y. Akiyama, P. Stegall, and S. K. Agrawal, "Knee joint misalignment in exoskeletons for the lower extremities: Effects on user's gait," *IEEE Transactions on Robotics*, vol. 31, no. 4, pp. 978–987, Aug. 2015.

[63] C. A. Laubscher, R. J. Farris, and J. T. Sawicki, "Design and preliminary evaluation of a powered pediatric lower limb orthosis," in *Proceedings of the ASME 2017 International Design Engineering Technical Conferences & Computers and Information in Engineering Conference*, Cleveland, OH, 2017.

[64] C. A. Laubscher, R. J. Farris, and J. T. Sawicki, "Angular momentum-based control of an underactuated orthotic system for standing balance," *Autonmous Robots*, Springer, under review.

[65] "Truper | College Park," *College Park Industries*, 2018. [Online]. Available: https://www.college-park.com/truper. [Accessed: 28-Sep-2018].

[66] K. Shamaei, G. S. Sawicki, and A. M. Dollar, "Estimation of quasi-stiffness and propulsive work of the human ankle in the stance phase of walking," *PLoS ONE*, vol. 8, no. 3, Mar. 2013.

[67] D. A. Winter, *Biomechanics and Motor Control of Human Movement*, 4th ed. Hoboken, NJ: John Wiley & Sons, 2009.

[68] D. J. Maher, A. A. Garnett, C. A. Laubscher, J. T. Sawicki, and D. J. Simon, "Extended Kalman filter-based control of a pediatric exoskeleton," in *ASME International Mechanical Engineering Congress & Exposition*, Tampa, FL, 2017.

[69] A. Esquenazi, M. Talaty, A. Packel, and M. Saulino, "The ReWalk powered exoskeleton to restore ambulatory function to individuals with thoracic-level motor-complete spinal cord injury," *American Journal of Physical Medicine & Rehabilitation*, vol. 91, no. 11, pp. 911–921, Nov. 2012.

[70] N.-S. Kwak, K.-R. Müller, and S.-W. Lee, "A lower limb exoskeleton control system based on steady state visual evoked potentials," *Journal of Neural Engineering*, vol. 12, no. 5, 2015.

[71] H.-F. Liao, S.-F. Jeny, J.-S. Lai, C. K. Cheng, and M.-H. Hu, "The relation between standing balance and walking function in children with spastic diplegic cerebral palsy," *Developmental Medicine & Child Neurology*, vol. 39, no. 2, pp. 106–112, Sep. 2008.

[72] S. González-Mejía and J. M. Ramírez-Scarpetta, "Design and implementation of a control strategy for static balance of a lower limbs exoskeleton," *Ingeniería y Competitividad*, no. 1, p. 10, Jun. 2014.

[73] A. L. Hof, M. G. J. Gazendam, and W. E. Sinke, "The condition for dynamic stability," *Journal of Biomechanics*, vol. 38, no. 1, pp. 1–8, Jan. 2005.

[74] S. Wang, L. Wang, C. Meijneke, *et al.*, "Design and control of the MINDWALKER exoskeleton," *IEEE Transactions on Neural Systems and Rehabilitation Engineering*, vol. 23, no. 2, pp. 277–286, Mar. 2015.

[75] A. Tsukahara, R. Kawanishi, Y. Hasegawa, and Y. Sankai, "Sit-to-stand and stand-to-sit transfer support for complete paraplegic patients with robot suit HAL," *Advanced Robotics*, vol. 24, no. 11, pp. 1615–1638, Jan. 2010.

[76] B. Siciliano and O. Khatib, *Springer Handbook of Robotics*. Springer Science & Business Media, 2008.

[77] M. Vukobratović and B. Borovac, "Zero-moment point—thirty five years of its life," *International Journal of Humanoid Robotics*, vol. 1, no. 1, pp. 157–173, Mar. 2004.

[78] X. Lai, X. Wu, Y. Fang, and X. Wang, "A survey of balance control strategy for humanoid robots."

[79] H. F. N. Al-Shuka, B. Corves, W.-H. Zhu, and B. Vanderborght, "Multi-level control of zero-moment point-based humanoid biped robots: A review," *Robotica*, vol. 34, no. 11, pp. 2440–2466, Nov. 2016.

[80] N. Aphiratsakun and M. Parnichkun, "Balancing control of AIT leg exoskeleton using ZMP based FLC," *International Journal of Advanced Robotic Systems*, vol. 6, no. 4, pp. 319–328, Dec. 2009.

[81] M. Azad and R. Featherstone, "Angular momentum based balance controller for an under-actuated planar robot," *Autonomous Robots*, vol. 40, no. 1, pp. 93–107, Jan. 2016.

[82] J. J. Craig, *Introduction to Robotics: Mechanics and Control*. Pearson/Prentice Hall, 2005.

[83] C. G. Atkeson, C. H. An, and J. M. Hollerbach, "Estimation of inertial parameters of manipulator loads and links," *The International Journal of Robotics Research*, vol. 5, no. 3, pp. 101–119, Sep. 1986.

[84] K. S. Fu, R. C. González, and C. S. G. Lee, *Robotics: Control, Sensing, Vision, and Intelligence*. McGraw-Hill, 1987.

[85] M. Gautier and W. Khalil, "A direct determination of minimum inertial parameters of robots," in *IEEE International Conference on Robotics and Automation Proceedings*, Philadelphia, PA, USA, 1988, pp. 1682–1687.

[86] C. L. Lawson and R. J. Hanson, *Solving Least Squares Problems*. SIAM, 1995.

[87] R. A. Rubinstein, K. D. Shelbourne, C. D. VanMeter, J. R. McCarroll, A. C. Rettig, and R. L. Gloyeske, "Effect on knee stability if full hyperextension is restored immediately after autogenous bone-patellar tendon-bone anterior cruciate ligament reconstruction," *The American Journal of Sports Medicine*, vol. 23, no. 3, pp. 365–368, May 1995.

[88] K. M. Jagodnik and A. J. van den Bogert, "Optimization and evaluation of a proportional derivative controller for planar arm movement," *Journal of Biomechanics*, vol. 43, no. 6, pp. 1086–1091, Apr. 2010.

[89] C. A. Laubscher, R. J. Farris, A. J. van den Bogert, and J. T. Sawicki, "Assistive control of an anthropometrically parametrized lower-limb exoskeleton," *IEEE Transactions on Neural Systems and Rehabilitation Engineering*, submitted.

[90] S. M. Cain, K. E. Gordon, and D. P. Ferris, "Locomotor adaptation to a powered ankle-foot orthosis depends on control method," *Journal of NeuroEngineering and Rehabilitation*, vol. 4, Dec. 2007.

[91] J. R. Koller, D. A. Jacobs, D. P. Ferris, and C. D. Remy, “Learning to walk with an adaptive gain proportional myoelectric controller for a robotic ankle exoskeleton,” *Journal of NeuroEngineering and Rehabilitation*, vol. 12, no. 1, 2015.

[92] G. S. Sawicki and D. P. Ferris, “A pneumatically powered knee-ankle-foot orthosis (KAFO) with myoelectric activation and inhibition,” *Journal of NeuroEngineering and Rehabilitation*, vol. 6, 2009.

[93] C. Fleischer and G. Hommel, “A human–exoskeleton interface utilizing electromyography,” *IEEE Transactions on Robotics*, vol. 24, no. 4, pp. 872–882, Aug. 2008.

[94] T. Lenzi, M. C. Carrozza, and S. K. Agrawal, “Powered hip exoskeletons can reduce the user’s hip and ankle muscle activations during walking,” *IEEE Transactions on Neural Systems and Rehabilitation Engineering*, vol. 21, no. 6, pp. 938–948, Nov. 2013.

[95] G. Aguirre-Ollinger, J. E. Colgate, M. A. Peshkin, and A. Goswami, “Design of an active one-degree-of-freedom lower-limb exoskeleton with inertia compensation,” *The International Journal of Robotics Research*, vol. 30, no. 4, pp. 486–499, Apr. 2011.

[96] A. Gams, T. Petrič, T. Debevec, and J. Babič, “Effects of robotic knee exoskeleton on human energy expenditure,” *IEEE Transactions on Biomedical Engineering*, vol. 60, no. 6, pp. 1636–1644, Jun. 2013.

[97] R. Ronsse, T. Lenzi, N. Vitiello, B. Koopman, E. van Asseldonk, S. M. M. De Rossi, J. van den Kieboom, H. van der Kooij, M. C. Carrozza, and A. J. Ijspeert, “Oscillator-based assistance of cyclical movements: Model-based and model-free

approaches," *Medical & Biological Engineering & Computing*, vol. 49, no. 10, pp. 1173–1185, Sep. 2011.

[98] D. P. Ferris, G. S. Sawicki, and M. A. Daley, "A physiologist's perspective on robotic exoskeletons for human locomotion," *International Journal of Humanoid Robotics*, vol. 4, no. 3, pp. 507–528, Sep. 2007.

[99] K. Shamaei, M. Cenciarini, A. A. Adams, K. N. Gregorczyk, J. M. Schiffman, and A. M. Dollar, "Design and evaluation of a quasi-passive knee exoskeleton for investigation of motor adaptation in lower extremity joints," *IEEE Transactions on Biomedical Engineering*, vol. 61, no. 6, pp. 1809–1821, Jun. 2014.

[100] O. Barzilay and A. Wolf, "A fast implementation for EMG signal linear envelope computation," *Journal of Electromyography and Kinesiology*, vol. 21, no. 4, pp. 678–682, Aug. 2011.

[101] T. C. Pataky, "Generalized n-dimensional biomechanical field analysis using statistical parametric mapping," *Journal of Biomechanics*, vol. 43, no. 10, pp. 1976–1982, Jul. 2010.

[102] R. C. Browning, J. R. Modica, R. Kram, and A. Goswami, "The effects of adding mass to the legs on the energetics and biomechanics of walking," *Medicine & Science in Sports & Exercise*, vol. 39, no. 3, pp. 515–525, Mar. 2007.

[103] K. Yoshino, T. Motoshige, T. Araki, and K. Matsuoka, "Effect of prolonged free-walking fatigue on gait and physiological rhythm," *Journal of Biomechanics*, vol. 37, no. 8, pp. 1271–1280, Aug. 2004.

[104] J. Zhang, P. Fiers, K. A. Witte, R. W. Jackson, K. L. Poggensee, C. G. Atkeson, and S. H. Collins, "Human-in-the-loop optimization of exoskeleton assistance during walking," *Science*, vol. 356, no. 6344, pp. 1280–1284, Jun. 2017.

[105] B. Vanderborght, A. Albu-Schaeffer, A. Bicchi, *et al.*, "Variable impedance actuators: A review," *Robotics and Autonomous Systems*, vol. 61, no. 12, pp. 1601–1614, Dec. 2013.

[106] M. Germanotta, J. Taborri, S. Rossi, F. Frascarelli, E. Palermo, P. Cappa, E. Castelli, and M. Petrarca, "Spasticity measurement based on tonic stretch reflex threshold in children with cerebral palsy using the PediAnklebot," *Frontiers in Human Neuroscience*, vol. 11, May 2017.

APPENDICES

APPENDIX A

MEASURED ANTHROPOMETRICS

The anthropometrics below include both necessary and inferred values, and are grouped by region on the body. For all standing measurements, the subject should stand erect with feet together, arms hanging at the sides, and weight evenly distributed, unless otherwise stated. For all sitting measurements, the subject should sit erect on a chair or flat table surface parallel to the ground with knees together and feet on a surface also parallel to the ground such that the knees are flexed at 90 deg, unless otherwise stated. If time permits, take multiple measurements to verify values. In addition, take measurements for both the left and right leg and record both values when applicable. For all distance measurements, apply little pressure to the skin to minimize body compliance to avoid measurement inaccuracy. When multiple sites of pressure are necessary for a measurement, apply the pressure evenly.

Table XVI. Measured anthropometrics

Age	Record subject age on the date in which measurements are taken.
Sex	Record if the subject is male or female.
Stature (Standing Height)	With the subject standing with head oriented facing forward as one would naturally, measure the vertical distance from the ground to the top of the head. See page 64 in [59].
Weight	With the subject standing on a scale with minimal influence of other sources of weight, record the measured weight. See page 60 in [59].
Waist Height	With the subject standing, measure the vertical distance from the ground to the navel. See page 332 in [59].
Waist Circumference	With the subject standing, measure the circumference of the torso at *Waist Height* in the transverse plane. See page 336 in [59].
Waist Breadth	With the subject standing, measure the horizontal breadth of the torso at *Waist Height* in the transverse plane. See page 340 in [59].
Waist Depth	With the subject standing, measure the horizontal depth of the torso at *Waist Height* in the transverse plane. This value should equal to the sum of *Waist Depth Back* and *Waist Depth Front*.

Waist Depth Back	With the subject standing, measure the approximate horizontal depth from the midaxillary line at *Waist Height* to the most posterior part of the waist within the transverse plane.
Waist Depth Front	With the subject standing, measure the approximate horizontal depth from the midaxillary line at *Waist Height* to the most anterior part of the waist within the transverse plane.
Waist Natural Height	With the subject standing, measure the vertical distance from the ground to the point of minimal circumference near the waist.
Waist Natural Circumference	With the subject standing, measure the circumference of the torso at *Waist Natural Height* in the transverse plane. See page 344 in [59].
Waist Natural Breadth	With the subject standing, measure the horizontal breadth of the torso at *Waist Natural Height* in the transverse plane. See page 340 in [59].
Waist Natural Depth	With the subject standing, measure the horizontal depth of the torso at *Waist Natural Height* in the transverse plane. This value should equal to the sum of *Waist Natural Depth Back* and *Waist Natural Depth Front*.
Waist Natural Depth Back	With the subject standing, measure the approximate horizontal depth from the midaxillary line at *Waist Natural Height* to the most posterior part of the waist within the transverse plane.
Waist Natural Depth Front	With the subject standing, measure the approximate horizontal depth from the midaxillary line at *Waist Natural Height* to the most anterior part of the waist within the transverse plane.
Iliocristale Height	With the subject standing, measure the vertical distance from the ground to the highest point on the iliac crest of the pelvis. See page 348 in [59].
Hip Buttocks Height	With the subject standing, measure the vertical distance from the ground to the maximum posterior protrusion of the buttocks. See page 352 in [59].
Hip Breadth Max Seated	With the subject sitting, measure the maximum breadth across the hips parallel to the seated surface. See page 104 in [59].
Trochanteric Height	With the subject standing, measure the vertical distance from the ground to the greater trochanter landmark. See page 376 in [59].
Hip Trochanter Breadth	With the subject standing, measure the horizontal distance between the left and right greater trochanter landmarks. See page 360 in [59].
Thigh Breadth Max Seated	With the subject sitting, measure the maximum breadth across the thighs. See page 108 in [59].
Thigh Clearance	With the subject sitting, measure the vertical distance from the sitting surface to the highest point of the thigh near the abdominal-thigh junction. See page 112 in [59].
Thigh Upper Height	With the subject standing, measure the vertical distance from the ground to the upper part of the thigh below the gluteal furrow. This directly determines the placement of the top part of the top cuff.
Thigh Upper Circumference	With the subject standing with legs slightly separated, measure the horizontal circumference of the thigh at *Thigh Upper Height*. See page 380 in [59].
Thigh Upper Breadth	With the subject standing, measure the horizontal breadth of the thigh at *Thigh Upper Height* in the transverse plane.
Thigh Upper Depth	With the subject standing, measure the horizontal depth of the thigh at *Thigh Upper Height*. See page 384 in [59].
Thigh Lower Height	With the subject standing, measure the vertical distance from the ground to the bottom part of the thigh above the knee. This directly determines the placement of the bottom part of the bottom cuff.

Thigh Lower Circumference	With the subject standing with legs slightly separated, measure the horizontal circumference of the thigh at *Thigh Lower Height*.
Thigh Lower Breadth	With the subject standing, measure the horizontal breadth of the thigh at *Thigh Lower Height* in the transverse plane.
Thigh Lower Depth	With the subject standing, measure the horizontal depth of the thigh at *Thigh Lower Height*.
Knee Height Seated	With the subject sitting, measure the vertical distance from the foot-resting surface to the top of the knee, where the top and back of the patella is located. See page 120 in [59].
Tibiale Height	With the subject standing, measure the vertical distance from the ground to the tibiale. See page 388 in [59].
Shank Upper Height	With the subject standing, measure the vertical distance from the ground to the upper part of the shank. This directly determines the placement of the middle part of the top cuff. See page 392 in [59].
Shank Upper Circumference	With the subject standing with legs slightly separated, measure the circumference of the shank at *Shank Upper Height* in the transverse plane. See page 396 in [59].
Shank Upper Breadth	With the subject standing, measure the horizontal breadth of the thigh at *Shank Upper Height* in the transverse plane.
Shank Upper Depth	With the subject standing, measure the horizontal depth of the shank at *Shank Upper Height* in the transverse plane. See page 400 in [59].
Shank Lower Height	With the subject standing, measure the vertical distance from the ground to the upper part of the shank. This directly determines the placement of the middle part of the bottom cuff. See page 392 in [59].
Shank Lower Circumference	With the subject standing with legs slightly separated, measure the circumference of the shank at *Shank Lower Height* in the transverse plane. See page 396 in [59].
Shank Lower Breadth	With the subject standing, measure the horizontal breadth of the thigh at *Shank Lower Height* in the transverse plane.
Shank Lower Depth	With the subject standing, measure the horizontal depth of the shank at *Shank Lower Height* in the transverse plane. See page 400 in [59].
Shank Front	With the subject standing, measure the approximate horizontal depth from the central axis of the tibia between *Shank Lower Height* and *Shank Upper Height* to the most anterior part of the shin within the transverse plane.
Ankle Circumference	With the subject standing with feet slightly separated, measure the minimum horizontal circumference of the ankle above the sphyrion and malleoli in the transverse plane. See page 404 in [59].
Ankle Breadth	With the subject standing with feet apart, measure the minimum horizontal breadth of the ankle above the sphyrion and malleoli in the transverse plane. See page 408 in [59].
Ankle Depth	With the subject standing with feet apart, measure the minimum horizontal depth of the ankle above the sphyrion and malleoli in the transverse plane.
Sphyrion Height	With the subject standing with feet apart, measure the vertical distance from the ground to the sphyrion. See page 412 in [59].

Height: Superior-inferior direction, typically from the ground
Circumference: Within the transverse (horizontal) plane
Depth: Anterior-posterior direction, within the transverse plane
Breadth: Medial-lateral direction, within the transverse plane